DIRECT NUMERICAL SIMULATION OF HUMAN PHONATION

BY

SHAKTI SAURABH

DISSERTATION

Submitted in partial fulfillment of the requirements
for the degree of Doctor of Philosophy in Aerospace Engineering
in the Graduate College of the
University of Illinois at Urbana-Champaign, 2017

Urbana, Illinois

Doctoral Committee:

Professor Daniel J. Bodony, Advisor
Professor Philippe H. Geubelle
Professor Jonathan B. Freund
Professor Bradley P. Sutton

Abstract

The generation and propagation of the human voice is studied using direct numerical simulation. A full body domain is employed for the purpose of directly computing the sound in the region past the speaker's mouth. The air in the vocal tract is modeled as a compressible and viscous fluid interacting with the vocal folds (VFs). The vocal fold tissue material properties are multi-layered, with varying stiffness, and a finite-strain model is utilized and implemented in a quadratic finite element code. The fluid-solid domains are coupled through a boundary-fitted interface and utilize a Poisson equation-based mesh deformation method. The domain includes an anatomically relevant vocal tract geometry, either in two dimensions or in three dimensions. Adult and two-year-old child anatomy inspired simulations are performed. Phonation simulations using a non-linear hyper elastic, linear elastic and viscoelastic models of the VFs are performed and compared. The sensitivity of phonation to the VF Poisson's ratio is also evaluated.

Simulations are employed to investigate voice disorders related to vocal fold stiffness asymmetry and unilateral vocal fold paralysis (UVFP). Additionally, an analysis is performed for medialization laryngoplasty, a well known surgical treatment for UVFP. Phonation onset is determined from all the simulations as a measure of degree of voice disorder with phonation threshold pressure (PTP) as a key parameter for the quantification.

The computational model developed is demonstrated to be consistent with prior measurements and sufficiently sensitive to be used in future studies involving VF pathologies, surgical procedures to restore voice, and/or closed loop models of voice, speech and perception.

To my lovely wife Parul

Acknowledgements

I would like to take this opportunity to acknowledge the help and support of a number of people whose crucial contribution over the past four and a half years helped lead to a successful completion of my PhD. First, I thank Professor Daniel J. Bodony, my advisor, for his guidance, friendship and endless patience. His constant motivation and encouragement has always kept my spirits high. I would also like to thank my thesis committee, Professor Jonathan B. Freund, Professor Philippe H. Geubelle and Professor Bradley P. Sutton for their valuable inputs and suggestions towards my research.

I am grateful for the support from the National Science Foundation (CAREER award number 1150439, Dr. D. Papavassiliou as the technical monitor). I acknowledge computational resources provided by the NSF XSEDE resources, award number TG-CTS090004.

I would also like to thank my family for their loving support and continued patience. I am especially grateful to my wife Parul Chadha for standing by my side throughout the duration of my PhD and never giving up on me. I also thank my close friends Saurabh Gupta and Amal Sahai for their support and constant motivation.

I would like to extend my sincere gratitude to Dr. Mahesh Natarajan, a previous member of our lab, for always bringing me out of situations when I would be stuck on any problem. My special gratitude to Dr. Chris Ostoich, upon whose work I build my research and whose selfless and humble support helped me with numerous difficult situations. I also thank my other previous lab mates Dr. Nek Sharan, Dr. Qi Zhang, Wentao Zhang and Ryan Tomokiyo for their help and support. I would also like to thank my current lab mates Cory Mikida, Bryson Sullivan, Fabian Dettenrieder, Dr. Mohammad Mehrabadi, Michael Banks and Dr. Shreyas Bidadi for their positvive feedback on my research and for constantly cheering me up.

Table of Contents

List of Tables

List of Figures

Chapter 1

Introduction

1.1 Background

For humans, voice is the most important mode of communication. Voice also serves other purposes, such as singing and expressing emotions. It can also be studied as an attribute of speech production, which is comprised of three major physical phenomena, namely: respiration, i.e., the mechanical process of moving air in and out of the the lungs; phonation, which is the process of producing periodic sound waves due to the vibration of vocal folds (VF); and articulation, i.e., the process of resonance taking place in the vocal cavities due to the movements of structures such as jaw, teeth, lips, tongue and soft palate [1]; see Figure 1.1.

Understanding the generation and propagation of voice has been a subject of study since 1940. In this regard, phonation has received considerable attention but is yet not fully understood. Reports from the National Institutes of Health suggest that close to 7.5 million people in the United States suffer from some kind of voice disorder involving the VFs. Approximately, one-third of these people suffer from full or partial VF paralysis, which leads to reduced or complete loss of voice [2].

The study of phonation involves an understanding of aerodynamics and structural mechanics. It is this complex multi-physics nature of the problem and the limitations associated with performing *in vivo* investigation of the VFs which makes the study of phonation challenging and rewarding.

1.2 Physics of VF vibration

The VFs have a multilayered structure. They are primarily comprised of three layers, as shown in Figure 1.2: the cover, which consists of the epithelium and the superficial layer of the lamina propria; the transition layer, which

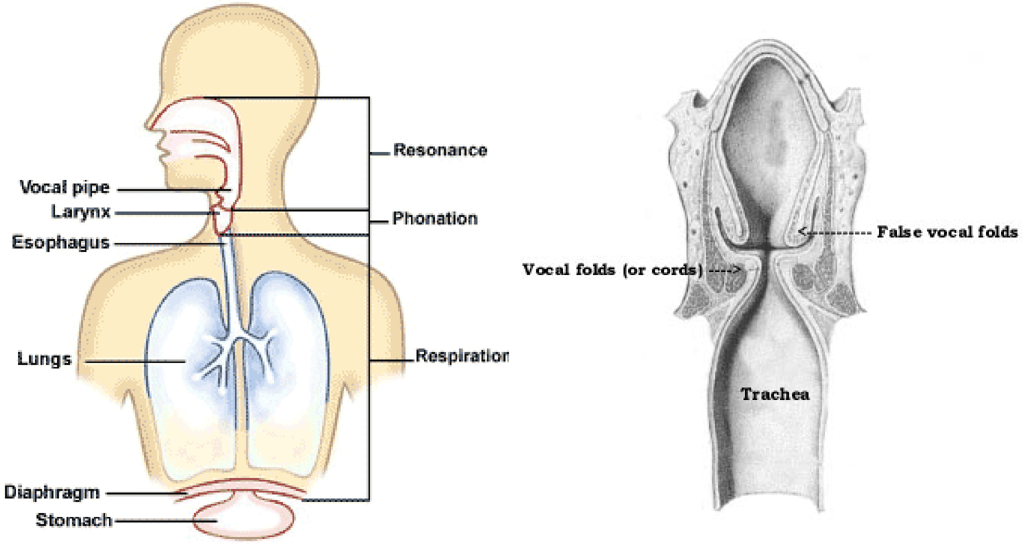

Figure 1.1: Stages of voice production; *Source: Anatomy and Physiology, John Hopkins Voice Center* (left), and false VFs; *Source: How Singing is Created-Vocal Anatomy* (right) .

consists of the intermediate and deep layers of the lamina propria, also called the ligament; and, the body, which is composed of vocalis muscles [3,4].

The generation of voiced sound is related to the vibration of the VFs. The VFs vibrate when the diaphragm expels air from the lungs and creates a pressure difference across them of the order of 1 kiloPascal, after which a self-sustained oscillation is achieved. The precise pressure difference above which oscillations are possible, known as the threshold pressure, is a function of the VF material properties [5,6]. Once self-sustained motion is established, the VFs oscillate with a dominant frequency F0 in the range of 125 Hz for an adult male, 200 Hz for an adult female, and up to 500 Hz for an infant, but exhibit a broadband spectrum due in part to the layered, fibrous nature of the VF tissue [7,8].

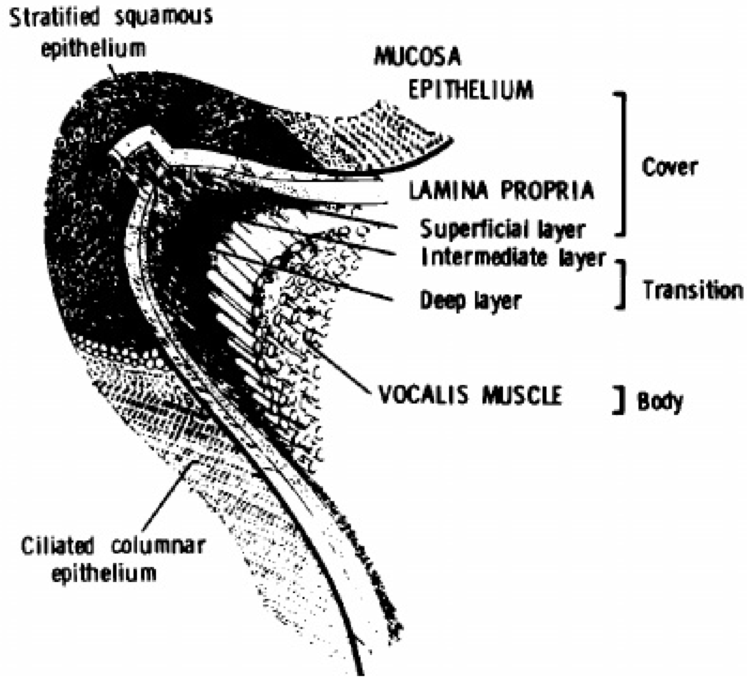

Figure 1.2: A schematic presentation of the human vocal fold (Hirano, 1975).

1.3 Literature Review

Phonation or vocal fold study has been looked into under three major categories: reduced order models, experiments, and detailed simulations. Other important aspects related to phonation based studies like VF viscoelasticity and VF pathology have been treated separately and will be discussed later.

1.3.1 Reduced Order VF and Glottal Flow Modeling

Reduced order VF model also referred to as lumped-element modeling was first proposed as a single mass oscillator system [9], subsequently extended to two spring-mass damper systems [10], one for each VF, wherein the VFs were driven by a applied pressure load. This latter model gained significant popularity and formed the basis for further and more refined reduced order models. The springs in these models represent the elastic nature of the VF, while the dampers provide a viscous characteristic. ROMs provide a simplified way of capturing the dynamics of the VFs while being computationally inexpensive. As such, reduced order models, gained significant development and are extensively researched [11–19]. While initial studies were mostly focused on a single layer model of the VF, more recent studies have been able to incorporate two-layered models [18, 20] as well as 3D models [21].

The main purpose of the VFs is to create a transient glottal jet whose properties control the sound to be uttered. The glottal jet properties are not known in detail but rather have been investigated from a global perspective. Early descriptions of the glottal jet focused on the so called glottal airflow waveform, a one-dimensional periodic volume flux with tunable parameters to match *in vivo* data [22]. From the unsteady velocity signal, Bernoulli's equation is used to estimate the unsteady pressure by a quasi-steady assumption. The asymmetry of the glottal waveform has been correlated to the voice quality: more asymmetry implies a brassy quality while less implies a breathy quality [23]. Because of its simplicity and possibility for experimental measurement, the 1-D waveform model continues to be used as means of understanding the role of fluid unsteadiness in the glottal jet dynamics [24].

The reduced order models have been unable to capture detailed VF motion visualized *in vivo*; in particular, they do not permit a non-uniform displacement towards the glottis centerline. They were also based on a symmetric domain and an inviscid flow assumption for the glottal fluid so that they can use the Bernoulli's equation to compute fluid loads [25–28]. These assumptions restrict more realistic asymmetric behavior of the flow past the glottis, as well as flow separation from the VF, which has been shown to be important [29]. However, some studies have overcome this difficulty by implementing boundary layer solvers [29, 30] while some have even coupled these reduced order models with Navier-Stokes simulations [31, 32] of the glottal fluid.

1.3.2 Experiments

Initial experimental studies using physical and synthetic VF models focused mostly around static VF models. Many of these were centered around 2D geometries [33–37], while some considered physiologically relevant 3D VF models [38, 39]. While all of these [33–39] studied the glottal flow as steady, there have been more recent efforts made to study the flow as unsteady [29, 40–45]. Again, the limitation of a static VF produces significant challenges in accurately obtaining a physically-relevant flow field. This problem was some-what answered by utilizing excised canine larynges [46–52] as compared to physical VF models. However, limitations in run time and the challenges associated with restoration of proper tensioning have restricted the use of excised canine larynges. This difficulty has been overcome by a more feasible alternative [53], by developing a fully synthetic VF model using silicone polymer, which have been extensively used to investigate a fully coupled fluid-structure interaction of the fluid with the VF model. These models have also been widely used to study glottal flow aerodynamics and speech pathologies [54–61].

1.3.3 CFD Simulations

With the advent of fast computational resources in the past decade and a half, the ability of computational fluid dynamics (CFD) to study phonation has gained increased attention. However, the fidelity of CFD techniques are challenged by the uncertainty in determining accurate material properties and the internal layering of the VFs. This was overcome in a recent study [62], which has provided quantitative estimates to the above problems.

Initial investigations using CFD assumed rigid VFs [63–65] or with a prescribed motion [66–70]. Only a small subset of studies allowed the VF motion to be dynamically coupled with the glottal flow [71–73]. The first 3D continuum model of the VF was developed using finite-element method only in 2000 [67]. The flow model used was Bernoulli's equations. More recently, a sharp-interface immersed boundary method has been developed and implemented to study both the glottal airflow and linear viscoelastic VFs [71, 72]. Recent simulations implementing a fully coupled, 3D continuum based model of the VF and the glottal flow [61, 73–75] have been performed.

Only the Frankel group simulations [63, 65, 70] used a compressible formulation wherein the sound was directly predicted; all others used an incompressible formulation and were consequently focused on the aerodynamics of the glottal jet. These latter simulations found that, at least in 2-D, the false vocal folds (a pair of passive VF-like tissues in the glottis, see Figure 1.1) are critical in obtaining a stable glottal jet and confirmed that additional degrees of freedom in the VF motion, as in a multi-mass or continuum mechanics descriptions discussed above, resulted in a more complex glottal jet. The compressible simulations used rigid [70] or a prescribed VF motion [63, 65] to compare the directly radiated sound measured at a point downstream of the glottis to an acoustic analogy-based [76, 77] prediction and found sizable disagreement, suggesting that incompressible simulations may not capture the radiated sound correctly when using an acoustic analogy.

One aspect usually missing in simulation based phonation studies is characterizing the far-field acoustics which requires a full body simulation with domain encompassing regions outside the speaker's mouth. Most of the focus has been on capturing the VF dynamics using a simulation domain usually truncated at the mouth. There are only a few studies which have utilized an anatomically representative vocal tract geometry [78–82]. More often, only a simplified rectangular vocal tract is generally employed [32, 72, 74, 83, 84]. It is necessary to conduct a full body simulation with a realistic vocal tract geometry to be able to relate the results thus obtained to clinical studies which, in most circumstances, measure the voice quality data outside the subject's mouth [85–87]. Simulations have used a variety of Poisson's ratio that requires more attention. Even though the VFs are likely nearly incompressible elements [53, 88–90], Poisson's ratio values of as low as 0.3 have been used in several phonation simulations [71, 72, 91, 92]. A recent study did a parametric analysis of effect of changing Poisson's ratio from 0.4 to 0.5, yet it did not consider values down to 0.3 [93]. This study also observed that Poisson's ratio above 0.49 and below 0.43 did not yield model motion that was similar to human VFs. For values of Poisson's ratio equal to 0.49999, there was very little VF deformation and the model did not vibrate.

There is an abundance of clinical assessment of child phonation [94–96], however simulation based research of this aspect is still scarce [97]. VF material property sensitivity usually related to pathological conditions, is another aspect which has received some study [17, 84, 98, 115], but without direct connection to far-field sound. A common question which has been overlooked in phonation simulations is to identify whether the VFs adhere to a linear or a finite deformation elastic modulus. Studies have used both linear elastic model [32, 71, 72, 74, 83, 84] as well as a finite deformation non-linear or hyper elastic models [53, 93, 99] interchangeably. A comparative analysis for the two models thus becomes imperative especially to understand the VF material property relevance to the phonated sound.

1.3.4 VF Viscoelasticity

Material characterization and subsequent continuum modeling of the VFs, is an area of research which has recently gained substantial momentum. One such aspect that is usually understated in several phonation based simulation studies is the viscoelastic nature of the VFs. The first requirement for any such study should be to utilize experimental data to corroborate the viscoelastic material properties that will be used for simulations. Several studies in the past have been able to achieve this using experimental techniques like parallel-plate torsional rheometry at small strain amplitudes [100–104] and controlled-stress torsional rheometry [100,104]. However, the frequency range of viscoelastic measurements varied from 0.1 Hz to 80 Hz. This range of frequencies does not comply with phonatory frequencies and, as such, requires frequency extrapolation [101, 102, 105] to be useful for simulation purposes. However, a recent study [106] has come up with measurements for frequencies upto 250 Hz, using a custom-built controlled-strain, linear simple-shear rheometer with human tissue samples.

The first attempts to model VF viscoelasticity came in the form of reduced order modeling. Initially modeled as a single spring-mass-damper system [10], many studies were conducted [11–14, 16–19], where the viscous effect of the VFs were characterized via the use of dampers in the system. Although significant advancements were made in phonation studies using these models, they lacked the ability to physiologically correlate the tissue properties to the system parameters. Continuum based models provided an answer to this underlying problem.

Effort has been applied to model VF tissue viscoelasticity in both 2D and 3D continuum based simulations. The first study utilizing tissue viscoelasticity [67] was, again, based on measurements taken at sub-phonation frequencies. Following this, several studies [71, 72, 74, 75, 107], simply used the viscoelastic parameters from Alipour et. al. [67], without much emphasis on verification of the parameters itself. The simple Kelvin-Voigt model was used for the strain rate characterization. The same model was also used in other studies [73, 78, 83]; again, with no particular attention given to verify the viscoelastic parameters used. The lack of data near phonation frequencies inhibited such verifications. Another study [108] looked at parametrically varying the viscous parameter to characterize the effects on phonation threshold pressure and fundamental frequency. It has been pointed in a recent study [71] that the choice of tissue viscosity used in several studies so far is full of some degree of uncertainty which has not been considered in great depths.

1.3.5 VF Pathology

The disruption of speech is traumatic. When the vocal fold properties change, or when one vocal fold becomes unusable, there is a corresponding change or loss of voice. This could range from temporary VF irregularity such as inflammation [109] and vocal fold scarring [110] to a more permanent condition like unilateral vocal fold paralysis and bilateral vocal fold paralysis [111, 112].

Such pathological conditions have been studied, including the underlying biomechanical left-right asymmetry of the VFs. Synthetic VF models have been widely used for this purpose [59, 113–115]. In particular the study by Zhang et al. [114, 115] used a detailed series of VF body layer stiffness asymmetry cases, studied with the help of a synthetic VF, where several acoustic parameters were collected and analyzed. They emphasized the importance of the body layer stiffness in voice production, a conclusion that was established by previous studies [18, 56, 116–118].

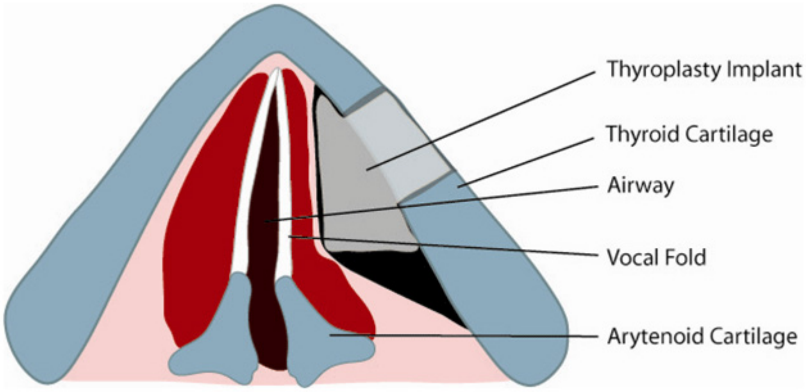

Figure 1.3: An illustration of medialization laryngoplasty. *Source: Vocal Fold Paralysis; Baylor College of Medicine.*

The last few decades witnessed a growth of computational modeling to study voice disorders. However, most of these studies were based on reduced order model of the VFs [17,32,119–123]. A recent study based on continuum model of the vocal folds [115] explored the effect of body layer stiffness asymmetry on the acoustic parameters. However, the flow model was based on quasi-1d potential flow determination with absence of a full vocal tract geometry. Although these studies give invaluable insight into the computational aspect of studying voice disorders, they lack the physical realism of a fully continuum based model, such as neglecting viscous effects and physiological dependence between the model system parameters and tissue properties. Recently, an effort [84] tried to bridge this gap by developing a tool for a fully continuum based model, but a detailed analysis of various aspects of voice disorders is missing, including acoustic relation to the biomechanics irregularities of the VFs. Another study [98] looked at small tension imbalance (up to 20%) between left and right vocal folds using a full continuum based modeling. Hence a detailed computational analysis of UVFP and its subsequent treatment via medialization laryngoplasty (Figure 1.3) is still an area of exploration.

Medialization laryngoplasty is a surgical procedure that aims to restore function to the larynx by moving the paralyzed vocal fold to the middle. When this occurs, the un-paralyzed side meets it in the middle for non-breathing functions, and results in complete closure. Several clinical studies have been conducted to study voice disorders such as UVFP, VF inflammation and scarring with varying new technologies such as endoscopic evaluation using an air pulse [112,124–126], which presents new data available for computational studies to compare to. One key parameter in clinical characterization of voice is the determination of phonation threshold pressure or PTP which is defined as the minimum lung pressure required to initiate and set the VFs in a sustained oscillation.

1.4 Present Approach and Key Accomplishments

This study presents a very first phonation model which encompasses a holistic computational approach and is suitable for perception, pathology and reconstruction study. We utilize a full body simulation approach to analyze phonation scenarios that have received limited attention or are accompanied by significant approximation. One such scenario includes age related differentiation of phonation characteristics. We have looked at the VF dynamics as well as the far-field acoustics for this aspect in detail. Another scenario concerns VF material property sensitivity, usually related to pathological conditions but also for healthy phonation. We examine not only the effect of VF material modeling and its impact on glottal aerodynamics, but also its impact on the sound field. A comparative study conducted to examine the effect of using a linear versus a finite deformation elastic model of the VFs resulted in an insignificant difference between the two. This provides a closure to the existing ambiguity in literature about the suitability of either model.

A study is presented with a more robust and experimentally verified viscoelastic model for the VF tissue. A baseline elastic only and a comparative study between viscoelastic and elastic only cases are performed.

Direct numerical simulation is employed to investigate voice disorder related to vocal fold (VF) stiffness asymmetry and unilateral vocal fold paralysis (UVFP). Additionally an analysis is performed for medialization laryngoplasty, a well known surgical treatment for UVFP. Phonation onset is determined from all the simulations as a measure of degree of voice disorder with phonation threshold pressure (PTP) as a key parameter for the quantification. Results obtained are consistent with data from clinical studies as well as similar past simulations.

A full body, fully-coupled fluid structure interaction based three-dimensional phonation study is analyzed. The simulation is carried out in two parts and both near VF flow dynamics and far-field acoustics have been studied. A comparison is drawn to current two-dimension simulations as well as data from literature. Results are in good agreement with previous three-dimensional phonation studies.

Chapter 2

Fluid Numerical Approach

The formulation of the fully coupled human phonation problem consists of two parts: fluid domain (for the flow of air inside the vocal tract) and the structure domain (motion of the vocal tract itself). The numerical approach for the fluid domain is formulated in this Chapter and the structural formulation is given in Chapter 3.

2.1 Fluid domain

The fluid model uses a fully compressible formulation of the Navier-Stokes equations. The conservation of mass, momentum and energy are given as follows:

$$\begin{aligned}
\frac{\partial \rho}{\partial t} + \frac{\partial}{\partial x_i}(\rho u_i) &= 0, \\
\frac{\partial \rho u_i}{\partial t} + \frac{\partial}{\partial x_j}\left(\rho u_i u_j + p\delta_{ij} - \tau_{ij}\right) &= 0, \\
\frac{\partial \rho E}{\partial t} + \frac{\partial}{\partial x_j}\left[\left(\rho E + p\right) u_j + q_j - u_i \tau_{ij}\right] &= 0,
\end{aligned} \tag{2.1}$$

Here ρ, $\rho \boldsymbol{u}$, $\rho E = p/(\gamma - 1) + \rho \boldsymbol{u} \cdot \boldsymbol{u}$, are the conserved variables representing density, specific momentum vector, and specific total energy, respectively. $\tau_{ij} = \mu(\partial u_i/\partial x_j + \partial u_j/\partial x_i) + \delta_{ij}\lambda \partial u_k/\partial x_k$ is the viscous stress tensor. μ, λ, and δ_{ij} are the first and second viscosity coefficients, and Kronecker delta, respectively. The thermodynamic pressure is given by p in Eq. (2.1) and the heat flux vector by $\boldsymbol{q}$. Repeated indices imply summation. Non-dimensionalizing Eq. (2.1) results in the following form for Reynolds and Prandtl numbers,

$$\mathrm{Re} = \frac{\tilde{\rho}_\infty \tilde{c}_\infty \tilde{L}}{\tilde{\mu}_\infty},$$

and

$$\mathrm{Pr} = \frac{\tilde{\mu}_\infty \tilde{C}_{p,\infty}}{\tilde{k}_\infty},$$

where the tilde denotes a dimensional quantity while subscript ∞ are the reference quantities. Other parameters in the above relations are a reference length L, speed of sound c, thermal conductivity k, and specific heat at constant pressure C_p.

In order to solve Eq. (2.1) on a non-uniform, non-orthogonal mesh in the physical domain we utilize smooth mappings that transform these equations to an equivalent conservative form in terms of computational variables $\boldsymbol{\xi}$ [127]. This mapping can be defined as

$$\boldsymbol{x} = \boldsymbol{X}(\boldsymbol{\xi}, \tau), \text{ with inverse } \boldsymbol{\xi} = \Xi(\boldsymbol{x}, t),$$

where $\boldsymbol{X}^{-1} = \Xi$, $\tau = t$, and Jacobian $J = |\partial \boldsymbol{X} / \partial \Xi|$.

Once in the computational domain, we use finite differences in order to approximate the spatial derivatives. High order summation-by-parts operators [128,129] are employed in combination with the simultaneous-approximation-term (SAT) boundary conditions [130–133]. This has been shown to yield a provably stable and accurate method [134]. Using this method, $\partial/\partial\xi$ can be approximated as $P^{-1}Q$, where Q has the property that $Q + Q^T = \mathrm{diag}(-1, 0, \ldots, 0, 1)$. The SAT formulation, being a penalization approach, is implemented by adding a penalty term to the right hand side of the governing equations. The final form of the penalized equation, as described in Svärd & Nordström [132] is given by

$$\frac{\partial \boldsymbol{q}}{\partial t} = \mathcal{F}(\boldsymbol{q}) + \sigma^{I1} P^{-1} E_1 A^{+}(\boldsymbol{q} - \boldsymbol{g}^{I1}) + \frac{\sigma^{I2}}{\mathrm{Re}} P^{-1} E_1 I (\boldsymbol{q} - \boldsymbol{g}^{I2}), \tag{2.2}$$

where only the left boundary terms are explicitly shown. The inviscid and viscous penalty parameters are given by σ^{I1} and σ^{I2} respectively, and $E_1 = (1, 0, \ldots, 0)^T$. Also $\mathcal{F}(\boldsymbol{q})$ denotes the divergence of the fluxes in the governing equations, A^{+} is a Roe matrix which will be be defined later, and I is an identity matrix.

In order to achieve numerical stability, $\sigma^{I1} \leq -2$ and

$$\sigma^{I2} \leq -\frac{1}{4P(1,1)} \max\left(\frac{\gamma\mu}{\mathrm{Pr}\rho}, \frac{5\mu}{3\rho}\right), \tag{2.3}$$

are required to be satisfied. We set both σ^{I1} and σ^{I2} to -2. Vectors $\boldsymbol{g}^{I1}$ and $\boldsymbol{g}^{I2}$ contain the boundary data. For the case of inviscid flows, the second penalty term is omitted and the target vector is defined as

$$\boldsymbol{g}^{I1} = \begin{bmatrix} \rho \\ \rho(\boldsymbol{u} - [(\boldsymbol{u}\cdot\boldsymbol{n}) - (\boldsymbol{u}_w\cdot\boldsymbol{n})]\boldsymbol{n}) \\ \rho e + \frac{1}{2}\rho|\boldsymbol{u} - [(\boldsymbol{u}\cdot\boldsymbol{n}) - (\boldsymbol{u}_w\cdot\boldsymbol{n})]\boldsymbol{n}|^2 \end{bmatrix}. \tag{2.4}$$

Defining matrix $A^+ = \chi\Lambda^+\chi^{-1}$, allows only the incoming characteristic variables $\boldsymbol{R} = \chi\boldsymbol{q}$. Here χ transforms the conserved variables $\boldsymbol{q}$ to characteristic variables $\boldsymbol{R}$. For the case of a calorically perfect gas χ is given by Pulliam & Chaussee [135], the Roe average of $\boldsymbol{q}$ and $\boldsymbol{g}^{I1}$ is used to evaluate χ. $\Lambda^+ = \Lambda - |\Lambda|$ is a diagonal matrix containing the elements $\Lambda = \mathrm{diag}\{\hat{U}, \hat{U}, \hat{U}+c, \hat{U}-c\}|\nabla_{\boldsymbol{x}}\xi|$ where $\hat{U}$ is the component of the velocity in the wall normal direction $\boldsymbol{n} = \nabla_{\boldsymbol{x}}\xi/|\nabla_{\boldsymbol{x}}\xi|$.

The viscous penalty term applies a no-slip, isothermal condition for a moving wall with velocity $\boldsymbol{u}_w(\boldsymbol{x}, t)$ and with temperature $T_w(\boldsymbol{x}, t)$, the target data are

$$\boldsymbol{g}^{I2} = [\rho,\, \rho\boldsymbol{u}_w,\, \rho e(T_w) + \frac{1}{2}\rho|\boldsymbol{u}_w|^2]^T, \tag{2.5}$$

We often require sponge regions to absorb and minimize reflections at outflow boundaries in the computational domain. The sponge region is implemented by adding a forcing term $-\eta(\boldsymbol{q} - \boldsymbol{q}_{ref})$ to the right hand side of Eq. (2.1). By penalizing the difference between the internal solution, $\boldsymbol{q}$, and a target solution, $\boldsymbol{q}_{ref}$ [136], the effect is desirably achieved. We can control the strength of this penalization by $\eta(s) = Ns^2$, where N is the sponge amplitude and s is the distance from the boundary normalized by the sponge length.

We compute the viscous terms in its strong form and approximating the spatial second derivatives by repeatedly applying the first derivative finite difference operators. This results in an increased computational efficiency as compared to the weak form where the second derivatives are in an expanded form. However, this comes at a cost: there is an absence of numerical damping at the highest wavenumber for the case of strong form leading to solution instabilities. This can be overcome by utilizing low-pass filters. We employ the implicit spatial filter by Lele [137], at each solution time step. Filtering is done by solving the linear system of equations resulting from the application of Eq. (2.6) to grid points i in each direction:

$$\alpha_f \hat{f}_{i-1} + \hat{f}_i + \alpha_f \hat{f}_{i+1} = a f_i + \frac{d}{2}(f_{i+3} + f_{i-3}) + \frac{c}{2}(f_{i+2} + f_{i-2}) + \frac{b}{2}(f_{i+1} + f_{i-1}), \tag{2.6}$$

Here a filtered quantity is denoted by $\hat{( )}$, while the filter accuracy is determined by a, b, c, and d which are functions of α_f which is a parameter governing the strength of the applied filter and its effect reduces as $\alpha_f \rightarrow 0.5$. For the entire work presented in this thesis, the value of α_f is chosen to be 0.49.

The fluid domain may consist of multiple blocks to accommodate complex geometries. Each block thus shares a common overlapping interface with the adjacent block. The coupling between the blocks requires a stable interface treatment as well as preserve conservation. This is accomplished by following a recent study [133] wherein conditions for stability and conservation of both viscous and inviscid fluxes in a SAT framework have been presented and verified.

In order to check the correctness of those conditions, we did both inviscid and viscous tests. First, for the inviscid test, we studied a vortex which was allowed to convect in a rectangular domain divided into two blocks with overlapping boundaries. Numerical result for contours of vorticity magnitude was plotted against the already available exact solution at the instant when the vortex reaches the center of the domain (where the interface resides). We observe an excellent match as shown in Figure 2.1.

After we established that the numerical solution matches well with the analytical solution, a test was done to see if the numerical solution follows the rate of convergence of the scheme being used for spatial discretization. In Figure 2.2 we plot the $||P||$-weighted L_2 norm of the error between the numerical and analytical solutions versus the grid resolution on a log-log scale. We can see that for a $2-4$ SBP scheme, the order of convergence for the numerical scheme is greater than 3, in accordance with the desired value [138].

Next we tested the viscous problem. We considered the case of Taylor-

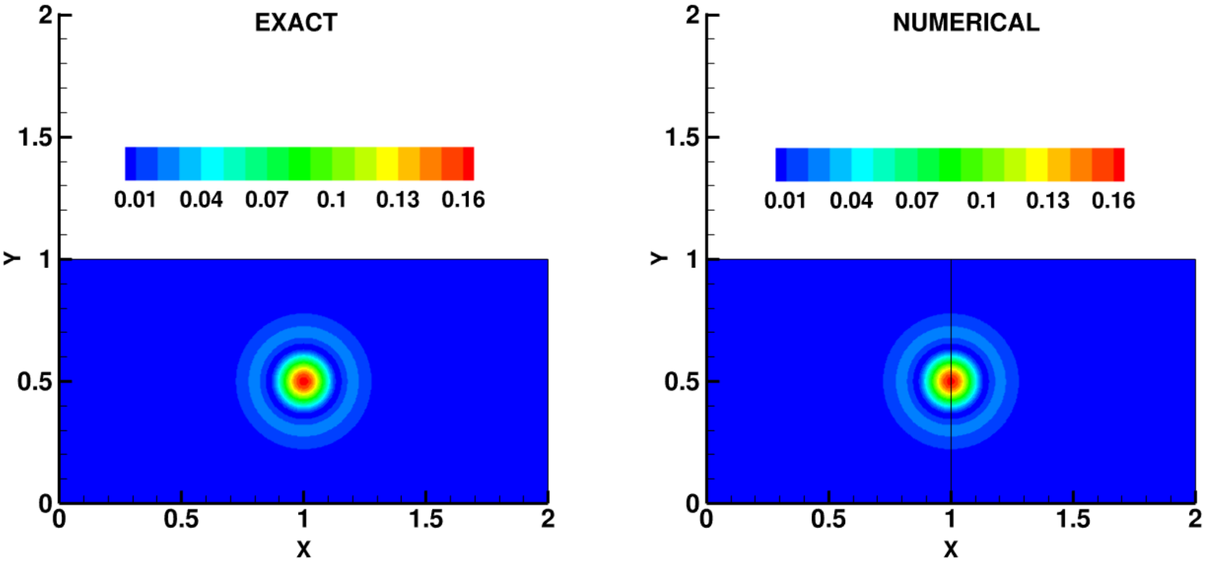

Figure 2.1: Sat Block Interface : Inviscid test, vorticity magnitude contours for convecting vortex.

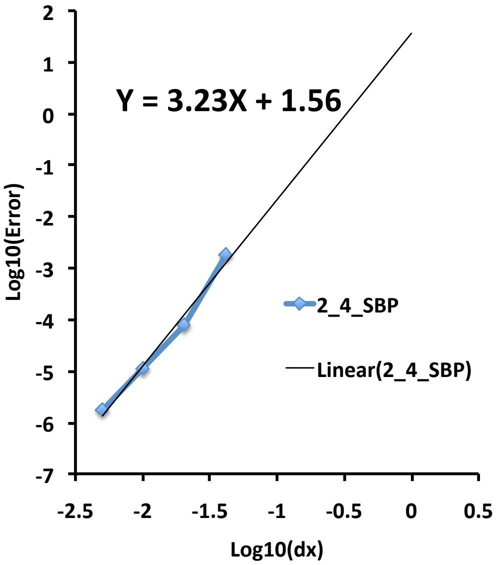

Figure 2.2: SAT Block Interface : Inviscid test, Rate of convergence with $2-4$ SBP Scheme.

Green vortex (TGV) for a Mach number $M = 0.05$. Analytical solution for TGV is available for an incompressible flow [139], which prompted the use of a very low Mach number for our simulation. The numerical solution for contours of pressure was plotted and compared to the analytical solution available, and the match was again excellent as can be seen in Figure 2.3.

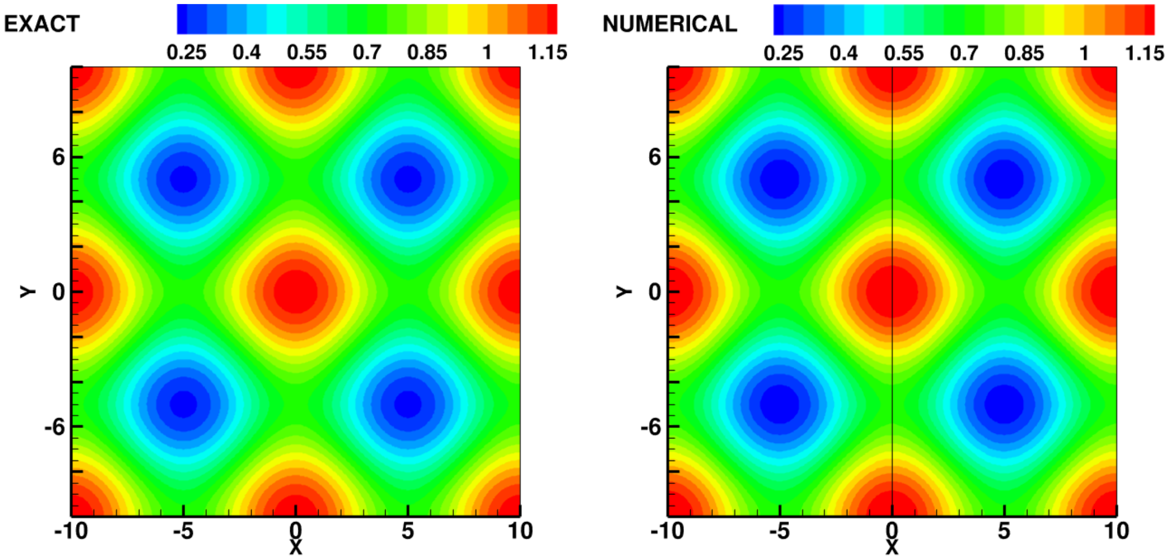

Figure 2.3: Sat Block Interface : Viscous test, Non-dimensional pressure contours for Taylor green vortex.

As reported earlier for an inviscid problem, the convergence test was now repeated for the viscous case described above. This time the order of convergence was nearly equal to 3, Figure 2.4, for a $2-4$ SBP scheme, again very close to the desired value.

The temporal advancement of Eq. (2.1) is accomplished using an explicit four-stage Runge Kutta method which is $O(\Delta t^4)$ accurate.

The fluids code has been used in a variety of fluid-only problems involving both laminar and turbulent flows [140–145].

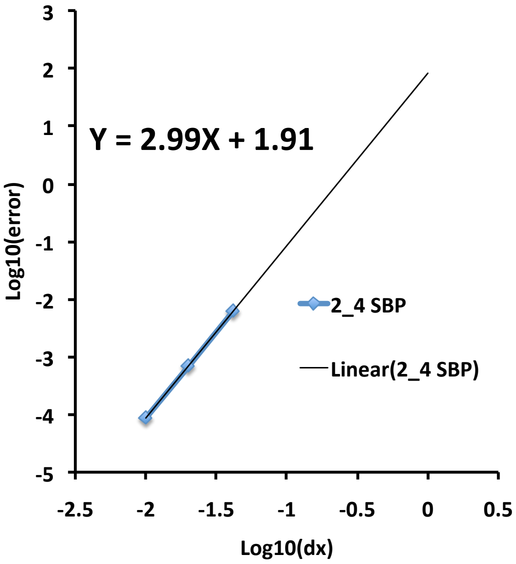

Figure 2.4: Sat Block Interface : Viscous test, Rate of convergence with $2-4$ SBP Scheme.

2.2 Fluid Grid Deformation

The fully coupled fluid-structure phonation problem involves significant deformation of the vocal tracts and hence necessitates the use of deforming grids for body-fitted meshes. We use a transfinite interpolation scheme to compute the grid coordinates after deformation, that works on the principle that the arclength-normalized coordinate of each point along its associated grid line is preserved. Details about this method can be found in [146]. Figure 2.5 is shown as an example of grid deformation.

The VFs undergo large deformation and as a result the fluid grid which conforms to the solid grid at the interface experiences these large deformations as well. The interior of the fluid grid can result in skewed cells due to large shear between two grid points. Elliptic PDEs generally result in smooth solutions which can be used as an advantage in large deformation mesh handling [147], and as such has been used in the current work.

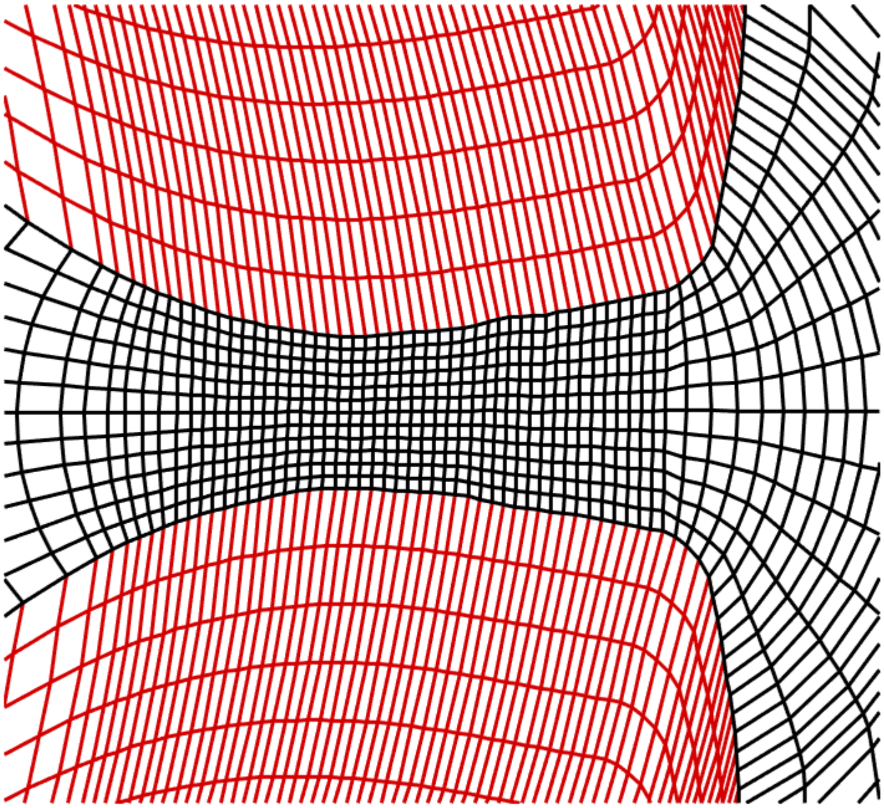

Figure 2.5: A 2D illustration the fluid grid (black) conforming to the motion of the solid grid (red) using transfinite interpolation.

Chapter 3

Structural Numerical Approach

3.1 Solid domain

A non-linear thermomechanical finite-element solver was used and verified [148] to compute the deformation of the vocal folds. However, the current configuration only utilizes the structural capabilities of the thermomechanical solver. The details of the solver and the method are described in the following sections.

3.1.1 Multiplicative decomposition

Here we will look at both the structural and thermal components of the solver. However, for our simulations we only utilize the structural capability of the current thermomechanical solver. Let us consider a body which can deform due to mechanical and thermal loading. With the initial configuration denoted by B_O, and $\boldsymbol{X}$ denoting the points on the body, at a later time t the body achieves a different configuration B wherein every point on the body can be denoted by $\boldsymbol{x} = \boldsymbol{\phi} = \boldsymbol{X} + \boldsymbol{u}$. Here $\boldsymbol{\phi}(\boldsymbol{X}, t)$, defines the transformation between the two configurations and $\boldsymbol{u}(\boldsymbol{x}, t)$ is the displacement. We can also define the deformation gradient as $\boldsymbol{F}(\boldsymbol{X}, t) = \nabla_{\boldsymbol{X}} \boldsymbol{\phi}(\boldsymbol{X}, t) = \partial \boldsymbol{x} / \partial \boldsymbol{X}$, and the right Cauchy-Green tensor as $\boldsymbol{C} = \boldsymbol{F}^T \boldsymbol{F}$. Also the volume change between the two configurations is represented by the Jacobian, $J = \det(\boldsymbol{F})$.

In the thermomechanical formulation as used currently, we can multiplicatively decompose the deformation gradient $\boldsymbol{F}$ into a stress-free component, ${}^{\theta}\boldsymbol{F}$, where all deformations are due to thermal expansion/contraction, and an isothermal component, ${}^{e}\boldsymbol{F}$, where deformations are produced by the stresses in the elastic body:

$$\boldsymbol{F} = {}^{\theta}\boldsymbol{F}^{e}\boldsymbol{F}. \tag{3.1}$$

This method of partitioning the problem is called an isothermal split [149]. Again, each component of the deformation gradient has an associated Jacobian, ${}^{\theta}J = \det({}^{\theta}\boldsymbol{F})$ and ${}^{e}J = \det({}^{e}\boldsymbol{F})$, which represent the volume changes due to thermal effects and stresses, respectively. We assume that the solid is thermally isotropic such that

$$ {}^{\theta}\boldsymbol{F} = \beta(\Theta)\boldsymbol{I}, \tag{3.2} $$

where $\boldsymbol{I}$ is the identity tensor and $\beta(\Theta)$ is the stretch ratio in any direction due to thermal expansion/contraction.

3.1.2 Isothermal stage

For the deformation problem shown in Figure 3.1, we apply the strong form of conservation of linear momentum in the current configuration, B, as

$$ \nabla \cdot \boldsymbol{\sigma} + \rho \boldsymbol{b} = \rho \ddot{\boldsymbol{u}}, \tag{3.3} $$

Here $\boldsymbol{\sigma}$ is the Cauchy stress tensor, $\boldsymbol{b}$ is a field of body forces, ρ is the density, $\ddot{\boldsymbol{u}} = \partial^2 \boldsymbol{u}/\partial t^2$ is the acceleration, and ∇ is the gradient in the current configuration. The principal of virtual work is correspondingly given by

$$ \delta W = \int_B (\nabla \cdot \boldsymbol{\sigma}) \cdot \boldsymbol{\delta u}\, dv + \int_B \rho \boldsymbol{b} \cdot \boldsymbol{\delta u}\, dv - \int_B \rho \ddot{\boldsymbol{u}} \cdot \boldsymbol{\delta u}\, dv = \boldsymbol{0}, \tag{3.4} $$

where $\boldsymbol{\delta u}$ denotes the virtual displacement. After some rearrangement and applying the divergence theorem $\int_v \nabla \cdot (\cdot) dv = \int_{\partial v} (\cdot) \cdot \hat{\boldsymbol{n}}\, da$, Eq. (3.4) yields the alternative form:

$$ \delta W = \int_B \boldsymbol{\sigma} : \nabla \boldsymbol{\delta u}\, dv + \int_B \rho \ddot{\boldsymbol{u}} \cdot \boldsymbol{\delta u}\, dv - \int_{\partial B_{\boldsymbol{t}}} \boldsymbol{t} \cdot \boldsymbol{\delta u}\, da - \int_B \rho \boldsymbol{b} \cdot \boldsymbol{\delta u}\, dv = \boldsymbol{0}, \tag{3.5} $$

where $\boldsymbol{t} = \boldsymbol{\sigma} \cdot \hat{\boldsymbol{n}}$ denotes the traction vector applied along the portion $\partial B_{\boldsymbol{t}}$ of the deformed boundary and $\hat{\boldsymbol{n}}$ is the outward pointing unit normal vector. To pull Eq. (3.5) back to the initial configuration, B_0, we use the following identities [150–152]:

$$
\begin{aligned}
\nabla\boldsymbol{\delta u} = \boldsymbol{F}^{-T}\nabla_{\boldsymbol{X}}\boldsymbol{\delta u} = \boldsymbol{F}^{-T}\boldsymbol{\delta F} &= {}^{e}\boldsymbol{F}^{-T\theta}\boldsymbol{F}^{-T}\boldsymbol{\delta F},\\
dv = JdV &= {}^{e}J^{\theta}JdV = \beta^{3}(\Theta)^{e}JdV,\\
\boldsymbol{t}da = \boldsymbol{t}J\sqrt{\boldsymbol{N}\cdot\boldsymbol{C}^{-1}\boldsymbol{N}}dA &= \boldsymbol{t}_0 dA,\\
{}^{\theta}\boldsymbol{F} &= \beta(\Theta)\boldsymbol{I},\\
\hat{\boldsymbol{P}} = \frac{\partial^{e}W}{\partial^{e}\boldsymbol{F}} &= {}^{e}J\sigma^{e}F^{-T},\\
\text{and}\quad \rho_0 &= J\rho.
\end{aligned}
\tag{3.6}
$$

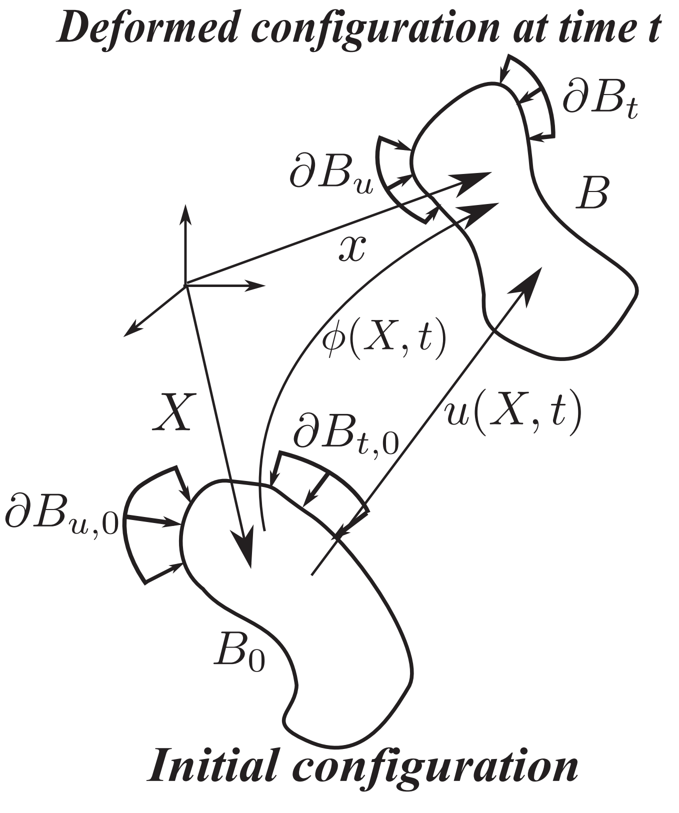

Figure 3.1: Schematic of the deformation gradient.

In Eq. (3.6), dv and dV are infinitesimal volume elements in the current and initial configurations, $\boldsymbol{N}$ is the unit outward pointing normal in the initial configuration, and $\hat{\boldsymbol{P}}$ is the first Piola-Kirchhoff stress tensor representing only stresses due to elastic deformations that take place during the isothermal stage. It can also be shown that the terms three and four in Eq. (3.5), when pulled back into the reference configuration, are

$$\int_{\partial B} \boldsymbol{t} \cdot \boldsymbol{\delta u} \; da + \int_{B} \rho \boldsymbol{b} \cdot \boldsymbol{\delta u} \; dv = \int_{\partial B_0} \boldsymbol{t}_0 \cdot \boldsymbol{\delta u} \; dA + \int_{B_0} \rho_0 \boldsymbol{b} \cdot \boldsymbol{\delta u} \; dV.$$

The expression of the first term in the undeformed configuration is derived as follows:

$$\int_{B} \boldsymbol{\sigma} : \nabla \boldsymbol{\delta u} \; dv = \int_{B_0} J \boldsymbol{\sigma} : \nabla \boldsymbol{\delta u} \; dV = \int_{B_0} J \boldsymbol{\sigma}^e \boldsymbol{F}^{-T} : {}^{\theta}\boldsymbol{F}^{-T} \boldsymbol{\delta F} \; dV$$

$$= \int_{B_0} {}^{\theta}J^e J \boldsymbol{\sigma}^e \boldsymbol{F}^{-T} : {}^{\theta}\boldsymbol{F}^{-T} \boldsymbol{\delta F} \; dV = \int_{B_0} {}^{\theta}J \hat{\boldsymbol{P}} : {}^{\theta}\boldsymbol{F}^{-T} \boldsymbol{\delta F} \; dV$$

$$= \int_{B_0} \beta^3(\Theta) \hat{\boldsymbol{P}} : \frac{\boldsymbol{I}}{\beta(\Theta)} \boldsymbol{\delta F} \; dV = \int_{B_0} \beta^2(\Theta) \hat{\boldsymbol{P}} : \boldsymbol{\delta F} \; dV.$$

It is also straightforward to derive the acceleration term:

$$\int_{B} \rho \ddot{\boldsymbol{u}} \cdot \boldsymbol{\delta u} \; dv = \int_{B_0} \rho_0 \ddot{\boldsymbol{u}} \cdot \boldsymbol{\delta u} \; dV.$$

This leads to the principle of virtual work in the reference configuration, B_0, as

$$\delta W = \int_{B_0} \beta^2(\Theta) \hat{\boldsymbol{P}} : \boldsymbol{\delta F} \; dV + \int_{B_0} \rho_0 \ddot{\boldsymbol{u}} \cdot \boldsymbol{\delta u} \; dV - \int_{\partial B_0} \boldsymbol{t}_0 \cdot \boldsymbol{\delta u} \; dA - \int_{B_0} \boldsymbol{b}_0 \cdot \boldsymbol{\delta u} \; dV = 0. \quad (3.7)$$

Equation (3.7) shows that using the multiplicative decomposition of the deformation gradient allows for a standard elastic constitutive model to be used to calculate the first Piola-Kirchhoff stress tensor in the isothermal stage. The full expression of the first Piola-Kirchhoff stress tensor is the product $\beta^2(\Theta)\hat{\boldsymbol{P}}$.

Non-linear solution method

For a non-linear problem, it is quite possible that a body with current configuration $\boldsymbol{x}$ does not satisfy $\delta W(\boldsymbol{u}) = 0$. In that case, a linear correction is applied, i.e., δW is linearized at $\boldsymbol{u}$ and multiplied by a correction $\Delta \boldsymbol{u}$ to achieve $\delta W(\boldsymbol{u}+\Delta\boldsymbol{u})=0$,

$$\delta W(\boldsymbol{u}+\Delta\boldsymbol{u})=0\approx L[\delta W]=\delta W(\boldsymbol{u})+D\delta W(\boldsymbol{u})[\Delta\boldsymbol{u}]=0 \tag{3.8}$$

where $D\delta W(\boldsymbol{u})[\Delta\boldsymbol{u}]$ is the directional derivative of $W(\boldsymbol{u})$ along $\Delta\boldsymbol{u}$. The terms which are involved in the linearization are the internal stress and traction terms,

$$L[\delta W]=\delta W(\boldsymbol{u})+D\delta W_{int}(\boldsymbol{u})[\Delta\boldsymbol{u}]-D\delta W_{ext}(\boldsymbol{u})[\Delta\boldsymbol{u}]=0,$$

which are described below. The corrected configuration $\boldsymbol{u}=\boldsymbol{u}_{old}+\Delta\boldsymbol{u}$ is found by solving for $\Delta\boldsymbol{u}$

$$D\delta W_{int}(\boldsymbol{u})[\Delta\boldsymbol{u}]-D\delta W_{ext}(\boldsymbol{u})[\Delta\boldsymbol{u}]=-\delta W(\boldsymbol{u}), \tag{3.9}$$

and iterating until $\delta W(\boldsymbol{u})=0$.

Linearization of δW

The internal virtual work is given by the term

$$\delta W_{int}=\int_{B_0}\beta^2(\Theta)\hat{\boldsymbol{P}}:\boldsymbol{\delta F}dV.$$

The term is linearized by taking the directional derivative along a displacement, $\Delta\boldsymbol{u}$, as

$$D\delta W_{int}[\Delta\boldsymbol{u}]=\int_{B_0}\beta^2(\Theta)\boldsymbol{\delta F}:D\hat{\boldsymbol{P}}[\Delta\boldsymbol{u}]dV. \tag{3.10}$$

Using

$$D\hat{\boldsymbol{P}}[\Delta\boldsymbol{u}]=\frac{\partial\hat{\boldsymbol{P}}}{\partial^e\boldsymbol{F}}:D^e\boldsymbol{F}[\Delta\boldsymbol{u}]=\mathcal{A}:D^e\boldsymbol{F}[\Delta\boldsymbol{u}]$$

and

$$D^e\boldsymbol{F}[\Delta\boldsymbol{u}]=\nabla_{\boldsymbol{X}}\Delta\boldsymbol{u}, \tag{3.11}$$

the linearized term takes the form

$$\int_{B_0}\beta^2(\Theta)\boldsymbol{\delta F}:D\hat{\boldsymbol{P}}[\Delta\boldsymbol{u}]dV=\int_{B_0}\beta^2(\Theta)\boldsymbol{\delta F}:\mathcal{A}:\nabla_{\boldsymbol{X}}\Delta\boldsymbol{u}dV. \tag{3.12}$$

The expressions of $\hat{\boldsymbol{P}}$ and $\boldsymbol{\mathcal{A}}$ for the St. Venant-Kirchhoff and Neo-Hookean constitutive models are given in Section 3.2 and Appendix A.1, respectively. Similarly, the external virtual work term,

$$\delta W_{ext} = \int_{\partial B_0} \boldsymbol{t}_0 \cdot \boldsymbol{\delta u} \; dA,$$

is linearized by taking the directional derivative along $\boldsymbol{u}$ as

$$D\delta W_{ext}[\Delta \boldsymbol{u}] = \int_{\partial B_0} \boldsymbol{\delta u} \cdot D\boldsymbol{t}_0[\Delta \boldsymbol{u}] \; dA, \tag{3.13}$$

where,

$$D\boldsymbol{t}_0[\Delta \boldsymbol{u}] = \frac{\partial}{\partial {}^e\boldsymbol{F}} \left(\boldsymbol{t} \; {}^e J \sqrt{\boldsymbol{N} \cdot \boldsymbol{C}^{-1} \boldsymbol{N}} \right) : D\,{}^e\boldsymbol{F}[\Delta \boldsymbol{u}] = \boldsymbol{\mathcal{B}} : \nabla_{\boldsymbol{X}} \Delta \boldsymbol{u}, \tag{3.14}$$

where $\boldsymbol{\mathcal{B}}$ is given in Appendix A.2.

The resulting linearized equation is given as

$$\begin{aligned} L[\delta W(\boldsymbol{u})] = & \int_{B_0} \beta^2(\Theta) \hat{\boldsymbol{P}} : \boldsymbol{\delta F} \; dV + \int_{B_0} \rho_0 \ddot{\boldsymbol{u}} \cdot \boldsymbol{\delta u} \; dV \\ & - \int_{\partial B_0} \boldsymbol{t}_0 \cdot \boldsymbol{\delta u} \; dA - \int_{B_0} \boldsymbol{b}_0 \cdot \boldsymbol{\delta u} \; dV \\ & + \int_{B_0} \beta^2(\Theta) \boldsymbol{\delta F} : \boldsymbol{\mathcal{A}} : \nabla_{\boldsymbol{X}} \Delta \boldsymbol{u} \; dV \\ & - \int_{\partial B_0} \boldsymbol{\delta u} \cdot \boldsymbol{\mathcal{B}} : \nabla_{\boldsymbol{X}} \Delta \boldsymbol{u} \; dA = 0. \end{aligned} \tag{3.15}$$

The discretized form for Eq. (3.15) yields

$$\boldsymbol{\delta u}^T \left(\boldsymbol{R}^{int} + \boldsymbol{M} \ddot{\boldsymbol{u}} - \boldsymbol{R}^{tract.} - \boldsymbol{R}^{body} + \boldsymbol{K} \Delta \boldsymbol{u} \right) = \boldsymbol{0}, \tag{3.16}$$

where $\boldsymbol{R}^{int.}$ is the internal load vector, $\boldsymbol{M}$ is the consistent mass matrix, $\boldsymbol{R}^{tract.}$ and $\boldsymbol{R}^{body}$ are the external load vectors due to traction and body forces, respectively, and $\boldsymbol{K}$, the tangent stiffness matrix, represents the linearized internal and external virtual work terms. A detailed description of the spatial discretization is given in Appendix A.4.

3.2 Constitutive models

In the geometrically non-linear regime, a hyperelastic constitutive model is derived from the function $w(\boldsymbol{X}, \boldsymbol{F})$, the stored energy per unit volume in the reference configuration. The stored energy function is often expressed in terms of the right Cauchy-Green strain, $w(\boldsymbol{F}) = \hat{w}(\boldsymbol{C})$, or, in the case of isotropic materials, the the invariants of $\boldsymbol{C}$, $\bar{w}(I_1, I_2, I_3)$. The three invariants are $I_1 = \mathrm{Tr}(\boldsymbol{C})$, $I_2 = 1/2(\mathrm{Tr}(\boldsymbol{C})^2 - \mathrm{Tr}(\boldsymbol{C}^2))$, and $I_3 = det(\boldsymbol{C}) = J^2$. Expressing w in terms of the invariants is useful when taking derivatives of W. For example, the second Piola-Kirchhoff stress tensor is given as

$$\boldsymbol{S} = 2\frac{\partial \hat{w}}{\partial \boldsymbol{C}} = 2\sum_{j=1}^{3} \frac{\partial \bar{w}}{\partial I_j}\frac{\partial I_j}{\partial \boldsymbol{C}}. \tag{3.17}$$

3.2.1 St. Venant-Kirchhoff constitutive model

The St. Venant-Kirchhoff model has the stored energy function

$$\hat{w} = \frac{\mu}{2}\mathrm{Tr}\left(\frac{\boldsymbol{C} - \boldsymbol{I}}{2}\right) + \frac{\lambda}{8}\left(\mathrm{Tr}(\boldsymbol{C}) - 3\right)^2, \tag{3.18}$$

where λ and μ are Lamѐ's first and second parameters, respectively. From Eq. (3.17), the second Piola-Kirchhoff stress tensor is found to be

$$\boldsymbol{S} = [\lambda \mathrm{Tr}(\boldsymbol{E})\boldsymbol{I} + 2\mu\boldsymbol{E}]. \tag{3.19}$$

The first Piola-Kirchhoff stress tensor can be shown to be $\boldsymbol{P} = \boldsymbol{F}\boldsymbol{S}$. Given an energy functional, w, the first Piola-Kirchhoff stress tensor is defined as

$$P_{iK} = \frac{\partial w}{\partial F_{iK}} = \frac{\partial \hat{w}}{\partial C_{JP}}\frac{\partial C_{JP}}{\partial F_{iK}}, \tag{3.20}$$

where $\boldsymbol{C} = \boldsymbol{F}^T\boldsymbol{F}$ is the right Cauchy-Green tensor and $\boldsymbol{S} = 2\dfrac{\partial w}{\partial \boldsymbol{C}}$. Further manipulation gives

$$\frac{\partial C_{JP}}{\partial F_{iK}} = \frac{\partial}{\partial F_{iK}}(F_{jJ}F_{jP}) = \frac{\partial}{\partial F_{iK}}(\delta_{ij}\delta_{KJ}F_{jP} + \delta_{ij}\delta_{KP}F_{jJ}) = \frac{\partial}{\partial F_{iK}}(\delta_{KJ}F_{iP} + \delta_{KP}F_{iJ}). \tag{3.21}$$

Considering the symmetry of the right Cauchy-Green tensor

$$\begin{aligned} P_{iK} &= \frac{\partial \hat{w}}{\partial C_{JP}}(\delta_{KJ}F_{iP} + \delta_{KP}F_{iJ}) \\ &= \frac{\partial \hat{w}}{\partial C_{JP}}\delta_{KJ}F_{iP} + \frac{\partial \hat{w}}{\partial C_{JP}}\delta_{KP}F_{iJ} \\ &= 2F_{iP}\frac{\partial \hat{w}}{\partial C_{KP}} = F_{iP}S_{KP}. \end{aligned} \tag{3.22}$$

Therefore,

$$\boldsymbol{P} = \boldsymbol{F}[\lambda tr(\boldsymbol{E})\boldsymbol{I} + 2\mu\boldsymbol{E}]. \tag{3.23}$$

3.2.2 Modified Neo-Hookean constitutive model

The stored energy function for the modified Neo-Hookean model is given by

$$\bar{w}(I_1, I_2, I_3) = \frac{G}{2}(\tilde{I}_1 - 3) + \frac{K}{2}(J-1)^2, \tag{3.24}$$

where, $\tilde{I}_1 = I_1/J^{1/3} = I_1/I_3^{2/3}$ is the deviatoric expression of the first invariant of $\boldsymbol{C}$ and

$$G = \frac{E}{2(1-\nu)}$$

and

$$K = \frac{E}{3(1-2\nu)}$$

are the shear and bulk moduli, respectively. For this class of materials, the second Piola-Kirchhoff stress tensor is given by

$$\boldsymbol{S} = 2\frac{\partial \hat{w}}{\partial \boldsymbol{C}} = G\, J^{-2/3}\left(1 - \frac{\mathrm{Tr}(\boldsymbol{C})\boldsymbol{C}^{-1}}{3}\right) + K(J^2 - J)\boldsymbol{C}^{-1} \tag{3.25}$$

3.2.3 Viscoelasticity model

For the viscoelastic case, the stored energy function can be split into the elastic and viscoelastic components as follows,

$$\hat{w} = w^{el} + w^{vis} \tag{3.26}$$

The elastic component can be further split into volumetric and isochoric parts,

$$w^{el} = w_{vol} + w_{iso}^{\infty} \tag{3.27}$$

Holzapfel [153] observed that w^{vis} is proportional to w_{iso}^{∞} and the proportionality factor is given by β^{∞}, which is the non-dimensional free-energy factor associated with the stress relaxation time τ. In viscoelasticity stress relaxation time τ is referred to the characteristic time required for the material to relax from a deformed state to its equilibrium configuration. Using the above, the second Piola-Kirchhoff stress tensor $\boldsymbol{S}$ (which is related to the first Piola-Kirchhoff stress tensor as $\boldsymbol{P} = \boldsymbol{F}\boldsymbol{S}$) can be additively split into elastic and viscoelastic components as follows,

$$\boldsymbol{S} = \tilde{\boldsymbol{S}} + \boldsymbol{Q} \tag{3.28}$$

where,

$$\tilde{\boldsymbol{S}} = \boldsymbol{S_{vol}} + \boldsymbol{S_{iso}^{\infty}}. \tag{3.29}$$

Here $\tilde{\boldsymbol{S}}$ is composed of only the elastic components, namely the volumetric stress $\boldsymbol{S_{vol}}$ and the isochoric stress $\boldsymbol{S_{iso}^{\infty}}$, while $\boldsymbol{Q}$ represents viscoelastic isochoric component. Hence, $\boldsymbol{S_{vol}}$, $\boldsymbol{S_{iso}^{\infty}}$ are obtained directly through a elastic model while $\boldsymbol{Q}$ is obtained numerically after solving the desired viscoelastic model. In the present case, the time evolution of $\boldsymbol{Q}$ in terms of $\boldsymbol{S_{iso}^{\infty}}$ is given as follows,

$$\frac{d\boldsymbol{Q}}{dt} + \frac{\boldsymbol{Q}}{\tau} = \beta^{\infty}\frac{d\boldsymbol{S_{iso}^{\infty}}}{dt} \tag{3.30}$$

For a detailed derivation of Eq. (3.30) see [153]. $\boldsymbol{Q}$ is obtained by integrating Eq. (3.30) and then using the mid-point rule and the mean value theorem to march ahead in time. It is to be noted that the time history of $\boldsymbol{Q}$ needs to be stored in order to march forward. The final expression for $\boldsymbol{Q}(t_{n+1})$ is obtained as;

$$\boldsymbol{Q}(t_{n+1}) = \exp(\xi)\boldsymbol{Q}(t_n) + \beta^{\infty}\exp(\xi/2)[\boldsymbol{S_{iso}^{\infty}}(t_{n+1}) - \boldsymbol{S_{iso}^{\infty}}(t_n)] \tag{3.31}$$

where $\xi = -\Delta t/\tau$. Once $\boldsymbol{Q}$ is obtained, it is added to the elastic component using Eq. (3.28) to obtain the total stress. A detailed solver verification of the above viscoelastic model implementation is presented in Chapter. 5.

Temporal discretization

The dynamic equilibrium equation at time step $n+1$ is

$$\boldsymbol{R}_{n+1}^{int} - \boldsymbol{R}_{n+1}^{ext} + \boldsymbol{M}\ddot{\boldsymbol{u}}_{n+1} = \boldsymbol{0} \tag{3.32}$$

Newmark's method is used to advance Eq. (3.32) in time, in which the solution at time step $n+1$ is approximated by

$$\begin{aligned} \boldsymbol{u}_{n+1} &= \boldsymbol{u}_n + \Delta t \dot{\boldsymbol{u}}_n + \frac{\Delta t^2}{4}[(1-2\beta)\ddot{\boldsymbol{u}}_n + 2\beta\ddot{\boldsymbol{u}}_{n+1}], \\ \dot{\boldsymbol{u}}_{n+1} &= \dot{\boldsymbol{u}}_n + \Delta t[(1-\gamma)\ddot{\boldsymbol{u}}_n + \gamma\ddot{\boldsymbol{u}}_{n+1}], \end{aligned} \tag{3.33}$$

where $\gamma = 1/2$ and $\beta = 1/4$ are chosen to give an $\mathcal{O}(\Delta t^2)$ accurate, linearly stable scheme. Plugging Eq. (3.33) into Eq. (3.32) and approximating the internal load vector at time step $n+1$ as $\boldsymbol{R}_{n+1}^{int} = \boldsymbol{R}_n^{int} + \boldsymbol{K}\Delta\boldsymbol{u}$ results in

$$\boldsymbol{R}_{n+1}^{ext} - \boldsymbol{R}_n^{ext} + M\left(\frac{4}{\Delta t}\dot{\boldsymbol{u}}_n + 2\ddot{\boldsymbol{u}}_n\right) = \left(\frac{4}{\Delta t^2}\boldsymbol{M} + \boldsymbol{K}\right)\Delta\boldsymbol{u}$$

The solution, $\Delta\boldsymbol{u}$, is used to calculate the solution at $n+1$

$$\begin{aligned} \boldsymbol{u}_{n+1} &= \boldsymbol{u}_n + \Delta\boldsymbol{u}, \\ \dot{\boldsymbol{u}}_{n+1} &= \dot{\boldsymbol{u}}_n + \frac{2}{\Delta t}\Delta\boldsymbol{u}, \\ \ddot{\boldsymbol{u}}_{n+1} &= \ddot{\boldsymbol{u}}_n + \frac{4}{\Delta t^2}\Delta\boldsymbol{u}. \end{aligned}$$

Newton-Raphson iterations are used until Eq. (3.32) is satisfied to a tolerance of 10^{-5}.

3.3 Interface treatment

There is a weak coupling between the individual fluid and structural solvers at the interface where the fluid and structure domains meet. We solve for the fluid and structural domains independently at a given time step $t_n = n\Delta t$. At the interface, the spatial coupling is obtained by matching nodes between the two domains. Displacement and velocities, which are Dirichlet quantities are passed from the solid to the fluid side, while the Neumann quantities, like traction, are passed from the fluid to the solid side [154]. The stability benefits of the implicit thermomechanical solver are exploited in this choice of the physical quantities to pass at the fluid-solid interface [154]. Furthermore, it is shown in Appendix A.3 that it is less cumbersome to pass the Cauchy stress tensor, $\boldsymbol{\sigma}$, from the fluid solution to the solid domain, instead of the traction, $\boldsymbol{t} = \boldsymbol{\sigma} \cdot \hat{\boldsymbol{n}}$.

The presence of highly disparate time scales involved in the fluid-structure interaction problem poses a significant computational resource challenge. The transient solution in the solid evolves much more slowly than the solution on the fluid side. This results in prohibitively high computational costs. Also, the current fluid solver has an explicit time advancement scheme, as compared to the implicit one in the structural solver. This exacerbates the effect due to the stringent stability requirements associated with the explicit time advancement. In order to lessen these issues and advance the coupled system more efficiently without affecting the stability and accuracy requirements of the solvers, we use different time step sizes in the fluid and structural domains. This method is $\mathcal{O}(\Delta t_c)$ accurate, where Δt_c is the coupling step size.

As indicated, it is likely that the time step size is smaller in the fluid. Information is linearly interpolated between time steps when needed. The time step ratios are chosen so that their effect on the solution does not affect the quantities of interest. A verification study utilizing different time step sizes in the fluid and solid stages has been presented in [148] wherein a 2D simulation of a laminar boundary layer over a structurally complaint beam was conducted. A time step ratio of $SF = \Delta t_{solid}/\Delta t_{fluid} = 10/1$ was found to produce negligible errors, and the same is used in this study. We verified this through one of our simulations, wherein we ran a full body adult phonation case with Poisson's ratio of 0.27 (for details of the simulation setup and results, please refer to Chapter. 4) first with $SF = 1$, and then switched to $SF = 10$ and again back to $SF = 1$. Figure 3.2 plots the result for upstream gauge pressure and left VF gap from centerline for one of our phonation simulation studies. We notice negligible errors for $SF = 10$ time step ratio. This is particularly an important result, as for the phonation simulations, the vocal folds come very close for a certain duration in each oscillation cycle, leading to great reduction in fluid step size. We obtained a speed-up of approximately 5 with $SF = 10$ as compared to the $SF = 1$ case. This is a significant computational gain.

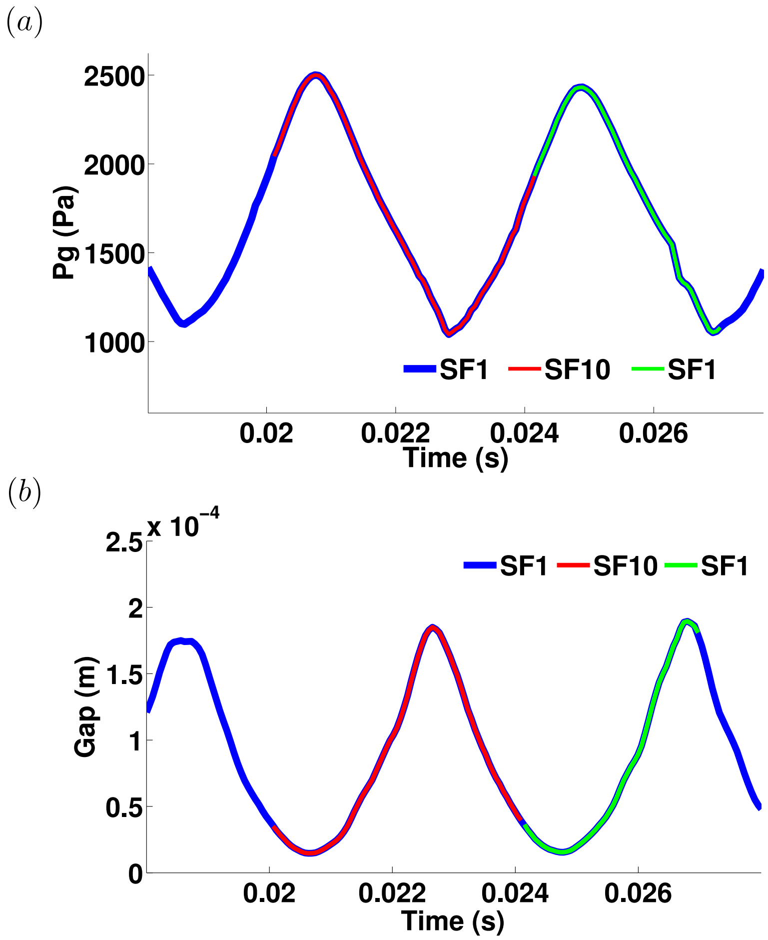

Figure 3.2: Comparison of structural to fluid time step $SF = 1$ and $SF = 10$ for adult phonation simulation with Poisson's ratio= 0.27: (a) Upstream gauge pressure variation, (b) Left VF gap from centerline.

Chapter 4

Full Body Simulation in 2D

In this chapter we attempt to examine an important aspect missing in computational phonation studies which is characterization of the sound field ultimately heard by a listener. Directly predicting the exterior sound field requires either a simulation with a domain that encompasses regions outside the speaker's mouth, which we term a 'full body' simulation. The domain for the simulations used in this chapter is shown in Figure 4.1 which is a full body domain with anatomically representative vocal tract geometry, which would not only capture the near VF flow dynamics, but also the far field acoustic signatures.

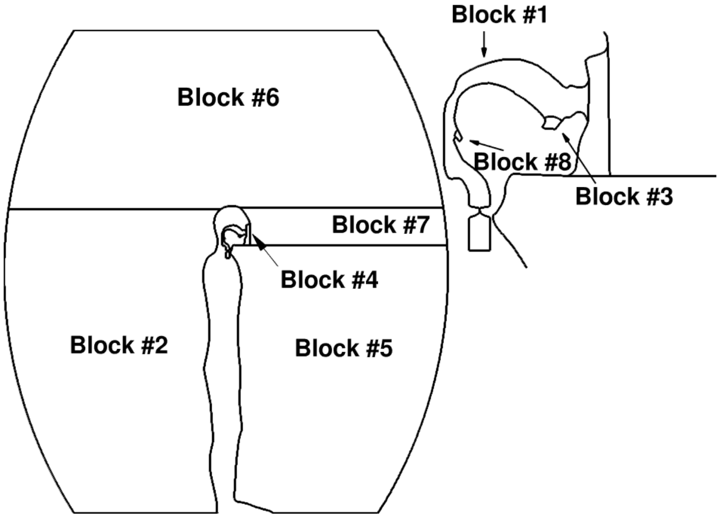

Figure 4.1: Multiple grid blocks used to create the human adult domain.

4.1 Quasi 1D Boundary Condition

This section describes the methodology used to generate the inflow conditions at the lung exit for our phonation simulations. Prior studies normally applied a constant pressure boundary condition to model the output of the lungs to the subglottis. A recent review paper [155] has questioned the appropriateness of such a boundary condition. The question raises a valid doubt as to whether the lung pressure remains constant or respond to the VF vibration during phonation. As a result, we developed a new boundary condition using the quasi one-dimensional approach and assume that a constant inflow flow rate and outflow pressure (atmospheric) are given as input. The inflow pressure is obtained from the Mach number variation calculated by solving Eq. (4.1) numerically at each time step,

$$\frac{dM^2}{dx} = G(M)\left[-\frac{2}{A}\frac{\partial A}{\partial x} + H(M, A, f)\right], \tag{4.1}$$

with $P_{outflow} = P_{atm}, U_{inflow} = 1m/s$, (For the glottal flow rate of 160-200 cm^2/s [71], U_{inflow} comes out to be approximately 1 m/s). Here A is the variation of glottal area along the vocal tract, f is the fanning friction factor and γ the ratio of specific heats. The functions G and H are given by:

$$G(M) = \frac{M^2[1 + (\gamma - 1)M^2/2]}{1 - M^2} \tag{4.2}$$

$$H(M, A, f) = \gamma M^2 fP/A \tag{4.3}$$

We have also done a comparative study for both quasi 1D and constant inflow boundary conditions. Results for this study have been discussed in Appendix B.1.1 .

With the description of the fluid and structural numerical approach provided in the previous chapters, we now examine several simulation cases for human phonation.

4.2 Full body Simulation of Human Adult

It has been observed [156] that the cross-section area variation of the vocal tract has a significant impact on the actual sound produced, a feature combined in our full body domain. We directly compute the acoustic field past the speaker's mouth instead of propagating the sound calculated inside the vocal tract to the outside by an acoustic analogy or other approximate method [156].

A total of eight blocks were used (Figure 4.1) to create the full body domain and the vocal tract. In Table 4.1, we provide the grid counts for each of the blocks.

Table 4.1: Adult full body grid sizes.

Block	N_1	N_2
1	2194	121
2	742	390
3	30	32
4	251	48
5	747	536
6	300	909
7	329	390
8	50	45

Table 4.2: VF material properties.

Layer	Young's modulus (kPa)	Poisson ratio
Cover	25	0.27, 0.47
Ligament	100	0.27, 0.47
Body	50	0.27, 0.47
Cartilage	250	-

The inflow boundary (exit of lung) is specified with the time-dependent pressure obtained via the quasi-1D formulation described in Sec. 4.1. The outer boundaries are maintained at atmospheric condition. The domain encompasses sufficient space for acoustic waves to propagate. The various blocks overlap with adjacent ones at the interface via body-fitted grid points.

For modeling the VFs, we use a three layer model composed of the cover, ligament and the body as shown in Figure 4.2. The VF layers terminate into a stiff cartilage after transitioning smoothly through a transition layer. The material properties of the VFs are given in Table 4.2. The values of the material parameters are motivated by [72] and are relatively stiffer than usual. The primary reason for this stiffening was to compensate for the longitudinal stretching and 3-D shear in the VFs during deformation due to anterior/posterior attachment to the cartilage which cannot be directly incorporated in the 2-D model. This was validated in [72] by conducting an eigenmode analysis of the stiffened 2-D VFs and comparing the results against the 3-D counterparts. Also the Poisson's ratio value used in that study is 0.3, which is significantly lower than the incompressible limit of 0.5. The VFs are likely nearly incompressible elements [53, 88–90], Poisson's ratio values of as low as 0.27 have been used in several phonation simulations [71, 72, 91, 92]. To examine the effect of this large variation in Poisson's ratio on phonation characteristics, we consider two Poisson's ratio cases for our analysis, namely, $\nu = 0.27$ and 0.47.

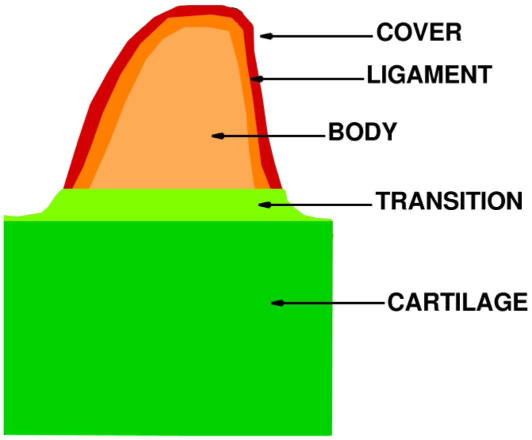

Figure 4.2: VF model showing the different layers.

Figure 4.3 shows the vorticity ($\boldsymbol{\omega} = \nabla \times \boldsymbol{u}$) contours and the corresponding VF motions for one full cycle for the two Poisson's ratio cases. The VFs do not collide during oscillation due to lubrication effect which results in an increase in pressure in the glottis when the VFs come very close to each other (or when (minimum VF gap)/(characteristic length scale 'L') $\ll 1$), that eventually pulls them apart. A simple validation of this idea based on lubrication theory is presented in the Appendix. The flow in the small gap is viscous dominated and the resulting glottal flow exhibits unsteadiness as shown by the vorticity contours. Also, there is an underlying asymmetry in the flow past the glottis. The eddies past the VFs curl up from one VF to the other without any bias. This phenomenon has been observed in previous two-dimensional simulation studies [30–32, 40, 41, 45, 72]. This asymmetry has been attributed to jet confinement, its pulsatility and the intrinsic instabilities of the glottal jet itself [75, 157]. Figure 4.4 shows the VF motion for one cycle for the two Poisson's ratio cases. When comparing the two Poisson's ratio cases, the following can be clearly observed. First, the Poisson's ratio close to incompressibility limit, shows the presence of the mucosal wave with clear convergent-divergent VF shapes during the opening and closing phase of the VF motion [158] as compared to mostly a lateral deformation observed for the lower Poisson's ratio case [71]. Second, the amplitude of VF oscillation is clearly higher for the lower Poisson's ratio case and so has been reported in one parametric study [93] where the Poisson's ratio was varied from 0.4 to 0.499.

Figure 4.5 shows minimum VF gap from centerline for the two Poisson's ratio cases. The VF amplitude of motion is inversely related to the Poisson's ratio as was noted in Figure 4.3. The dominant frequency of oscillation indicated by the peak in the FFT plot, is also an inverse function of the Poisson's ratio. Shurtz and Thomson [93] observed similar trend with their parametric study. Also worth noting is that the higher Poisson's ratio case with presence of mucosal wave presents a more non-uniform VF motion with time as opposed to the lower Poisson's ratio case with inherently dominant lateral motion. The frequency of oscillation are on the higher side due to the VF stiffening as mention earlier, yet the values are within phonation limits [158].

Figure 4.6 and Figure 4.7 show the time-averaged flow features for the two Poisson's ratio cases. A pair of large recirculation zones reside on the two sides of the jet. It is clearly observed that the bending of the vocal tract on the lower edge, which appears earlier than the upper edge, pushes the lower high circulation region downstream. For the higher Poisson's ratio case as shown in Figure 4.7 this lower recirculation region is very strong and pushes the jet to bend strongly towards the upper edge of the vocal tract. Even though the average is taken over 8 cycles, the mean flow is still highly asymmetric about the centerline for both the Poisson's ratio cases. This is due to the stochastic nature and the large time-scales present in the

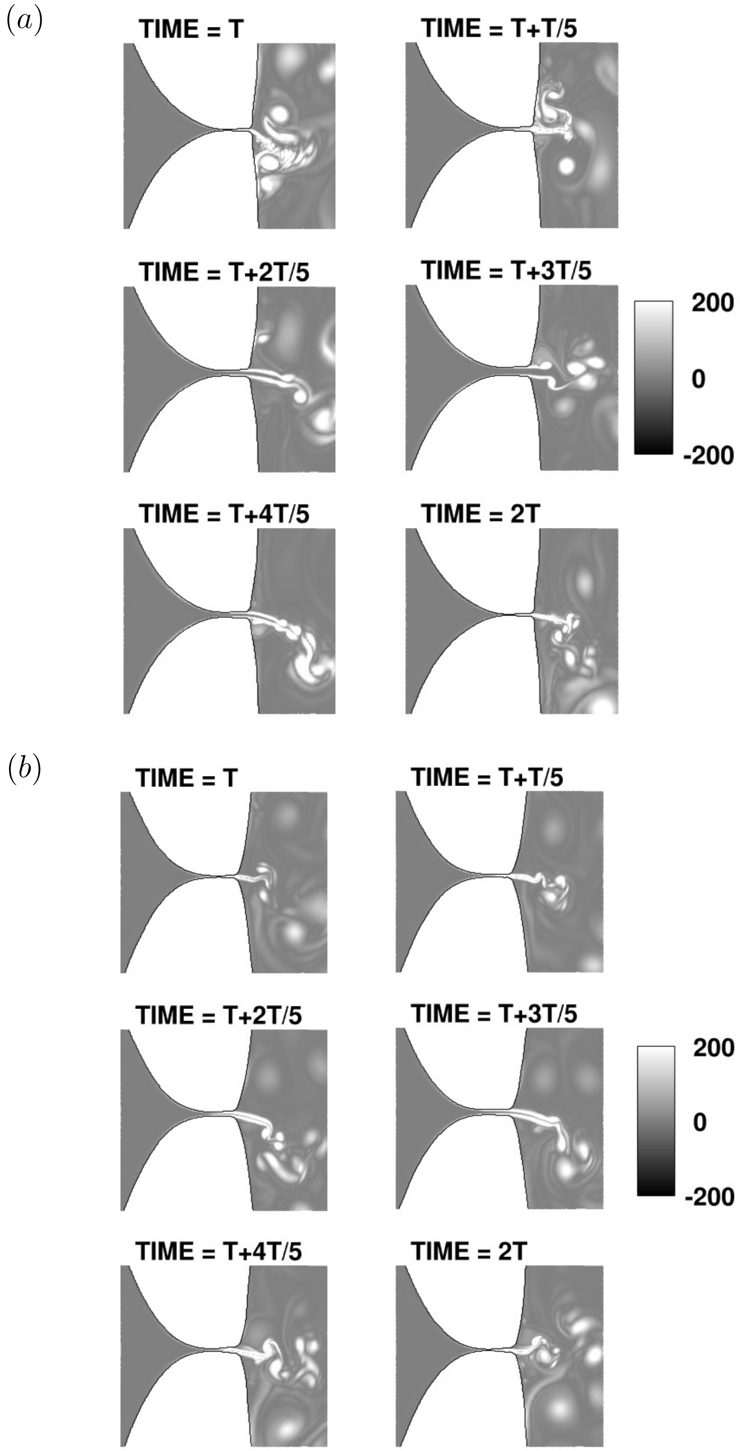

Figure 4.3: VF dynamics and vorticity contours for one full cycle for the human adult full body simulation (a) ν =0.27 and (b) ν =0.47.

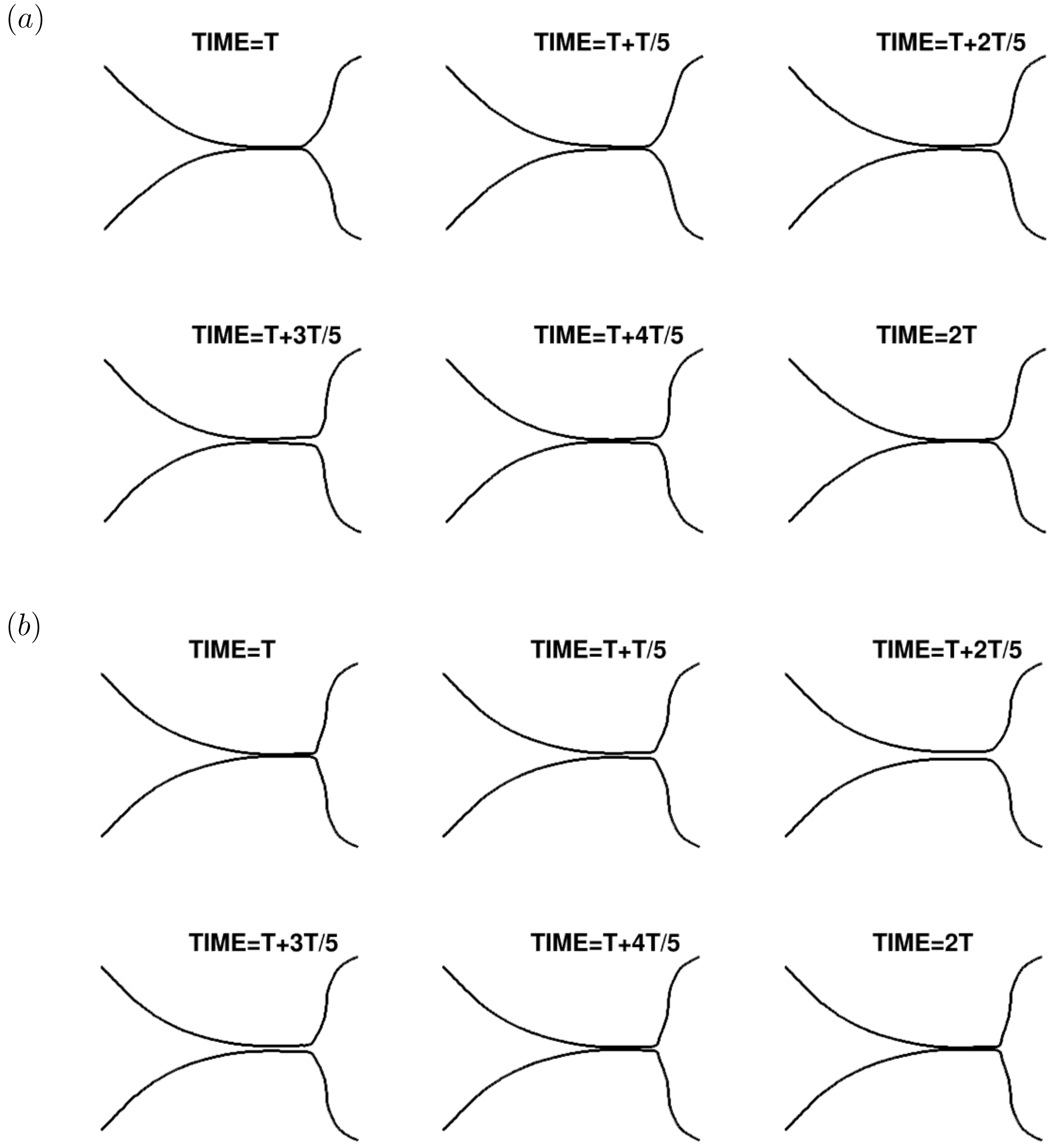

Figure 4.4: VF motion for one full cycle for the human adult full body simulation (a) ν =0.27 and (b) ν =0.47.

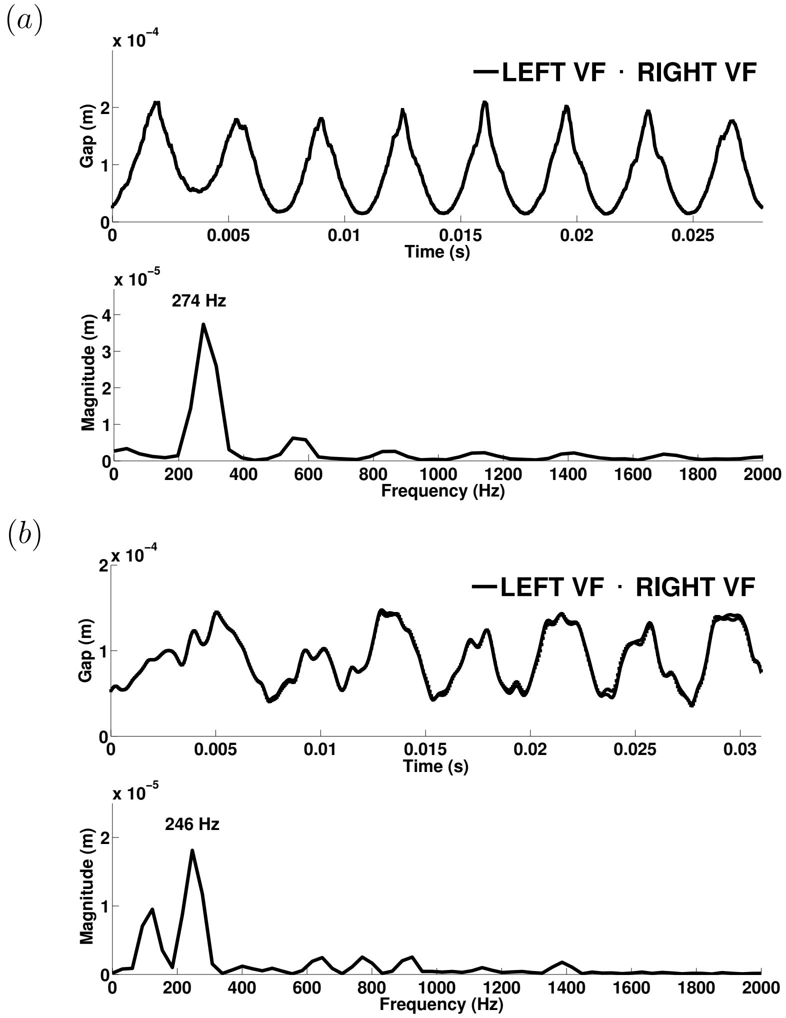

Figure 4.5: Minimum gap from centerline (top) and its FFT (bottom) for adult simulation with (a) ν =0.27 and (b) ν =0.47.

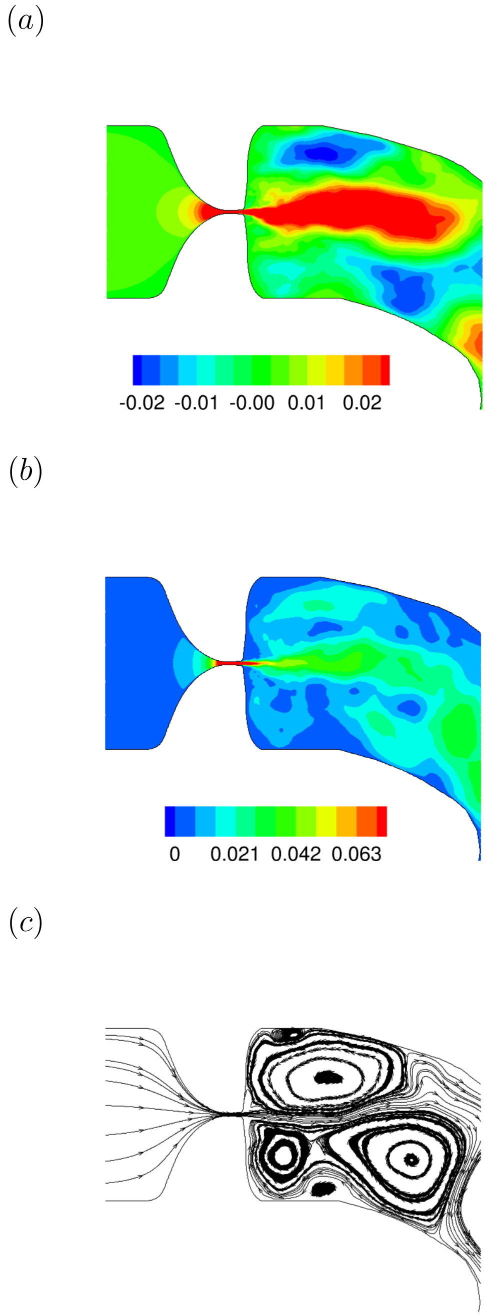

Figure 4.6: Time-averaged flow quantities for adult simulation with ν =0.27 showing (a) contours of non-dimensional stream wise velocity (b) contours of velocity magnitude and (c) streamlines.

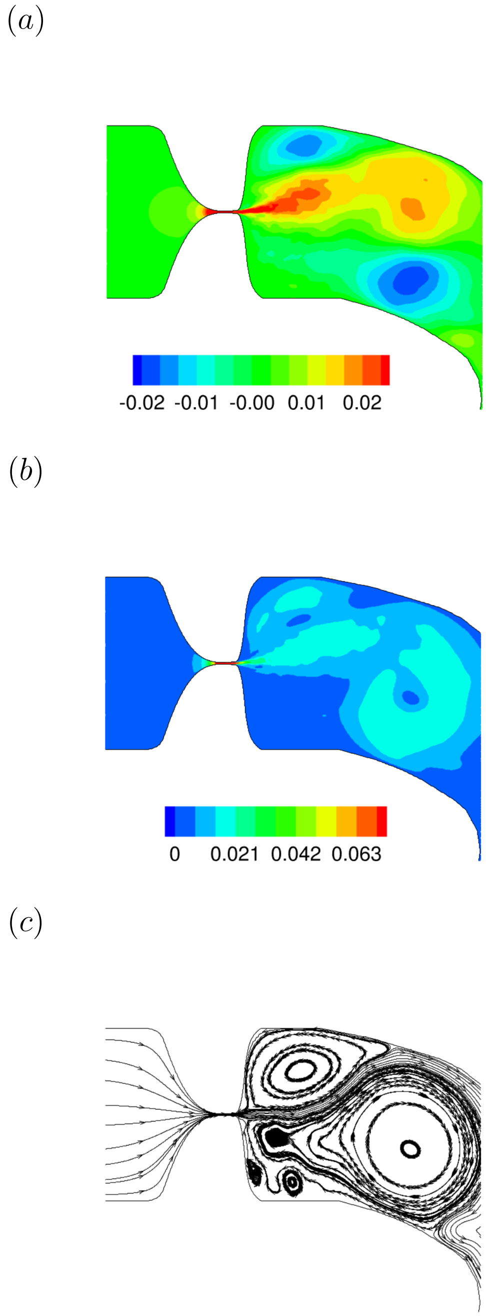

Figure 4.7: Time-averaged flow quantities for adult simulation with ν =0.47 showing (a) contours of non-dimensional stream wise velocity (b) contours of velocity magnitude and (c) streamlines.

supraglottal flow and the geometric changes in the vocal tract past the glottis. Similar observations have been reported in another study [71] but with a rectangular vocal tract. The asymmetry in that study was not as strong as in the present case which is due to the effect of the shape of vocal tract considered. The level of supraglottal flow asymmetry, which is an important aspect in the generation of sound, are significantly different with the current vocal tract when compared to the rectangular vocal tract case. It is pointed to the reader that the left and right VFs in the full body upright position as shown in Figure 4.1 are equivalent to the bottom and top VFs in the bottom-top configuration shown in Figure 4.7, and is obtained by suitable coordinate transformation.

Next we look at the time variation of the glottal flow which is an essential quantity in providing necessary information about the acoustic characteristics of the resulting flow in the far-field [75, 107, 159]. Several quantities can be obtained from the glottal waveform and compared to data from literature. Figure. 4.8(a) shows a typical glottal waveform [75]. The first quantities of interest include mean and maximum flow rate given by Q_{mean} and Q_{max} respectively. Typical values of Q_{mean} measured in experiments ranges from 0.11 cm^2/ms to 0.22 cm^2/ms [158] while the peak flow rate is observed to lie between 0.2 cm^2/ms to 0.58 cm^2/ms [160].

As pointed out in several phonation studies [75, 159, 161] that the time-varying glottal waveform acts as a representation of sound source according to the source-filter theory and quantities like open quotient (τ_0) and skewness quotient (τ_s) play a major role in determining sound quality. As such we calculate these quantities from the current simulation and relate it to those reported in literature. From Figure 4.8(a) the vibration period is defined as T, T_p is time of increasing flow, T_n is time of decreasing flow, and T_0 is the duration of flow. The open quotient (τ_0) is defined as the ratio of the flow duration to vibration period or $\tau_0 = T_0/T$. The skewness quotient is defined as the ratio of duration of increasing flow to duration of decreasing flow or $\tau_s = T_p/T_n$. Typical values of τ_0 ranges from 0.4 to 0.75 [5]. Values of τ_0 greater than 0.75 represents breathy voice while values lower than 0.4 indicates pressed voice [5, 75]. The skewness quotient is an indication of the the amount of inertia of the air column and VF collapse which results in a delay in flow buildup. Typical values of τ_s range from 1.1 to 3.4 [10, 71, 75, 162]. Another quantity of interest is the maximum flow declination rate or MFDR which is the instant of the most negative peak during a glottal flow cycle. Due to the flow rate skewness to the right (indicated by $\tau_s > 1$), the negative peak of the time derivative of the glottal flow in the closing phase is often much more dominant than the positive peak in the opening phase. MFDR is shown to be highly correlated to vocal intensity or peak amplitude of the produced voice [23, 159, 163], and as such will be considered when we discuss the far-field acoustics. A clinical study [164] has provided age and gender based correlation of MFDR to the sound pressure level and have highlighted the importance of this dependence as a measure of vocal intensity variation. Typical values of MFDR ranges from 0.1 cm^2/ms^2 to 0.45 cm^2/ms^2 [23, 159, 163].

Table 4.3 lists these quantities obtained for the two Poisson's ratio cases. Clearly these are within experimental and numerical limits as presented above. It is also noted that ν =0.27 case has higher overall flow rates as compared to ν =0.47 case. This is in accordance with the vocal fold deformation variation with time as shown in Figure 4.5 where larger displacements were observed for the lower Poisson's ratio case. All the quantities listed in Table 4.3 decrease with increasing Poisson's ratio. The same trend has been observed in the Poisson's ratio parametric study [93] done by varying Poisson's ratio from 0.4 to 0.499.

Table 4.3: Fluid flow parameters obtained from glottal waveform for the two Poisson's ratio cases.

Quantity	ν =0.27	ν =0.47
Q_{mean} (cm^2/ms)	0.167	0.151
Q_{max} (cm^2/ms)	0.31	0.24
τ_0	0.71	0.68
τ_s	1.51	1.23

Another quantity which has received substantial attention by researchers is the estimation of glottal flow separation location and it's behavior along the duration of any given VF oscillation cycle [10, 24, 29, 68]. Based on these studies it was observed that separation inside the glottis happens primarily during the closing phase of the oscillation cycle wherein the VFs present a divergent shape, while the opening phase (with convergent glottis) experiences minimum to no separation. It was also noted that the separation location

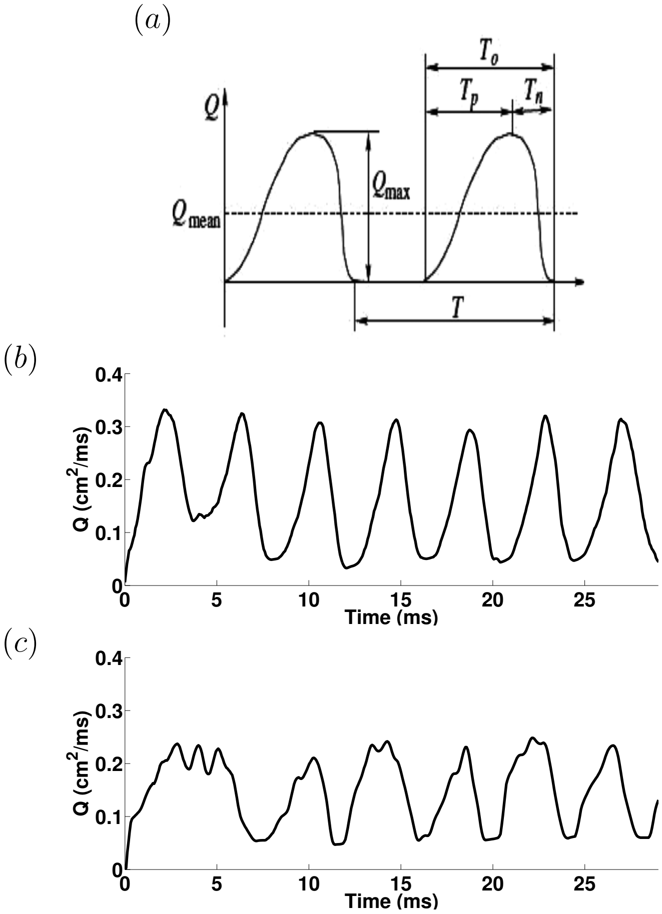

Figure 4.8: (a) Typical glottal flow rate waveform denoting the various flow quantities and (b) time variation of glottal flow rate for the ν =0.27 simulation and (c) time variation of glottal flow rate for the ν =0.47 simulation.

first moved upstream during the closing phase and this motion is inverted during the last part of the closing phase [29, 68]. However, these results are based on a single VF model or half-glottis model assuming flow symmetry across the glottal centerline [10, 29, 68]. As such, the effect of the presence of both VFs and their impact on flow separation locations of self and the other VF is missing and is crucial to understand. The accurate prediction of the flow separation point is important for phonation since it determines not only the volume flow velocity itself but also the hydrodynamical forces exerted on the vocal folds tissues.

Figure 4.9 provides a schematic of the separation point location determination. We employ a non-dimensional scaling denoted by s to obtain the separation location. Here $s = 0$ is a location chosen adequately upstream (based on the overall flow visualization), while $s = 1$ represents glottal exit and is marked by a sudden geometrical change in slope. It is noted that this location was again chosen based on flow visualization and is the point of maximum separation location. No separation was seen to occur beyond this location. The point of separation thus lies between these two points and it can be obtained as a non-dimensional value between 0 and 1. The separation location was identified as the point where the wall shear stress goes to zero or equivalently the wall normal derivative of the velocity is zero ($\frac{du}{dy}|_w = 0$). The instants when no separation occurred, the separation location was forced to a value of 1 ($s = 1$). The same procedure was applied to the other VF.

Figure 4.10 shows the time variation of the non-dimensional separation location (s) and the minimum VF gap from centerline plots for the two VFs for the two Poisson's ratio cases. The first thing that is clearly noted from both the Poisson's ratio cases is that separation happens during the glottal closure phase as was also observed in past studies [10, 24, 29, 68]. The opening phase experience no separation. The other important observation related to the interaction of the VFs is that during each cycle, it is primarily only one VF where separation is noted while separation on the other VF is pushed to glottal exit (which sets non-dimensional separation location or s equal to 1). This phenomena can be explained by looking at Figure 4.11 where for both the Poisson's ratio cases, separation from one VF within the glottis suppresses the point of detachment on the other, ultimately pushing it to glottal exit. The only exception to this is the very small duration (during the fifth cycle) for the Poisson's ratio of 0.47 where separation is seen to

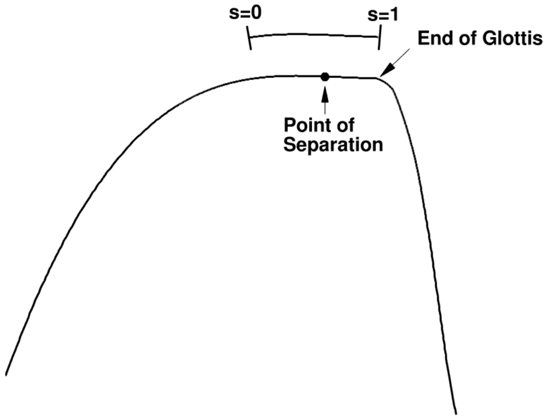

Figure 4.9: Sketch showing the non-dimensional scaling used for separation point determination.

happen on both the VFs. This interaction of the glottal flow separation is particularly important since it emphasizes the utility of considering both VFs for simulation and that this important dynamics is lost with the assumption of a symmetrical glottis [10,29,68]. The next point of observation is that the separation location first moves upstream and then this motion is inverted which is in accordance with past studies [29,68]. It is also noted that the non-uniformity in the VF deformation as seen from the VF gap from centerline plots for the Poisson's ratio 0.47 case, also affects the separation location in a similar manner. This non-uniformity in VF deformation which is due to the mucosal wave generation for the higher Poisson's ratio case in turn exhibits itself in the separation location plot, highlighting the inter-dependence of the fluid-structure interaction. Poisson's ratio of 0.27 case with predominant lateral VF motion and an absence of surface mucosal wave shows a much smoother variation for the two quantities plotted in Figure 4.10(a).

The two major parameters that are significant for voice quality are loudness and pitch. The former is characterized by the sound pressure level (OASPL) and the latter by the frequency content of the acoustic field. Figure 4.12 shows the oscillatory behavior of the acoustic waves (dilatation) exiting the mouth which are induced as a result of the VF motion and the interaction of the glottal jet with the vocal tract walls. This data can be

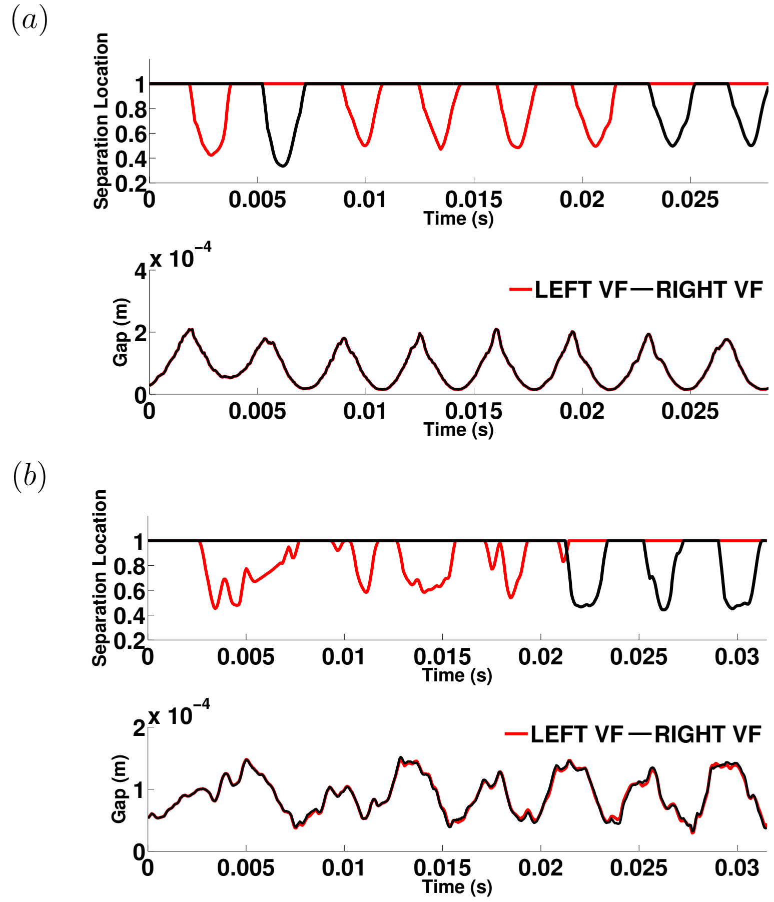

Figure 4.10: Time variation of non-dimensional separation location (top) and VF minimum gap for centerline for adult simulation with (a) ν =0.27 and (b) ν =0.47.

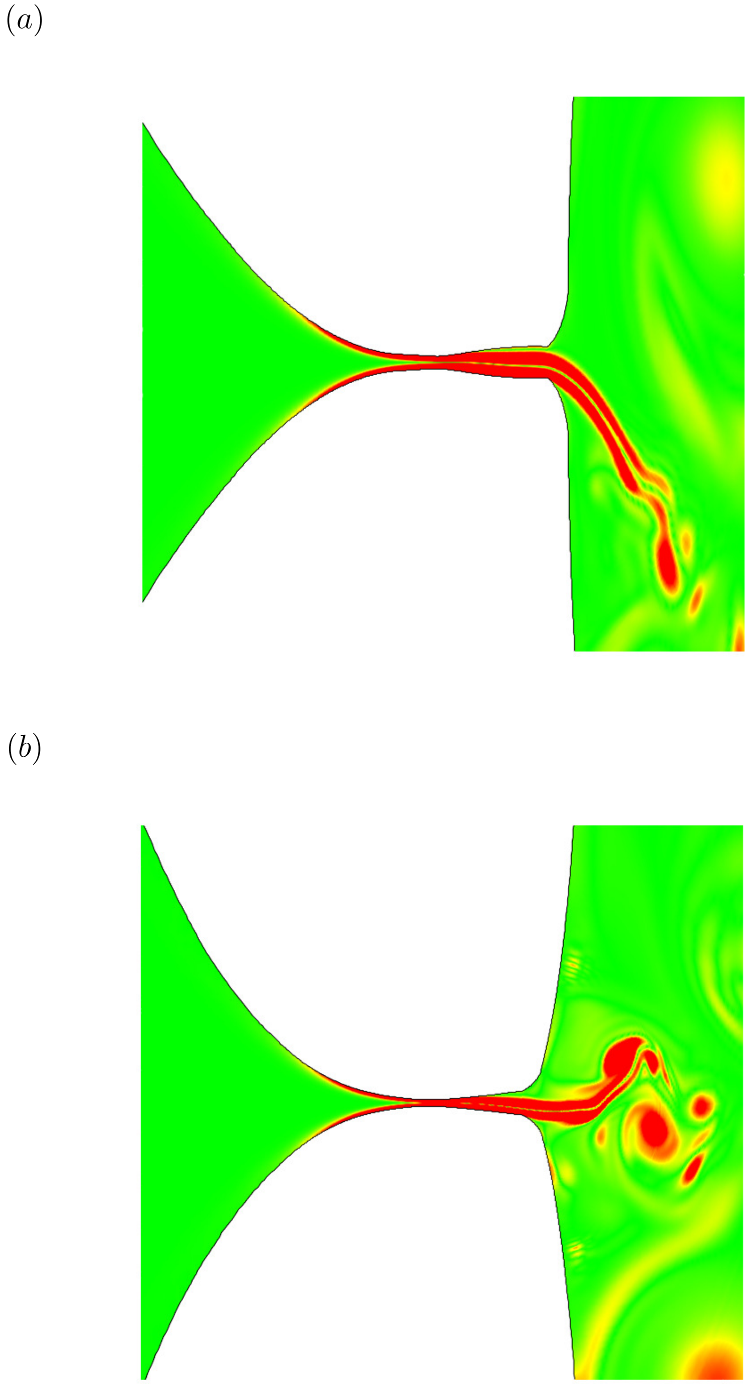

Figure 4.11: Instantaneous contour of vorticity showing separation on the two VFs for adult simulation with (a) ν =0.27 and (b) ν =0.47.

used to study acoustic characteristics of the flow which is computed directly without resorting to an acoustic analogy.

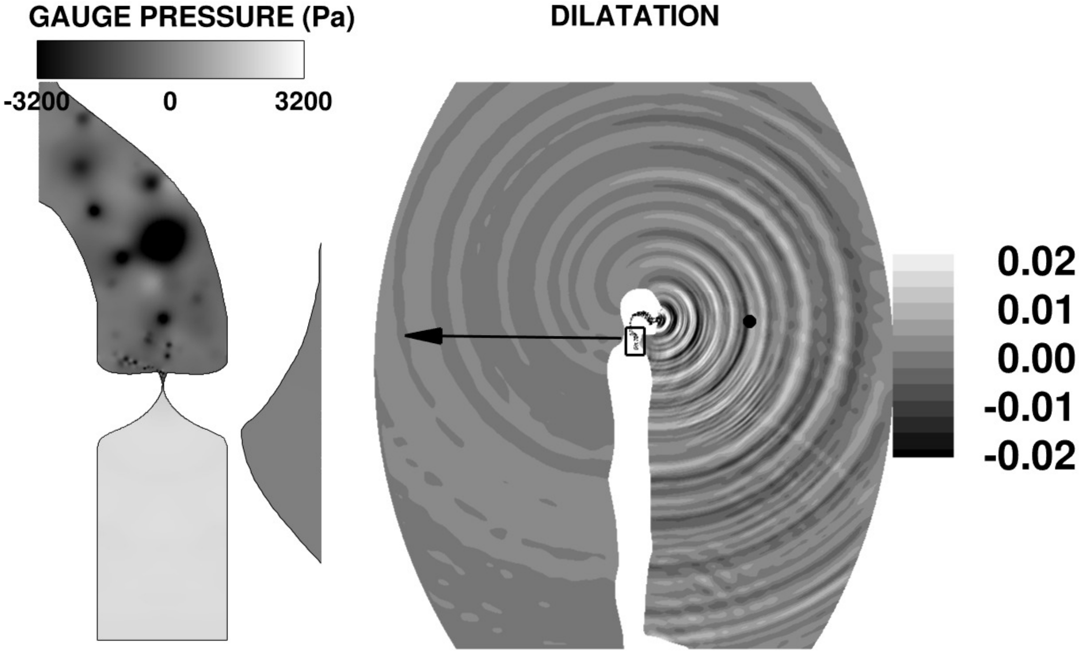

Figure 4.12: Gauge pressure (left) and far-field dilatation ($\nabla.\boldsymbol{u}$) field (right) for the human adult full body simulation.

In order to obtain pressure fluctuations due to compressibility effects, we use the linearized energy equation given by:

$$\frac{\partial p'}{\partial t} + \gamma P_{\infty} \nabla \cdot \boldsymbol{u'} = 0 \tag{4.4}$$

To obtain p' at any given point in the far field, we calculate the mean of $\boldsymbol{u}$ over time and then subtract this value from the instantaneous value to get $\boldsymbol{u'}$. Once this is done we solve Eq. (4.4) using numerical integration (Trapezoidal method) to get p'. In order to verify if the numerical integration is accurate enough, we compare it with the exact solution for the linearized energy equation in one dimension, for a right going wave $u'(x,t) = \frac{1}{c} sin(x - \bar{c}t)$. The exact solution is given by:

$$p'_{exact} = \bar{\rho}\bar{c}u' \tag{4.5}$$

Figure 4.13 gives the comparison. The estimated maximum error was found to be 0.4%.

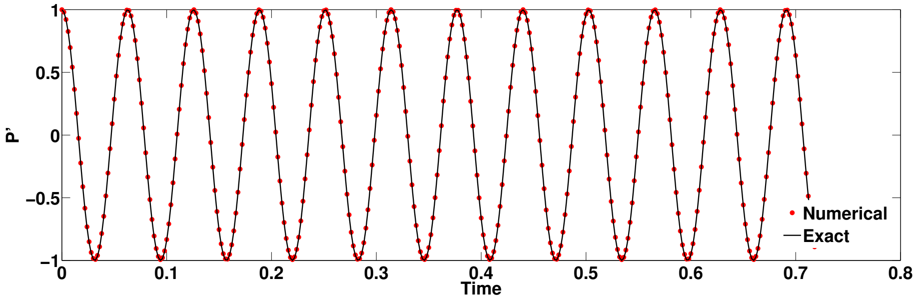

Figure 4.13: Validation of numerically obtained pressure fluctuation obtained using the linearized energy equation against exact solution for one-dimensional right going wave.

We would like to mention that in this calculation we have eliminated the contribution from the waves reflected from the foot of the speaker (see Appendix C for details), by calculating the center of the reflected waves (under cylindrical wave assumption), and using this and the center of the speaker's mouth exit, by simple geometry and knowing the velocity components of the entire field at any point, the wave velocity component emitted by the speaker's mouth can be extracted. This velocity can be plugged in Eq. (4.5) to obtain p' corresponding to only the emitted wave field. Once we have the variation of p' with time, we can obtain the sound pressure level $OASPL$ using the formula,

$$OASPL = 10\log_{10}\left(\frac{P_{\text{rms}}^2}{P_{\text{ref}}^2}\right). \tag{4.6}$$

The pitch characteristic is studied via the frequency spectrum at a point in the far-field. Figure 4.14 shows a signal of pressure fluctuations at a far-field point outside the speaker's mouth and a fast-fourier transform (FFT) of this data. The higher Poisson's ratio case shows reduced pressure fluctuation amplitude and fundamental frequency than the lower Poisson's ratio case.

Figure. 4.12 shows that the dilatation field outside the speaker's mouth is approximately cylindrical. This prompts conducting a directivity analysis, to see the variation of a quantity like sound pressure level over changing angles. For this a circle centered at the speaker's mouth with a radius of around 2 ft was created, excluding the arc that intersect with the body. This

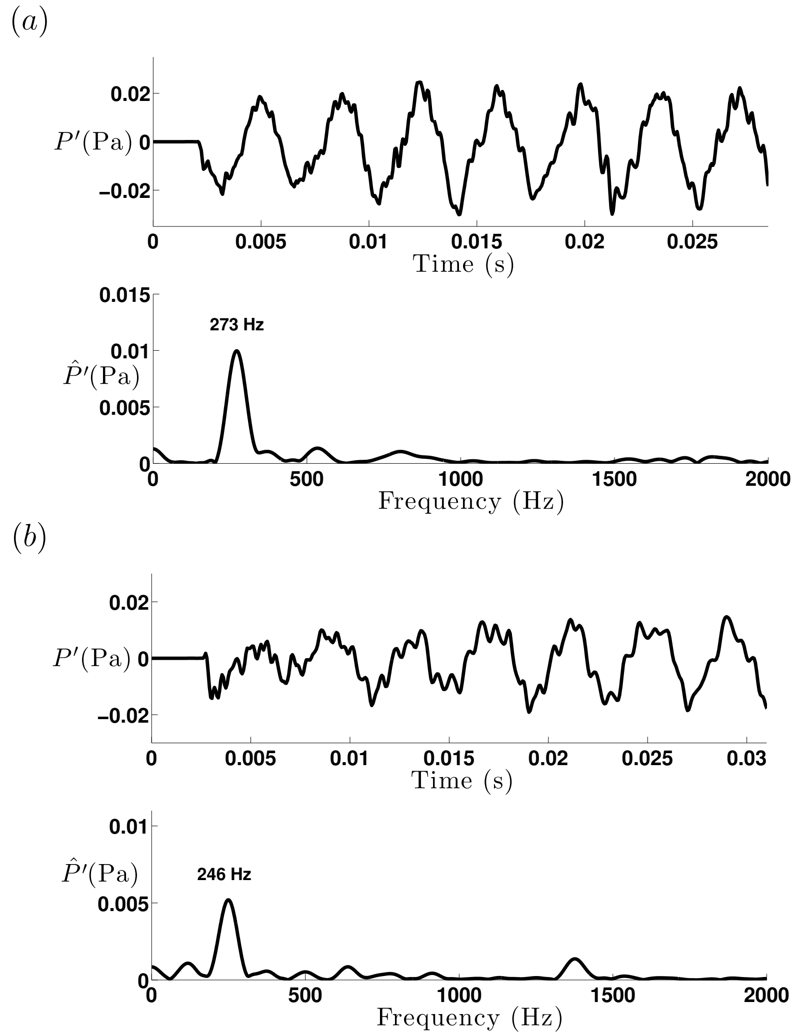

Figure 4.14: Far-field pressure fluctuation versus time for the human adult simulation at a location directly facing the speaker's mouth for (a) $\nu = 0.27$ and (b) $\nu = 0.47$.

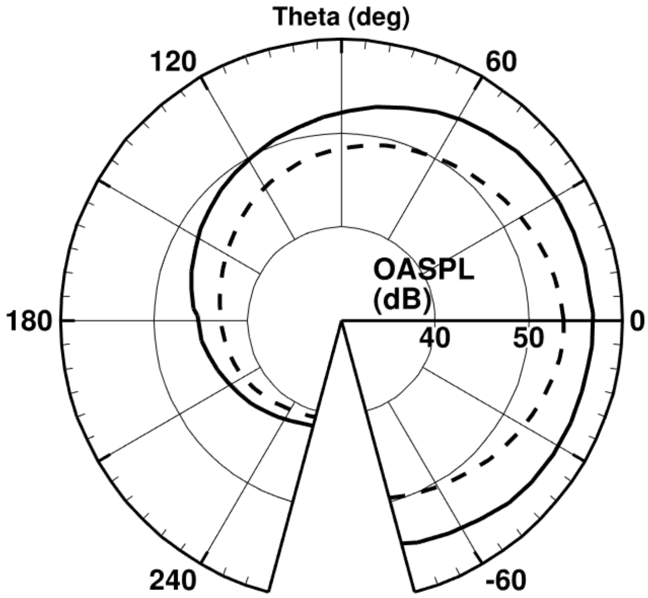

Figure 4.15: Overall sound pressure level directivity plot on a circle centered at the speaker's mouth and a radius of 2 feet for the human adult full body simulation. Solid line represents ν =0.27 case while dashed line represents ν =0.47 case.

location was selected to avoid any possible hydrodynamic contamination to the acoustic field if measured close to mouth exit. Sound pressure levels are measured along equidistant points on this circle. Figure 4.15 shows this variation. The excluded arc can be seen in the form of the cut sector at the bottom of the plot. As such, the angle $\theta = 0$ corresponds to a point directly in front of the mouth. For both the Poisson's ratio cases, it is observed that in the first and the fourth quadrant, corresponding to the part of the domain facing the mouth, the sound pressure levels are higher as compared to the third and fourth quadrant representing the back. Moreover, a gradual decrease in the sound pressure level values is noticed as one moves away from $\theta = 0$ position, indicating that the waves are stronger along the $\theta = 0$ line, and its intensity decreases with deviation from this angle. The sound field radiation to the back of the body is quieter due to wave diffraction around the head. However, the OASPL for the higher Poisson's ratio cases is lower along the entire circle as compared to the lower Poisson's ratio case. The maximum difference between the two cases is approximately 3.5 dB.

As was pointed earlier, the MFDR value based on the glottal flow waveform, has a direct correlation to the vocal intensity of the sound produced which will in turn directly affect the far-field sound levels. Table 4.4 provides the value of MFDR obtained from the glottal flow waveform in Figure 4.8 and the OASPL (measured at a point 2 ft from the speaker's mouth) for the two Poisson's ratio cases. The MFDR values lie within phonation limits mentioned earlier. As the Poisson's ratio is increased from 0.27 to 0.47, the MFDR and the OASPL values increases. Thus for a Poisson's ratio of 0.27 where a higher MFDR was obtained, the resulting OASPL value increased too. Theoretical [159, 163] and clinical [23] studies have established this dependence as well.

Table 4.4: MFDR and OASPL (measured at a point 2 ft from the speaker's mouth) for the two Poisson's ratio cases for the adult simulation.

Quantity	ν =0.27	ν =0.47
MFDR (cm^2/ms^2)	0.35	0.19
OASPL	57	53.5

4.3 Full body Simulation of Human Child

Age related differentiation of phonation characteristics has received very limited attention from the simulation community. As such an analysis based on this aspect becomes imperative.

As has been described in Sec. 4.2, a fully developed adult VF is comprised of three differentiable layers: the thin outer cover, the inner body and a transition layer in between the two. In a child, the transition layer and the cover are not fully developed. Instead, one uniform layer exists with properties similar to the cover layer of an adult [165].

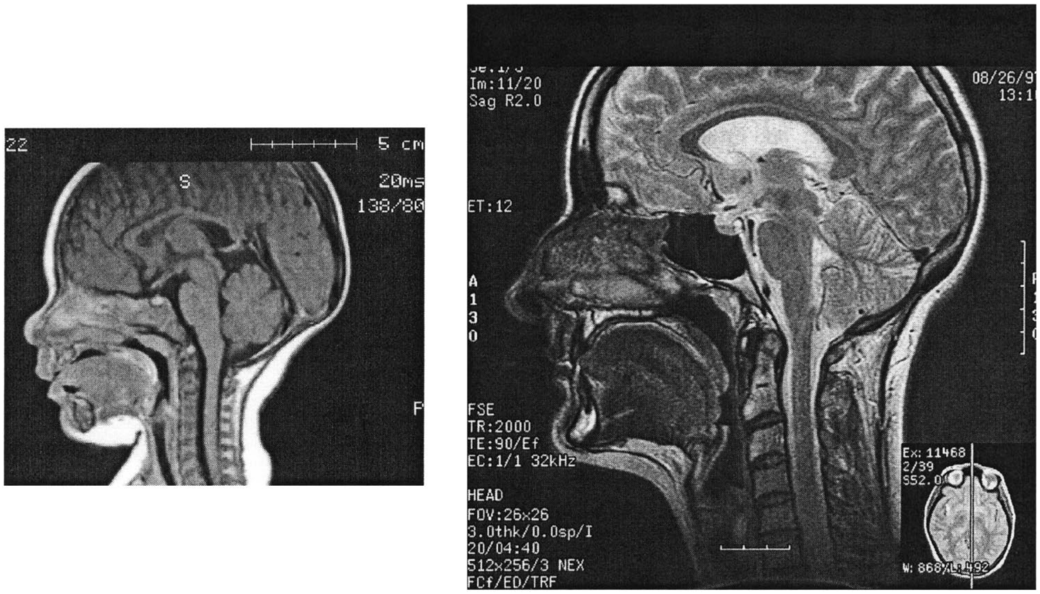

Figure 4.16: MRI images of human child and adult showing key vocal tract characteristics [Source: Vorperian et. al. (2005)].

The vocal tract experiences significant changes with age [166], as shown in Figure 4.16. First, the length of the vocal tract increases with age. Figure 4.17 shows the variation of the vocal tract length with age from a statistical study [166]. Another change that is significant is the laryngeal descent [166] with age as shown in Figure 4.18. Other changes include increase of pharyngeal length with age and development of curvatures along the vocal tract past the VFs. Most structures, despite differences in growth rate, appear to follow a growth pattern or a growth curve that is similar to that of the vocal tract length.

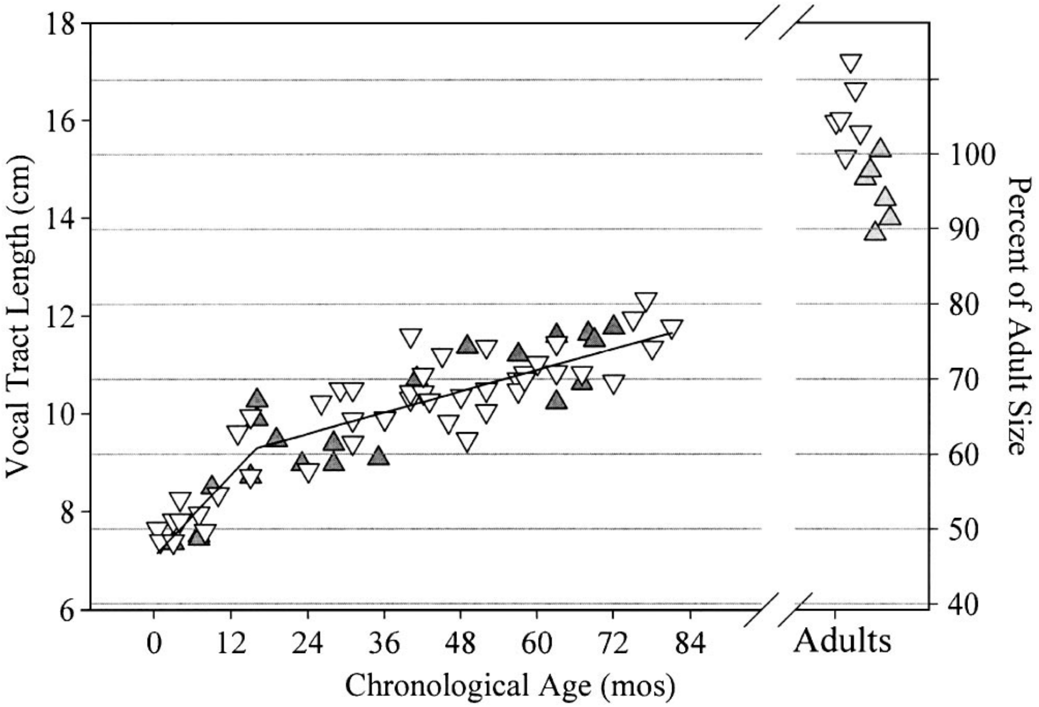

Figure 4.17: Vocal tract length with age [Source: Vorperian et. al. (2005)].

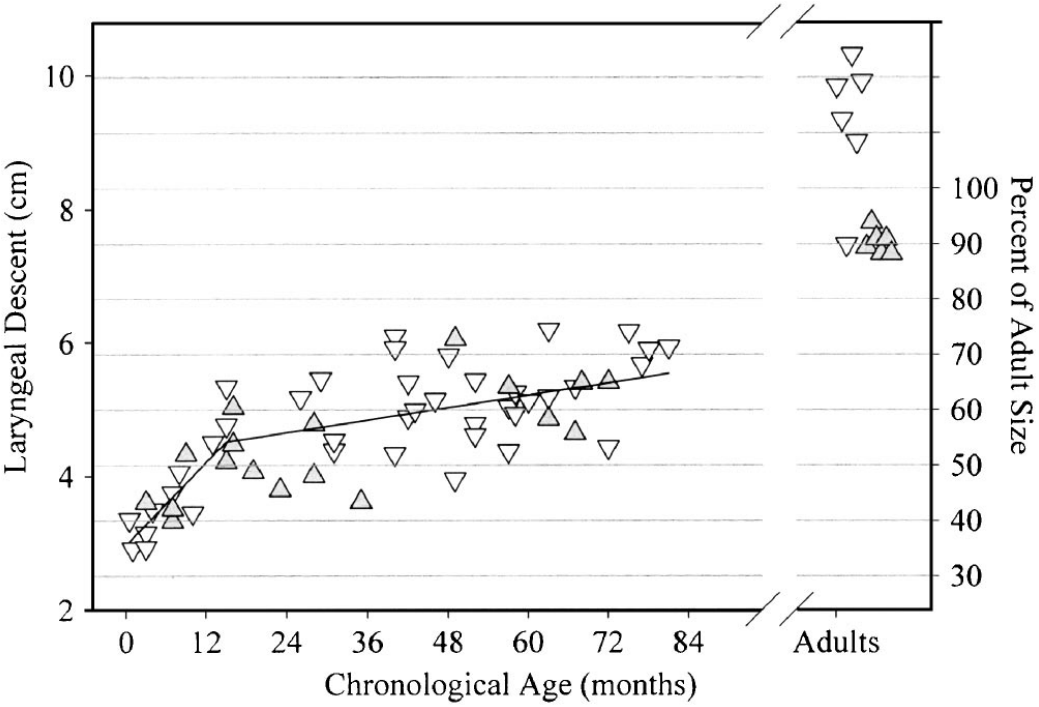

Figure 4.18: Laryngeal descent with age [Source: Vorperian et. al. (2005)].

Based on the above clinical data, we created a two year old child model for our simulation. A two year child model was selected since it encompasses all the above mentioned geometrical and biomechanical features and has been studied in detail in literature [94,97]. The VFs for the child was a two layered model with the first layer combining the top two layers, while the body layer remaining the same. Table 4.5 shows the modification we did to the already existing three-layered model to achieve the desired goal. We then modified the shape and the size of the vocal tract according to the above observations for a 2 year old. We also shifted the larynx upwards by 6 cm to account for the laryngeal descent that we see with age. These modifications are explained in Figure 4.19.

Table 4.5: VF material properties of a child.

Layer	Young's modulus (kPa)	Poisson ratio
Cover	25	0.27, 0.47
Ligament	25	0.27, 0.47
Body	50	0.27, 0.47
Cartilage	250	-

The simulation used the same initial and boundary conditions as those used for the adult configuration. Grid resolution was maintained same as the human adult full body case.

Figure 4.20 shows the vorticity ($\boldsymbol{\omega} = \nabla \times \boldsymbol{u}$) contours and Figure 4.21 shows the corresponding VF motions for one full cycle for the two Poisson's ratio cases. Again, as in the adult case for the Poisson's ratio close to incompressibility limit, the presence of the mucosal wave with clear convergent-divergent VF shapes during the opening and closing phase of the VF motion is noted while the lower Poisson's ratio case is dominated by lateral motion of the VFs. The amplitude of VF oscillation is clearly higher for the lower Poisson's ratio case as was observed in the adult simulation.

Figure 4.22 shows minimum VF gap from centerline for the two Poisson's ratio cases. As observed qualitatively in Figure 4.20, the VF amplitude of motion is greater for the lower Poisson's ratio case. The dominant frequency of oscillation indicated by the peak in the FFT plot, is also an inverse function of the Poisson's ratio again complying to the observations of Shurtz and Thomson [93]. The fundamental frequency values are also in accordance

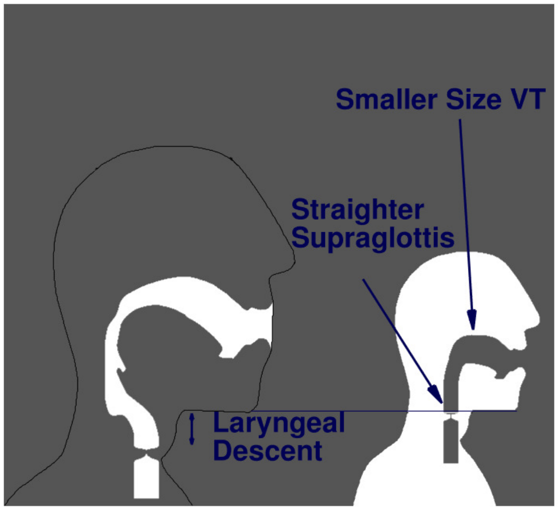

Figure 4.19: Adult versus child vocal tract model showing differences that were applied to the fluid domain.

with prior clinical and theoretical results for a two year old child [94, 97].

In the far-field as shown in Figure 4.23, the higher Poisson's ratio case shows reduced pressure fluctuation amplitude and fundamental frequency than the lower Poisson's ratio case as was observed in the adult simulation and in accordance with the VF oscillation amplitude in Figure 4.22. Moreover the pitch content of the far-field acoustics is richer for the child case when compared to adult with fundamental frequency almost 1.4 times that of an adult. This is consistent with what is observed naturally as well. The OASPL directivity plot shown in Figure 4.24 follows the behavior obtained for the adult case, with the higher Poisson's ratio cases having a lower acoustic intensity along the entire circle as compared to the lower Poisson's ratio case. The maximum difference between the two cases is approximately 3 dB.

As was shown for the adult case, the MFDR value based on the glottal flow waveform, had a direct dependence on the OASPL values measured in the far-field. We provide these values for the current child simulation case in Table 4.6. The MFDR values lie within phonation limits mentioned earlier. As the Poisson's ratio is increased from 0.27 to 0.47, the MFDR and the OASPL values increases. Thus for a Poisson's ratio of 0.27 where a higher

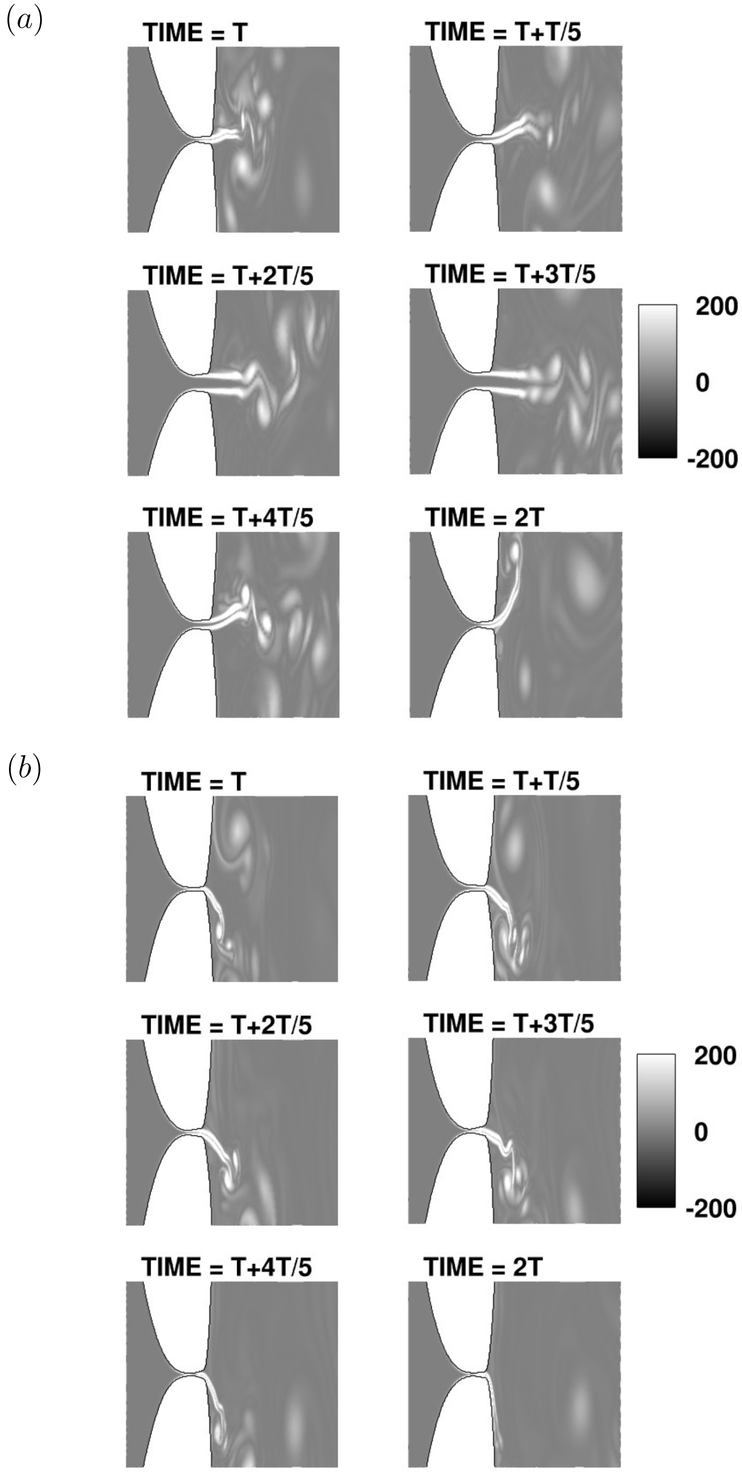

Figure 4.20: VF dynamics and vorticity contours for one full cycle for the human child full body simulation (a) $\nu = 0.27$ and (b) $\nu = 0.47$.

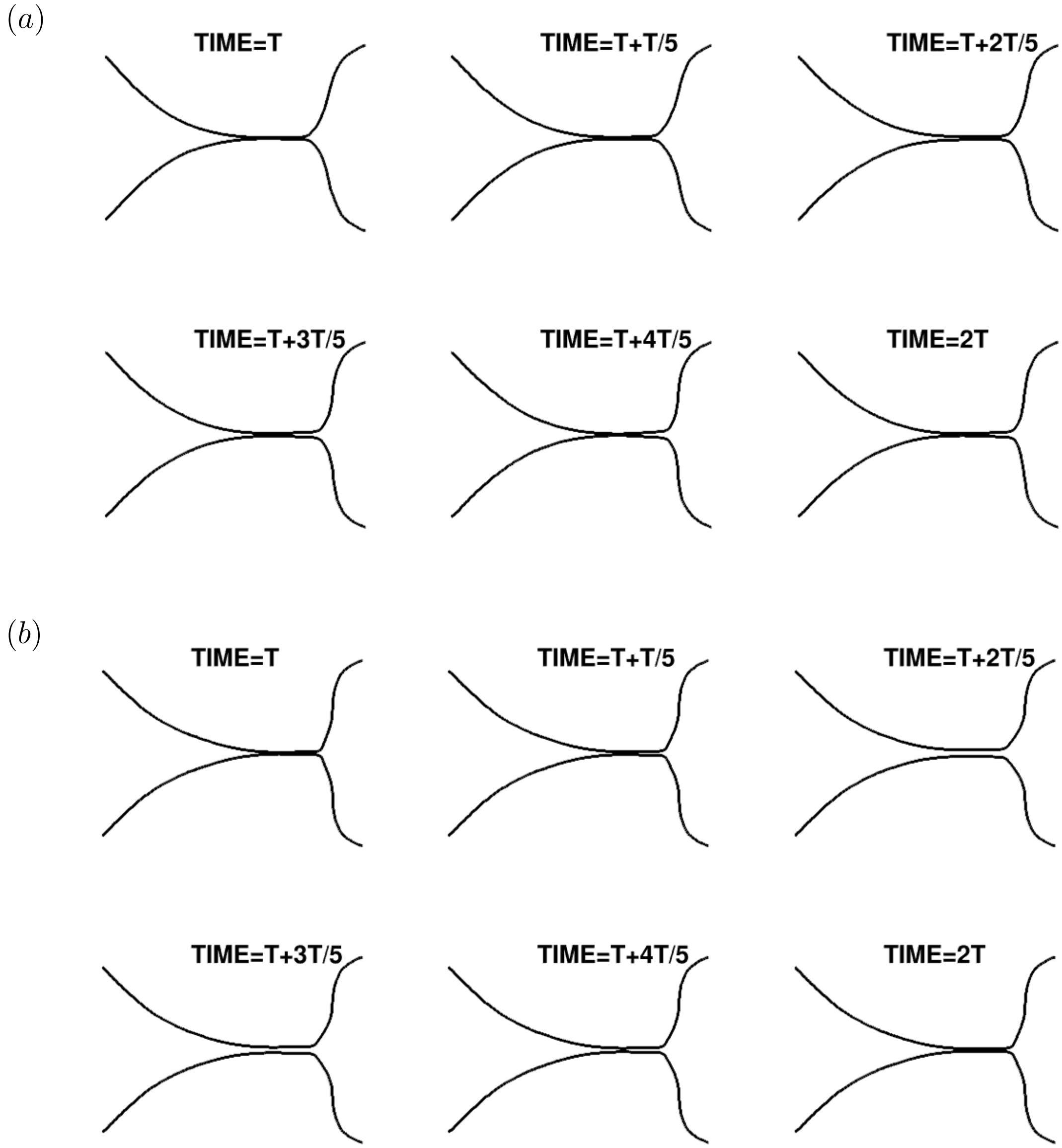

Figure 4.21: VF motion for one full cycle for the human child full body simulation (a) $\nu = 0.27$ and (b) $\nu = 0.47$.

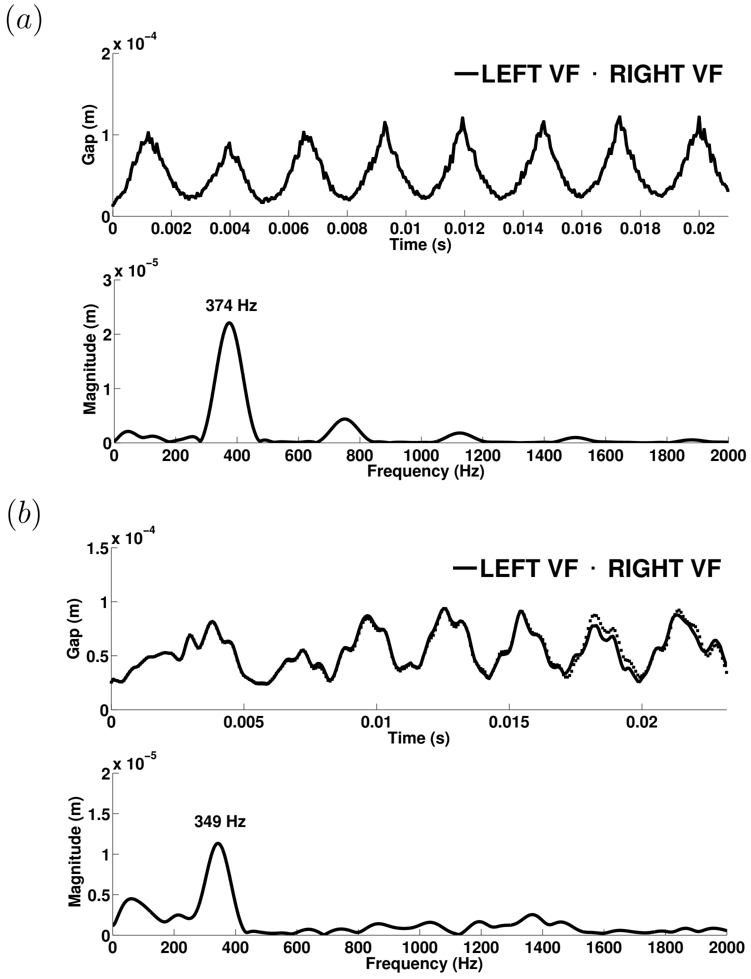

Figure 4.22: Minimum gap from centerline (top) and its FFT (bottom) for the child simulation with (a) $\nu = 0.27$ and (b) $\nu = 0.47$.

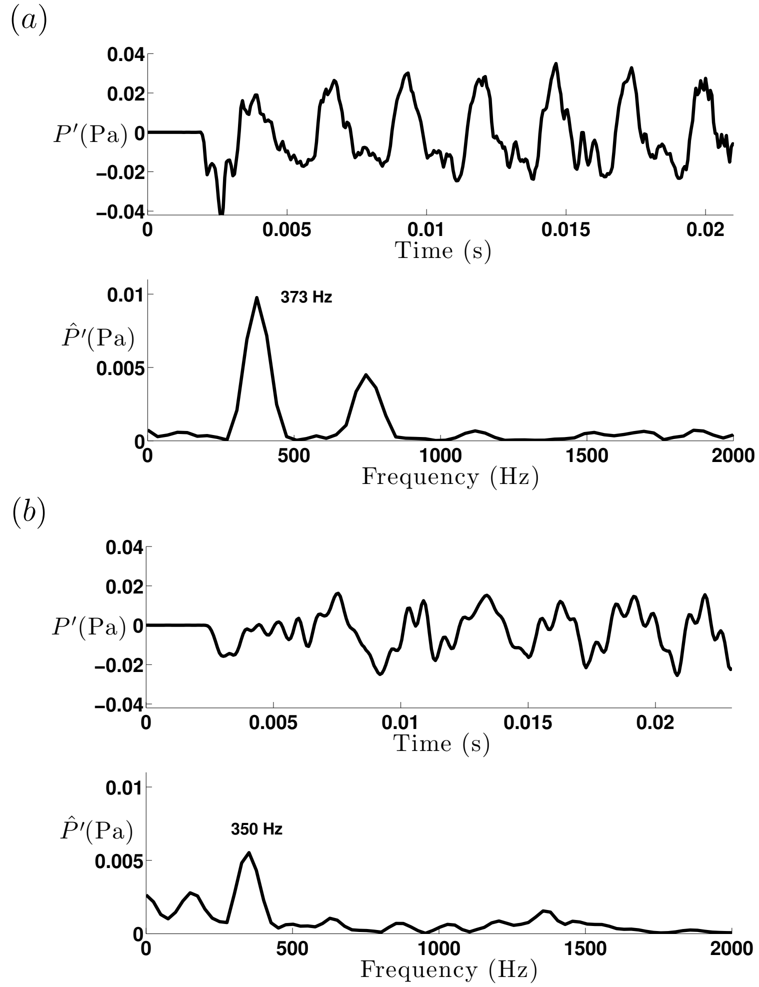

Figure 4.23: Far-field pressure fluctuation versus time for the human child simulation at a location directly facing the speaker's mouth for (a) $\nu = 0.27$ and (b) $\nu = 0.47$.

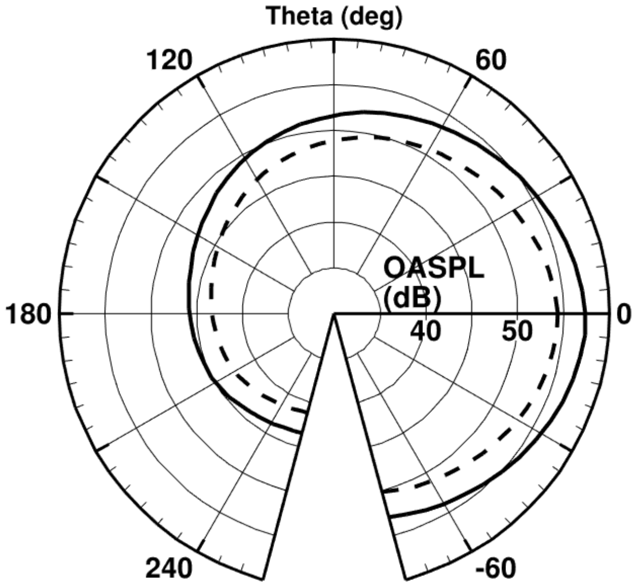

Figure 4.24: Overall sound pressure level directivity plot on a circle centered at the speaker's mouth and a radius of 2 feet for the human child full body simulation. Solid line represents $\nu = 0.27$ case while dashed line represents $\nu = 0.47$ case.

MFDR was obtained, the resulting OASPL value increased too which was also seen for the adult simulation case.

Table 4.6: MFDR and OASPL (measured at a point 2 ft from the speaker's mouth) for the two Poisson's ratio cases for the child simulation.

Quantity	ν =0.27	ν =0.47
MFDR (cm^2/ms^2)	0.23	0.13
OASPL	57.6	54.8

4.4 VF Material Property Sensitivity Study

Following the simulation of the adult and child phonation, the effect of changing the material properties of the VF layers on phonation characteristics like sound intensity and pitch was analyzed. The motivation for doing this parametric study was the high degree of variance present in literature with regards to the different stiffnesses for the three layers used in simulation studies. The elasticity of the cover layer varied from as much as 5 kPa [167] to 25 kPa [71, 168]. Larger variations were observed for the ligament layer with elastic modulii ranging from 6 kPa [167] to 104 kPa [71]. Body layer properties, on the other hand, did not show such a large variation from one study to another, ranging from 45 kPa [168] to 52 kPa [71]. Another aspect of conducting such an analysis is based on VF pathologies wherein damage to VFs due to fatigue (observed in singers and teachers) or due to trauma, is visible in the form of stiffness variation in the various layers of the VFs. As such, a sensitivity study with respect to elastic modulus of the VF layers, seems a reasonable way to go.

Three different cases for this analysis were undertaken. Table 4.7 provides the parameters for each of these cases and also comparing to the already completed adult simulation. The cover layer elasticity was varied by $\mp 20\%$ for the first two cases and the ligament layer was made considerably softer for the third case, while the other properties were kept unchanged. Varying one property at a time will give an insight on the effect of each of these variations independently. Both the Poisson's ratio (ν =0.27,0.47) were studied for the cases mentioned here. All other simulation parameters were unchanged from the adult case.

Table 4.7: VF Material Properties (in kPa) for 3 cases with perturbed properties.

Case	E_{Cover}	$E_{Ligament}$	E_{Body}
Adult	25	100	50
Case 1	20	100	50
Case 2	30	100	50
Case 3	25	10	50

The far-field characteristics were analyzed for this study. The pressure fluctuation are plotted for this study in Figure 4.25 and Figure 4.26 for Poisson's ratio 0.27 and 0.47 respectively. For case 1 with lower cover layer stiffness, both the Poisson's ratio cases presented lower pressure fluctuation amplitudes than the adult case while for case 2 with higher cover layer stiffness, the trend was opposite. Further for case 3 with significant reduction in ligament layer stiffness, the pressure fluctuations exhibited marked reduction from the adult case. The values of the fundamental frequencies F0, also shows significant variations from case to case. Our understanding points to observing higher frequencies when the VFs are stiffened and lower when they are made softer. When compared to the adult case, stiffening the VFs for case 2, increased the fundamental frequency while making it softer for case 1 and 3 decreased it. Table 4.8 also provides the OASPL obtained from the corresponding pressure fluctuations for the cases studied here. In Figure 4.27 we overlay the pressure fluctuation data for adult, case 1 and case 2 to understand the variation in phase with time by varying the VF stiffness. As is noted from the plots, for both the Poisson's ratio cases, the VF case with lower stiffness than the adult case results in a growing lag in phase as time progresses. This trend is opposite for the case with higher VF stiffness than the adult case. Thus the significant differences in far-field quantities indicate the relevance of change in VF stiffness on the calculated acoustic field.

Once again the effect of Poisson's ratio is also quite noticeable. For all the cases considered here, decreasing the Poisson's ratio from 0.47 to 0.27 led to an increase in the pressure fluctuation amplitude as well as the fundamental frequency. This is consistent with the observations from the adult and child simulations as well as the analysis done by Shurtz and Thomson [93].

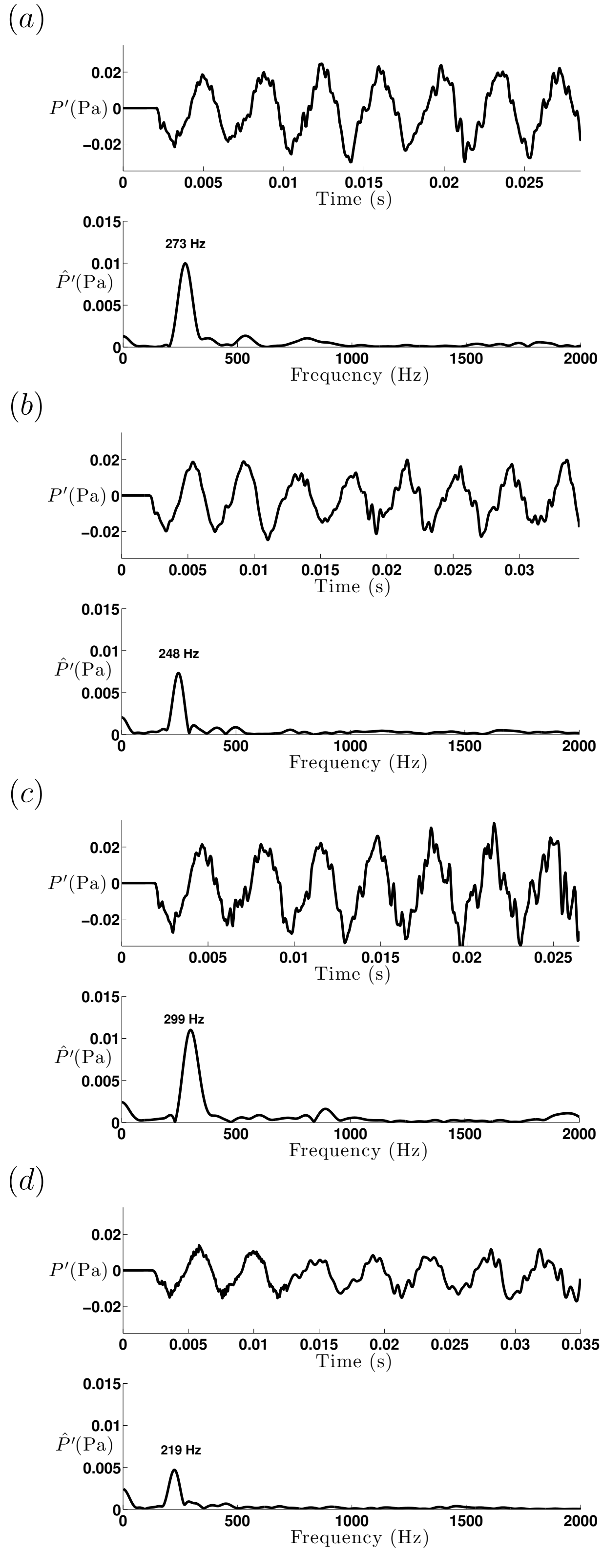

Figure 4.25: Far-field pressure fluctuation versus time for VF material property sensitivity study with ν =0.27 for (a) Adult, (b) Case 1, (c) Case 2 and (d) Case 3.

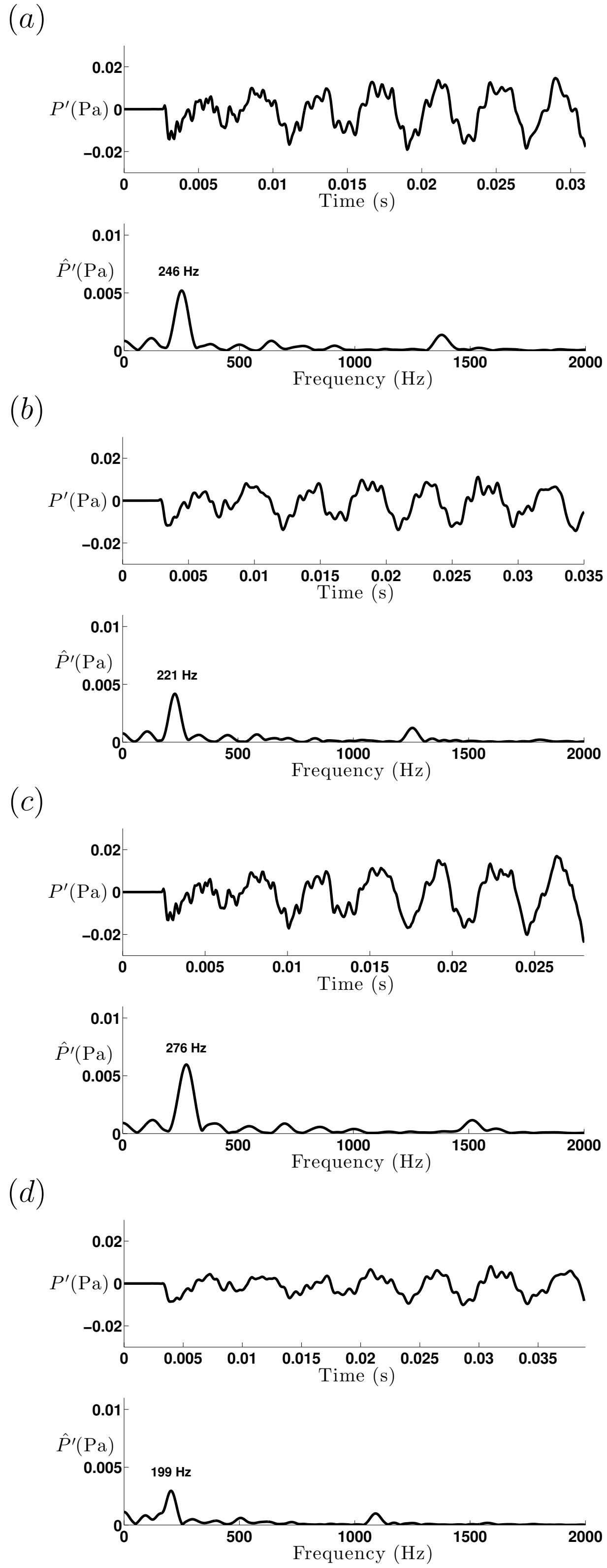

Figure 4.26: Far-field pressure fluctuation versus time for VF material property sensitivity study with ν =0.47 for (a) Adult, (b) Case 1, (c) Case 2 and (d) Case 3.

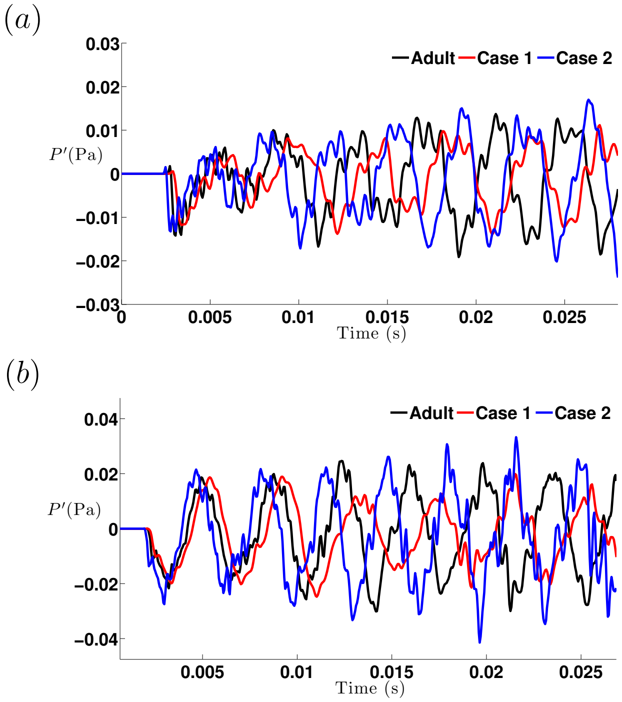

Figure 4.27: Far-field pressure fluctuation versus time for adult, case 1 and case 2 with (a) ν =0.47 and (b) ν =0.27.

Previous adult and child simulations showed that MFDR had a direct dependence on the OASPL values measured in the far-field. The current sensitivity study provides an opportunity to study this dependence. The MFDR values for the current simulation cases is presented in Table 4.9 and they lie within phonation limits mentioned earlier. When comparing these to the OASPL values in Table 4.8, the direct dependence between the two quantities is clearly verified. An increase in VF stiffness results in an increase in MFDR which in turn leads to an increase in OASPL and vice-versa.

Table 4.8: OASPL (in dB) for the sensitivity study.

Case	$\nu = 0.27$	$\nu = 0.47$
Adult	57	53.5
Case 1	53.5	50.6
Case 2	59.4	55.2
Case 3	52	49.5

Table 4.9: MFDR (in cm^2/ms^2) for the sensitivity study.

Case	$\nu = 0.27$	$\nu = 0.47$
Adult	0.35	0.19
Case 1	0.31	0.16
Case 2	0.40	0.22
Case 3	0.26	0.14

4.5 Non-Linear vs Linear Elasticity

Till now the focus was on using a non-linear finite deformation model of the VFs. In this section results are presented for the situation when the VFs are modeled using an infinitesimal strain assumption applied in a linear elastic constitutive model framework as also provided in Luo et al. [71]. The material properties of the VFs with respect to its stiffness in different layers and other simulation parameters are kept the same from the adult simulation case which has been also presented here for comparison. Poisson's ratio of 0.47 is used based on our understanding so far that a near incompressible VF leads to the generation of the mucosal wave, a characteristics of VF dynamics relevant to phonation.

When looked at the VF deformation as shown in Figure 4.28, it is quite interesting to note that both the linear as well as non-linear modeling of the VFs resulted in a very similar output. The amplitudes of VF oscillation as well as the behavior of the VF deformation with time are strikingly close with maximum difference between the two being less than 8%. Moreover the dominant frequency of VF oscillation also remained nearly the same. This is an important conclusion, since there has been a lot of studies done using both the models without much emphasis on the actual difference between the two. This leads to us to believe that the VF deformations do not cross into the non-linear regime much to account for any significant difference between the two cases.

The instantaneous strain plots for the two case are presented next. Figure 4.29, Figure 4.30 and Figure 4.31 shows the three strain components ε_{xx}, ε_{yy} and ε_{xy} respectively for the two elastic models. There are a series of conclusions that can be drawn from these plots. First, all three strain components contours are qualitatively very similar for the two elastic models

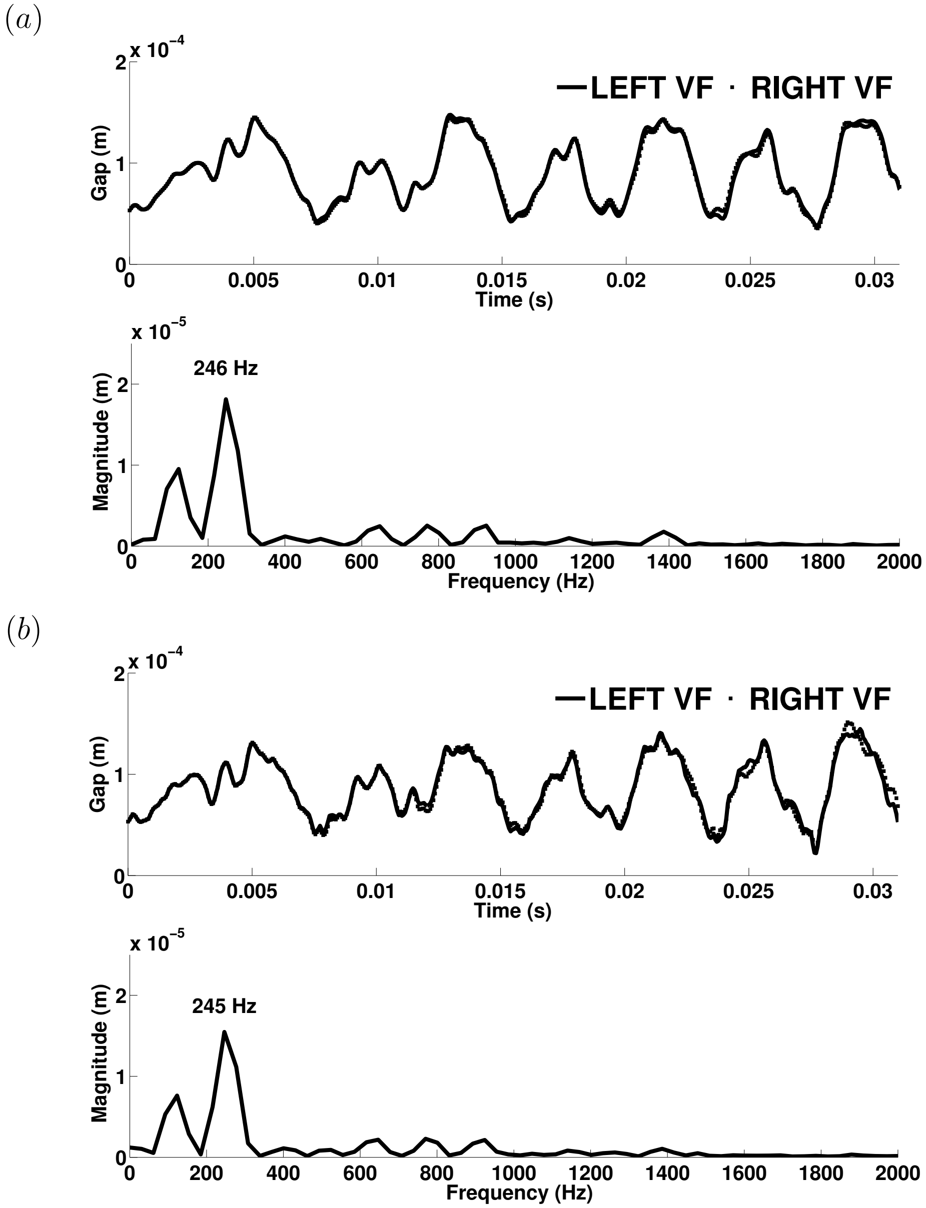

Figure 4.28: Minimum gap from centerline (top) and its FFT (bottom) with (a) non-linear hyper elastic model and (b) linear elastic model.

over the entire cycle. Second, the maximum strain values measured over the entire cycle are quantitively also very close for the two models. Finally, the maximum values of ε_{xx} and ε_{yy} are less than 8% for both the models. We notice that ε_{xy} is also constrained to a maximum value for 11%. These values of strain are not strictly non-linear and as such, the two models predict similar strains and VF displacements as they both adhere to a linear model type behavior.

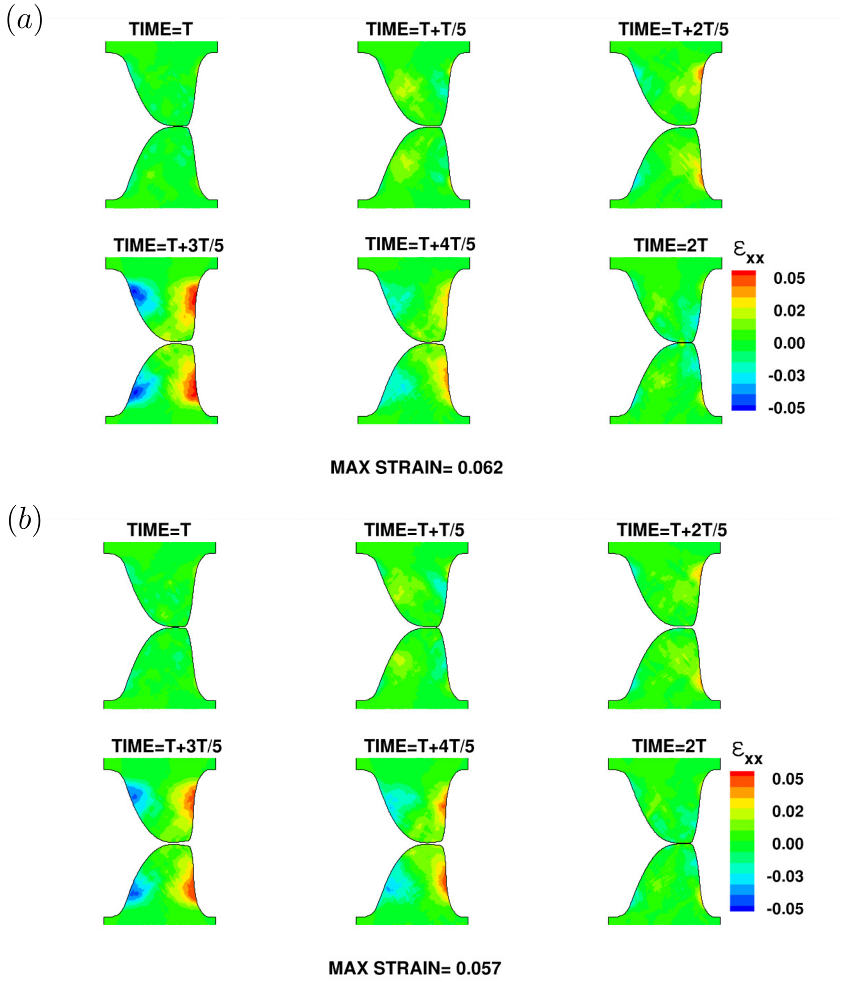

Figure 4.29: Instantaneous strain ε_{xx} plotted for one full cycle for (a) non-linear hyper elastic model and (b) linear elastic model. The maximum strain value over all the plots is indicated at the bottom.

Looking at the far-field acoustic characteristics for the two cases with pressure fluctuations plotted in Figure 4.32, it is noted that both the amplitude and the frequency of the waveform are quite close both qualitatively as

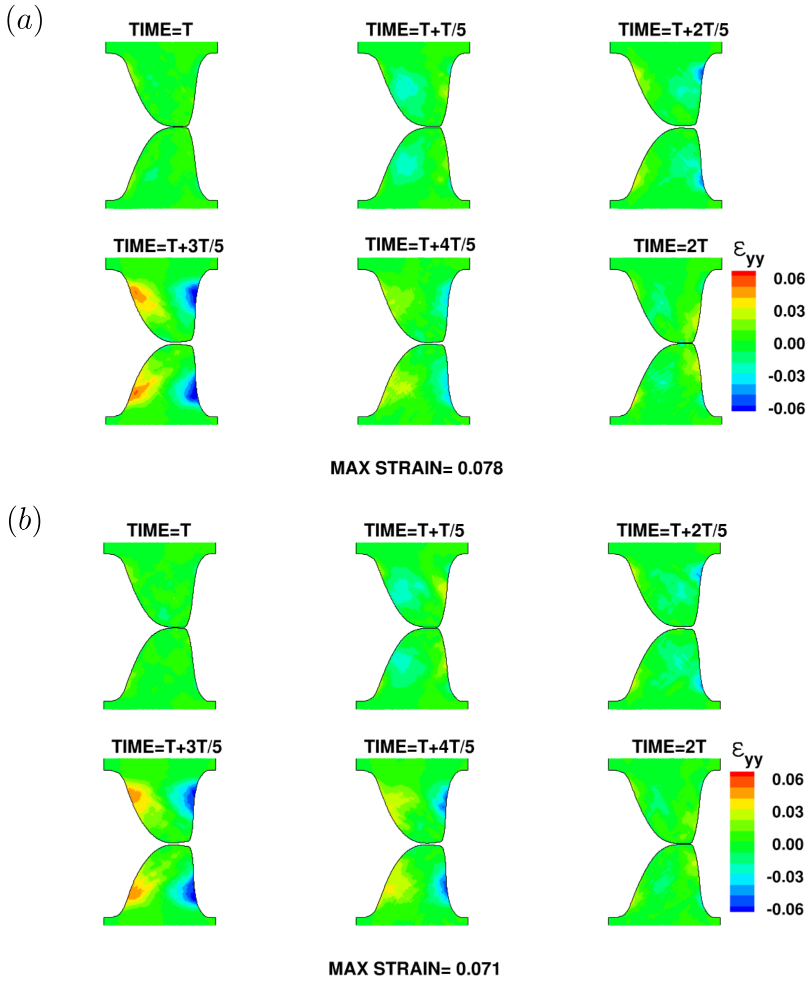

Figure 4.30: Instantaneous strain ε_{yy} plotted for one full cycle for (a) non-linear hyper elastic model and (b) linear elastic model. The maximum strain value over all the plots is indicated at the bottom.

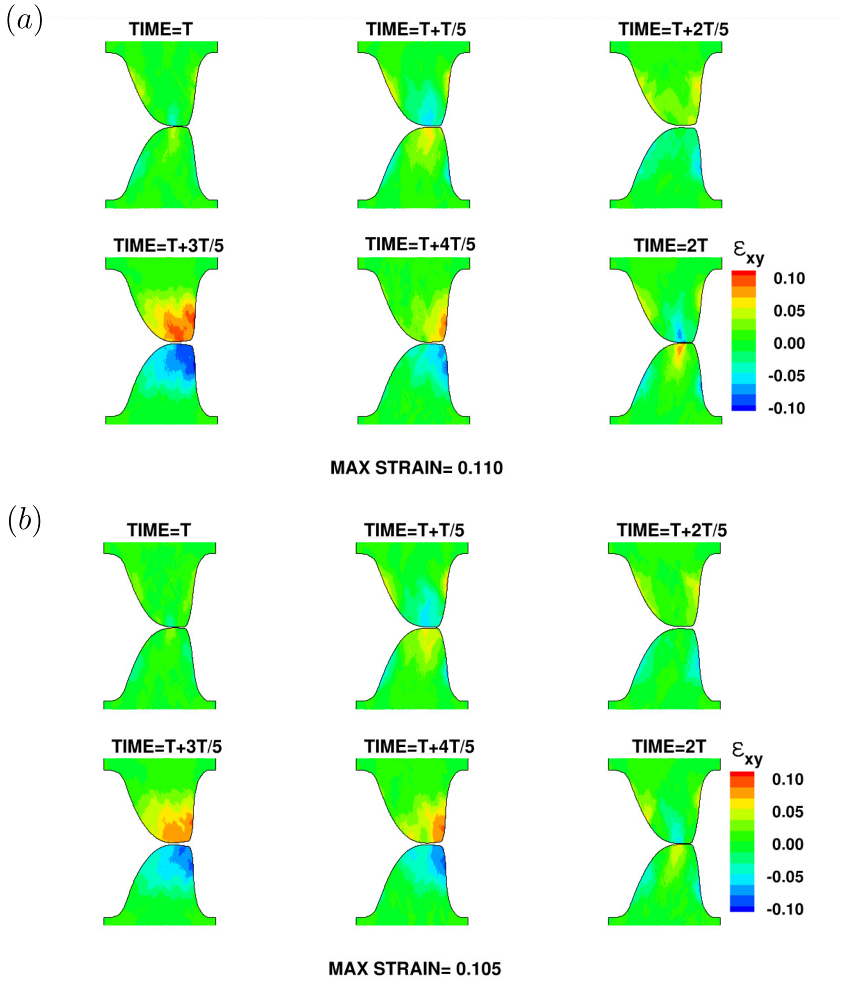

Figure 4.31: Instantaneous strain ε_{xy} plotted for one full cycle for (a) non-linear hyper elastic model and (b) linear elastic model. The maximum strain value over all the plots is indicated at the bottom.

well as magnitude wise. Again the maximum difference is less than 7%, which indicates that the two models predict similar behavior even in the far-field, which is also in accordance with the VF oscillation.

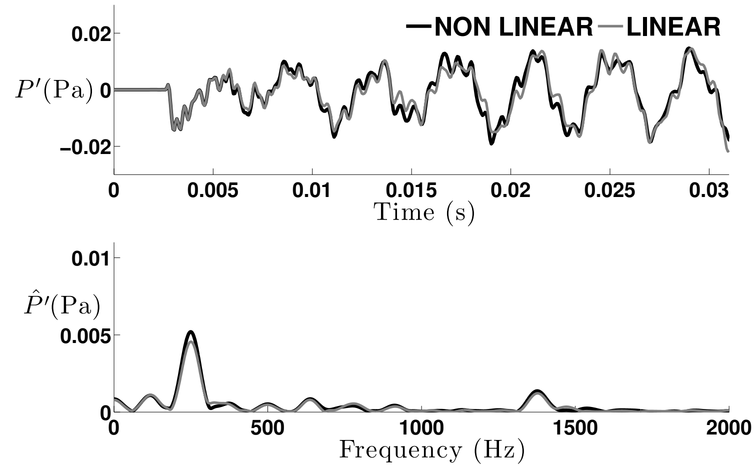

Figure 4.32: Far-field pressure fluctuation versus time comparison for non-linear hyper elastic versus a linear elastic model.

4.6 Simulation in Two Parts

So far the cases presented here have looked at simulations done with one full body domain, which presents a challenge for choosing the maximum time-stepping that is mainly governed by the instantaneous gap due to the motion of the VFs. If the simulation domain is broken into a vocal tract section and a section of the full body past the speaker's mouth, the work becomes easier since the part of the domain without the vocal tract is independent of the VF motion and can be run at significantly higher time stepping, thus saving on computational requirements. This is the motivation behind the current study. Moreover there have been attempts to do so in the past [156], wherein the flow inside the vocal tract was computed directly and voiced sound was propagated past the speaker's mouth using linearized perturbed compressible equation (LPCE). In this study, flow field in both the domains are computed using the compressible Navier-Stokes equation. The solution from the vocal tract domain at its exit (corresponding to the mouth exit), is fed to the second domain wherein the acoustic waves propagate into the ambient. Hence, the only difference between the full body simulation done in one part and the simulation done in two parts here is accounted from the fact that the former treats the mouth interface as a SAT block interface while for the latter case, it is an outflow-inflow combination. It is worth mentioning that the second part of the domain was run at a time step of approximately 10 times the maximum time step for the full body simulation done in one part. This is indeed a significant computational cost reduction and hence makes the study worth looking at.

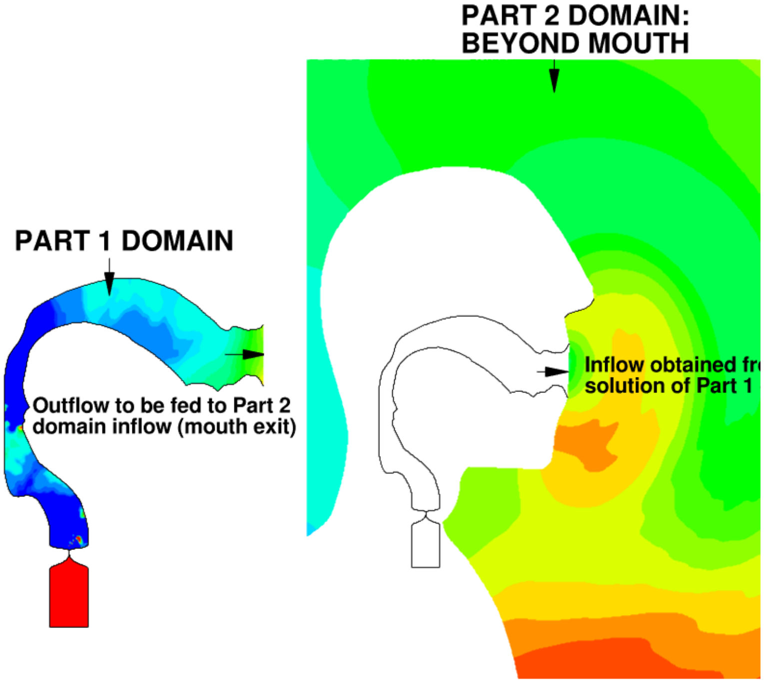

Figure 4.33: Two part simulation domain. Part 1 of the simulation is carried out in the vocal tract (VT) domain while part 2 is carried out in the full body domain past the mouth of the speaker.

Figure 4.34, presents the minimum VF gap from centerline for the two simulation scenarios. The qualitative behavior of the VF motion is quite the same for both the cases, with the maximum difference in amplitude over the entire time being less than 10%. The fundamental frequencies of vibration for the two cases remain unchanged. These point to the fact that the simulation done in two parts has been quite successful in preserving the VF dynamics when compared to the simulation done in one part. The next question to ask

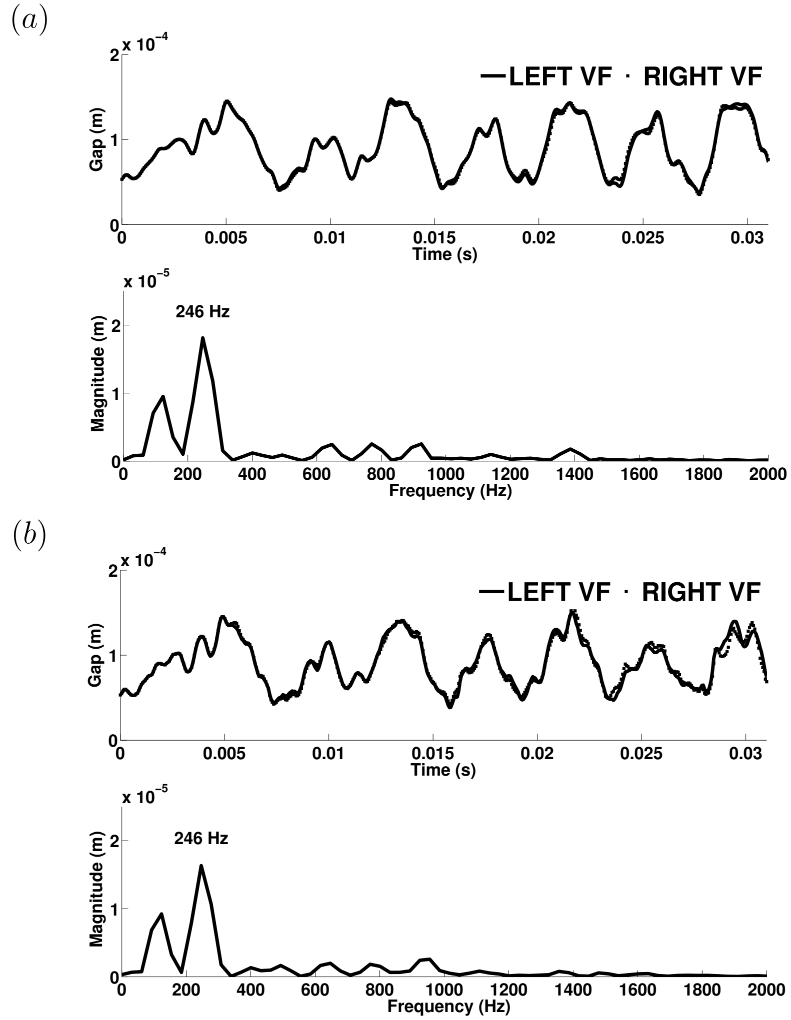

Figure 4.34: Minimum gap from centerline (top) and its FFT with (a) full body simulation done in one part and (b) full body simulation done in two parts.

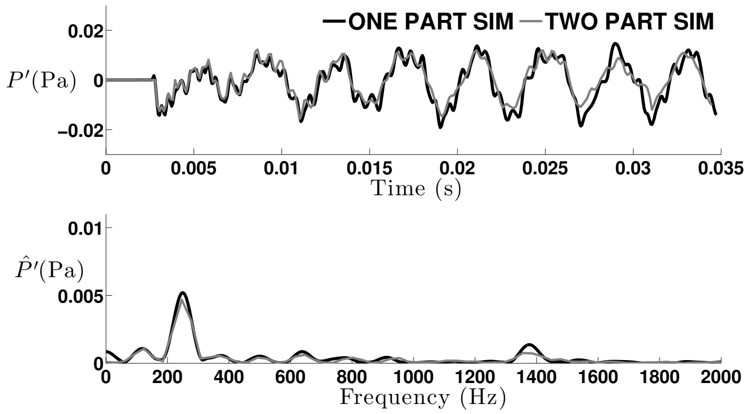

Figure 4.35: Far-field pressure fluctuation versus time comparison for full body simulation done in one part versus full body simulation done in two parts.

is whether the same will hold for the far-field acoustics. Pressure fluctuations at a point 2 feet past the speaker's mouth is plotted and shown in Figure 4.35, for the two scenarios. Interestingly, the two cases show significant similarity even in the far-field. The maximum difference noted here is less than 8%. The fundamental frequencies also align with each other and is consistent with the VF oscillations for both the cases. The OASPL for the two cases obtained from the time history of the pressure fluctuation differ by less than 0.5 dB. Thus, the close quantitative predictions obtained for both the cases leads to the usefulness of running the simulation in two parts with significantly reduced computational expense.

Chapter 5

Vocal Fold Viscoelasticity

This chapter presents an analysis of the effect of viscoelasticity on phonation by comparing it to its elastic counterpart. In order to first begin studying the problem it is imperative that the viscoelastic parameters are obtained by novel and justified means. As such the viscoelastic model (standard linear solid or SLS model) presented earlier in Chapter 3 is subjected to a curve-fitting with the available data in literature [106], which was obtained using a custom-built controlled-strain, linear simple-shear rheometer system. The study provides direct empirical measurements of viscoelastic properties at frequencies in the phonatory range. Details of measurement procedure and data procurement are presented in [106]. Figure 5.1 shows plots of experimental data for the loss and storage modulus fitted separately with the expression obtained by converting the viscoelastic model from time domain to frequency domain using fast Fourier transform. The fit gives the essential quantities corresponding to the model that is then used for simulation. These quantities are provided in Table 5.1. It is to be noted that the fit provides all the quantities for a fixed Poisson's ratio of 0.47.

Table 5.1: VF material properties for the viscoelastic case.

Layer	Young's modulus (kPa)	ν	β^{∞}	τ(s)
Cover	1.5	0.47	100	8.2E-06
Ligament	6	0.47	100	8.2E-06
Body	3	0.47	100	8.2E-06

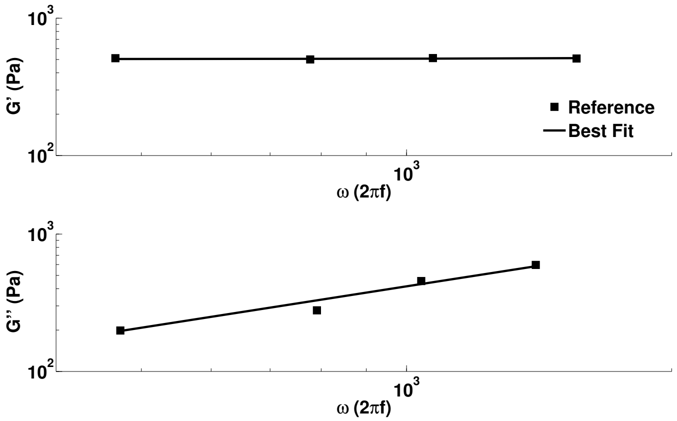

Figure 5.1: Curve fitting with SLS model against experimental data. Poisson's ratio is kept fixed and other parameters obtained from fit.

5.1 Viscoelastic solver validation

As mentioned earlier, a Standard Linear Solid model has been employed for capturing the viscoelastic nature of the VF. A validation study was conducted to check the correctness of the implementation. It is difficult to obtain analytical solution for a 3-D viscoelastic problem.

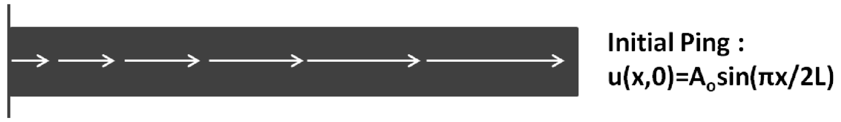

Figure 5.2: Problem setup to validate viscoelastic solver implementation.

Solver validation for the viscoelastic model can be done by simplifying the problem by using time evolution of end displacement of a slender(1-D) beam ($L = 1m$) subjected to an initial displacement field along its axis as shown in Figure 5.2. After this initial displacement the beam is left to itself. The plot of numerical solution obtained using the structural viscoelastic solver versus the analytical solution shown in Figure 5.3 match to within 0.001%. This completes the validation for the viscoelastic formulation.

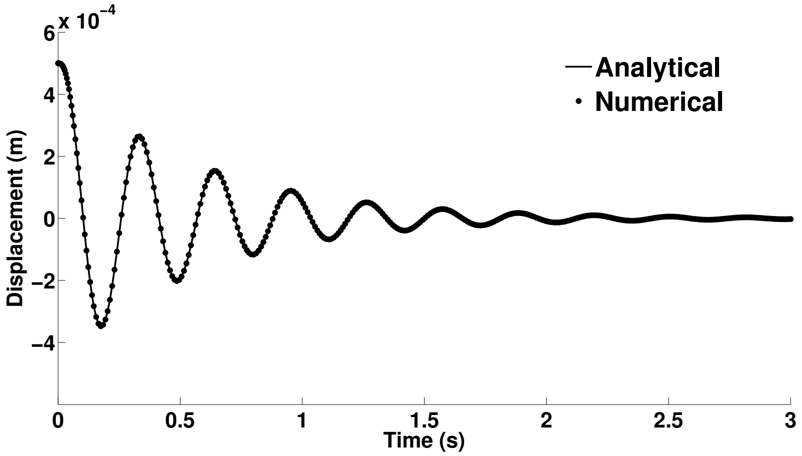

Figure 5.3: Displacement versus time for the numerical and analytical solution for the viscoelastic solver validation problem.

5.2 Viscoelastic vs elastic only comparative analysis

A comparative study is done to analyze the effect of viscoelasticity by running the simulation using only elastic and then by switching on the viscoelasticity formulation. Thus the elastic modulus and Poisson's ratio values were kept the same for both the simulations. Both near field and far field characteristics have been studied. A plot of the VF gap from centerline as shown in Figure 5.4, reveals some very significant differences between the two cases. First, it is noticed that the VF deformation show a marked reduction in amplitude for the viscoelastic case owing to the damping effect of the viscous nature of the VFs. Second, the viscous effect has negligible impact on the oscillation frequency of the VFs, as the peak fundamental frequency for both the cases are nearly the same. These have also been observed in another study [72], where an increase in the viscous parameter resulted in a decrease in the oscillation amplitude without affecting the frequency of oscillation. Another interesting aspect of the viscoelastic effect is the significant drive to symmetrical VF vibration when compared to the elastic case. The left and right VFs show marked asymmetry with time evolution for the elastic only case, while the viscoelastic case keeps the symmetry well intact. To understand this better, plots of VF dynamics overlaid with vorticity is considered in Figure 5.5. One full time period is considered for both the cases. Right away, it is noticed that for the elastic only case, the jet deflection is significantly higher and stochastic in nature near the glottal exit. On the other hand, the viscoelastic case, tries to preserve a minimal jet deflection at the glottal exit. The resulting lack of asymmetry just past the VF exit, explains the symmetrical VF motion as was noted it Figure 5.4. This is an interesting example of how changes in the material properties of the VFs result in changes to the fluid dynamics, which in turn effect the VF dynamics.

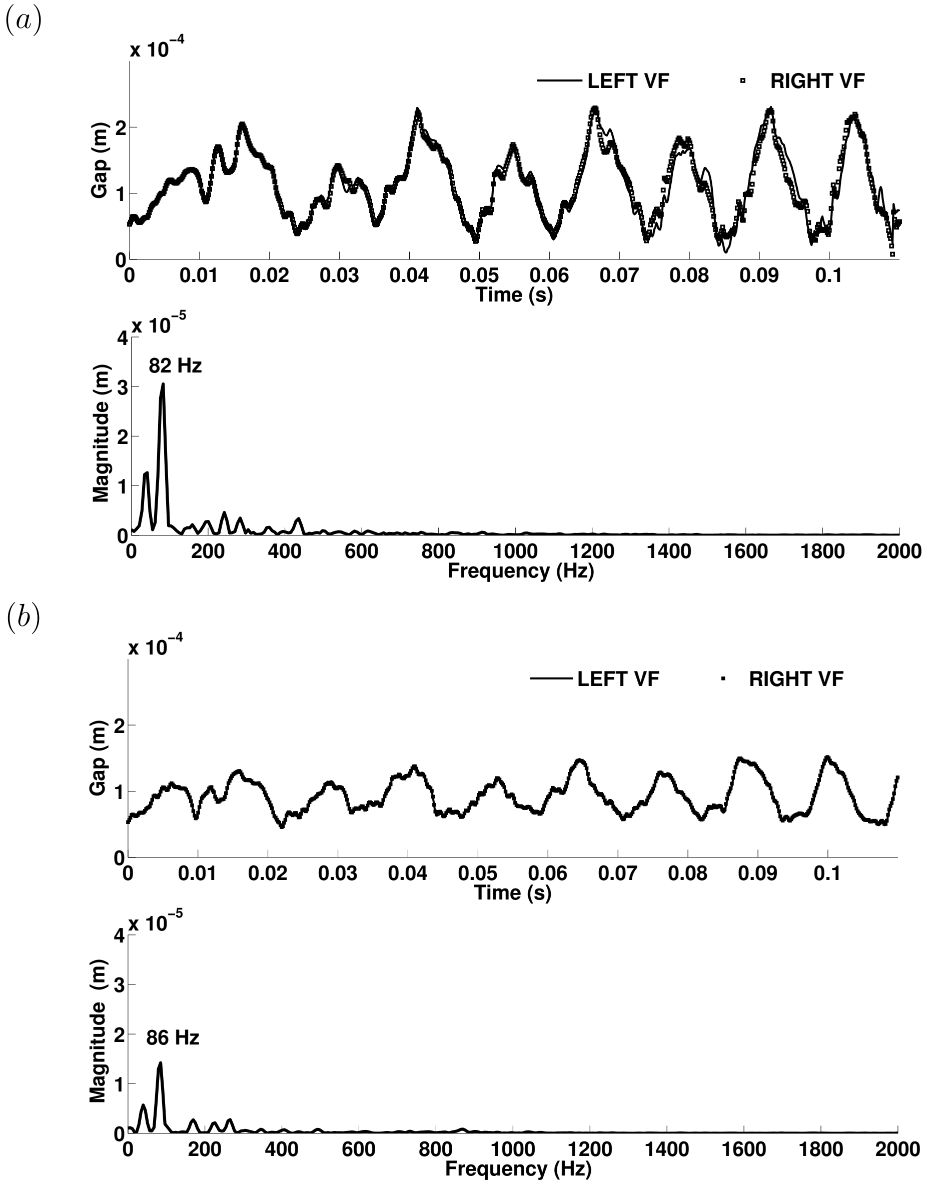

Figure 5.4: VF gap from centerline and the corresponding FFT of the left VF for (a) elastic only case and (b) viscoelastic case.

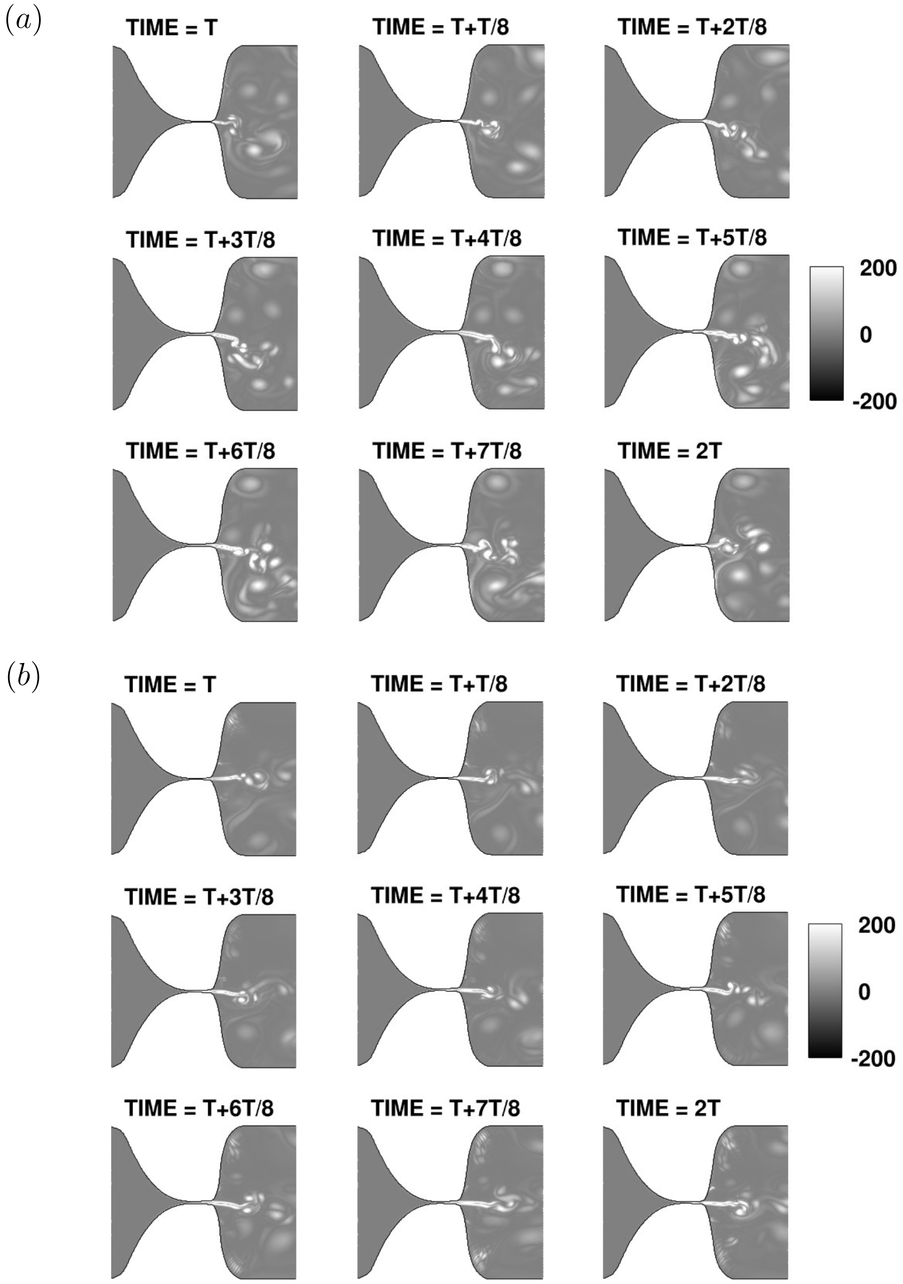

Figure 5.5: Vocal fold dynamics and vorticity contours (one full cycle) for (a) elastic only case and (b) viscoelastic case.

The effect of tissue viscoelasticity demonstrated significant impact on the flow field. As such it is imperative to look at the effects at far-field. A plot of OASPL in Figure 5.6, for the two cases, is analyzed first. The acoustic intensity show a significant reduction for the viscoelastic case. The maximum difference between the two cases being close to 3 dB. This can be attributed to the motion of the VFs. For the viscoelastic case, the VF deformation amplitudes were considerably reduced with respect to the elastic only case. This would in turn result in reduced displacement of the nearby fluid, which is directly linked to and is analogous to the monopole source term in the acoustic field. It has been shown [64] in a study, that the dominant source of acoustic energy in phonation is indeed the monopole term resulting from the fluid mass displacement due to the motion of the VFs.

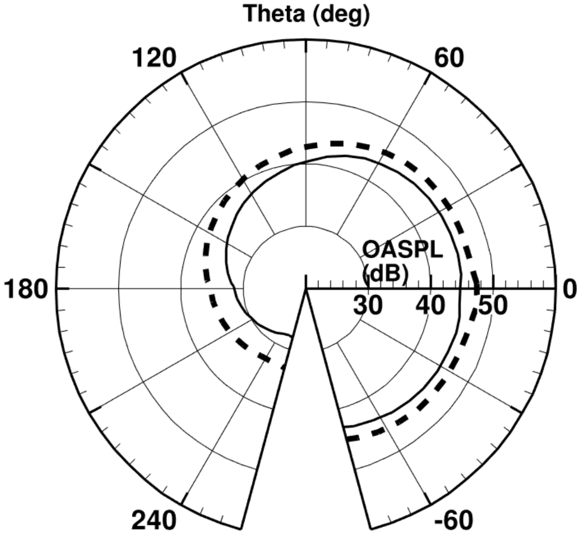

Figure 5.6: Sound pressure level directivity plot on a circle centered at the speaker's mouth and a radius of 2 feet. Solid and dashed lines correspond to viscoelastic and elastic only cases respectively.

A closer look at the pitch content for the two cases Figure 5.7, obtained via FFT of the pressure fluctuation data measured at a point directly past the speaker's mouth, shows that the fundamental frequency remains unchanged. This was also observed for the VF deformation.

As such, it can be inferred from the above observations that viscoelasticity

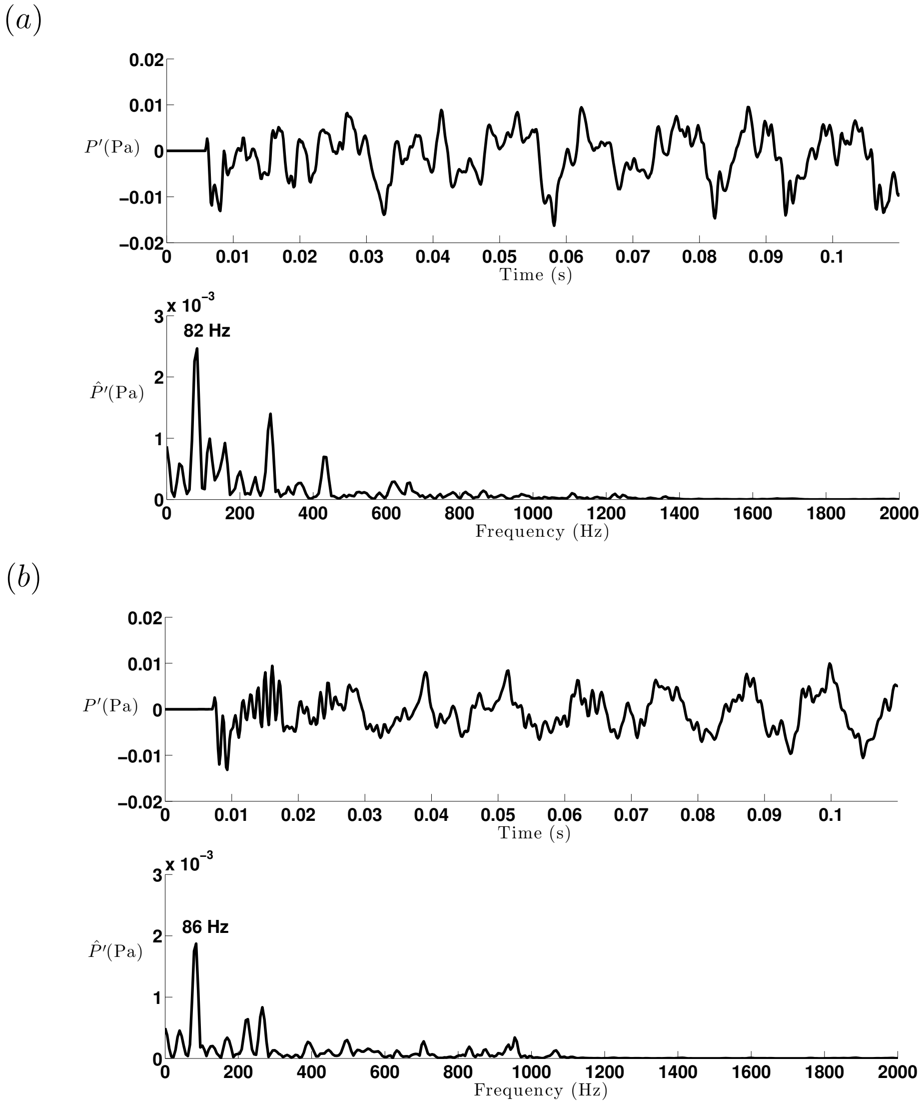

Figure 5.7: Far-field pressure fluctuation versus time and its corresponding FFT at a location directly facing the speaker's mouth for (a) elastic only case and (b) viscoelastic case.

plays an important role in keeping the VF deformations damped and close to symmetric which in turn has significant impact on both the near-field glottal flow and eventually on the far-field acoustics. The use of viscoelasticity in modeling tissue characteristics for simulation purposes is not only justified but also cannot be overlooked.

Chapter 6

Vocal Fold Pathology

The disruption of speech is traumatic. When the vocal fold properties change, or when one vocal fold becomes unusable, there is a corresponding change or loss of voice. This could range from temporary VF irregularity such as inflammation [109] and vocal fold scarring [110] to more permanent condition like unilateral vocal fold paralysis and bilateral vocal fold paralysis [111, 112]. This chapter provides an analysis based on simulation of the various pathological conditions and relating the results thus obtained to clinical data.

6.1 Physical model

A two-dimensional anatomically representative vocal tract geometry is used for the simulations as shown in Figure 6.1. The model consists of an anatomically representative vocal tract geometry and is chosen to accurately predict the phonation onset. It has been shown in a recent study [159], that supraglottal instabilities which are affected by the shape of the vocal tract, in turn affects the intra-glottal flow which then affects the phonation onset time. A linearly time-varying pressure ($dP/dt = 34.6Pa/ms$) is applied at the inflow while the outflow is maintained at atmospheric conditions.

A three layer model of the VFs composed of the cover, ligament and the body as described in Chapter 4 is used.

For the VF stiffness asymmetry study, two series of analyses were conducted. In the first series, the left VF body layer was kept at a constant stiffness of 25 kPa, while the right VF body layer stiffness was kept at 25, 50 and 75 kPa. The second series had the left VF stiffness of 75 kPa, while the right VF stiffness took the values of 75, 50, 25 kPa. The same has been illustrated in Table 6.1 and Table 6.2.

The one quantity which was particularly calculated was the phonation threshold pressure (PTP), which is defined as the minimum subglottal pres-

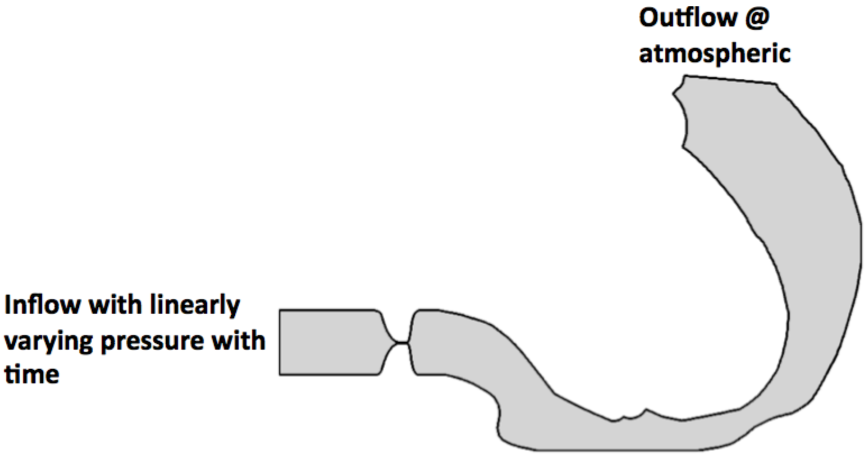

Figure 6.1: Schematic of the fluid domain.

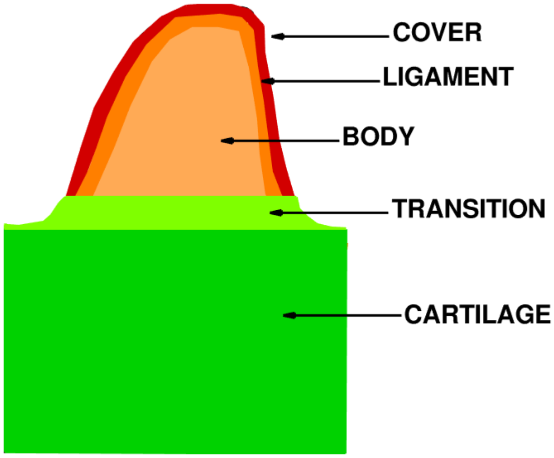

Figure 6.2: Vocal fold model showing the different layers.

Table 6.1: VF material properties for series 1.

Case	E_{body} (kPa)	E_{cover}	$E_{ligament}$
1	25(L), 25(R)	25(L,R)	100(L,R)
2	25(L), 50(R)	25(L,R)	100(L,R)
3	25(L), 75(R)	25(L,R)	100(L,R)

Table 6.2: VF material properties for series 2.

Case	E_{body} (kPa)	E_{cover}	$E_{ligament}$
1	75(L), 75(R)	25(L,R)	100(L,R)
2	75(L), 50(R)	25(L,R)	100(L,R)
3	75(L), 25(R)	25(L,R)	100(L,R)

sure required to initiate and sustain VF vibration. The time-varying pressure at inflow drives the flow through the glottis and the flow rate at the glottal exit is measured. The DC component of the flow rate is then subtracted from the original waveform, to give the periodic wave component [170]. For the current analysis, the AC component is filtered and the point where the signal shows an onset of sustained periodicity is defined as the phonation onset time. The subtotal pressure corresponding to the phonation onset time is then obtained as the desired PTP (Figure 6.3). These simulations employ a highly refined non-uniform 2194 × 121 cartesian grid for the fluid domain and 915 × 201 cartesian grid for the solid domain.

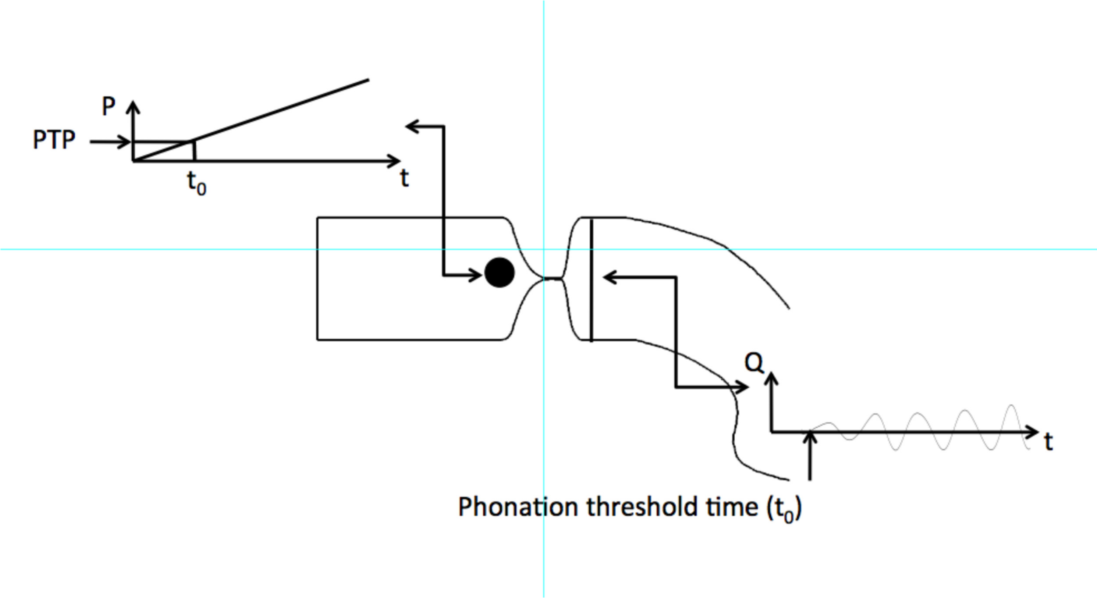

Figure 6.3: PTP determination method.

6.2 VF stiffness asymmetry: Series 1

The VF gap from centerline is plotted for the three cases in Figure 6.4. The first case with both VFs having the same stiffness values, exhibit near symmetric motion with time. A slight asymmetry build up is a result of the asymmetric flow field features past the VFs. As the right VF stiffness is further increased to 50 kPa keeping the left VF unchanged (25 kPa), a much stronger asymmetry is observed. The right VF with a higher value of stiffness tends to vibrate faster than the left VF. Moreover, the amplitude of vibration is reduced for the more stiffer VF. This trend is strengthened as the right VF is set to an even higher stiffness of 75 kPa. To clarify, the fundamental frequencies of vibration of both the VFs and the flow rate at a location just downstream of the VF exit is shown in Figure 6.5. Clearly for case 1, the flow rate is in sync with the motion of the two VFs, while for case 3 with maximum asymmetry, the flow rate follows the motion of the less stiffer VF. Interestingly for case 2, the flow rate tends to show oscillatory behavior which lies in between the fundamental frequencies of the two VFs. This points to the fact that the subjected asymmetry for the VFs is not sufficient to drive the flow to resort to the motion of either VFs. These observations have been reported in a similar study done earlier [114].

Once the effect of VF stiffness asymmetry on the dynamics of VF motion and the resulting flow field is established, the analysis is continued to obtain the PTP values for the three cases. Figure 6.6 shows the original flow rate and its extracted AC component which is then filtered using a second order low pass Butterworth filter [172]. This removes all the higher fluctuating components out and renders a smoothly varying waveform which is easier to analyze [171]. The effect of increasing asymmetry of the right VFs on the phonation onset time is clearly noted. The phonation onset time shifts to the right from case 1 to case 3. This implies that the subglottal pressure required to initiate and sustain phonation increases as the asymmetry is increased and is more dependent on the VF with higher stiffness. This observation is again verified in the study done by Zhang et al. [114]. Further the values of PTP for the three cases are plotted in Figure 6.6 which shows significant increase in the values of PTP with rising asymmetry. This is a very useful observation in clinical studies wherein the patients suffering from conditions like this find it difficult to phonate than usual [111].

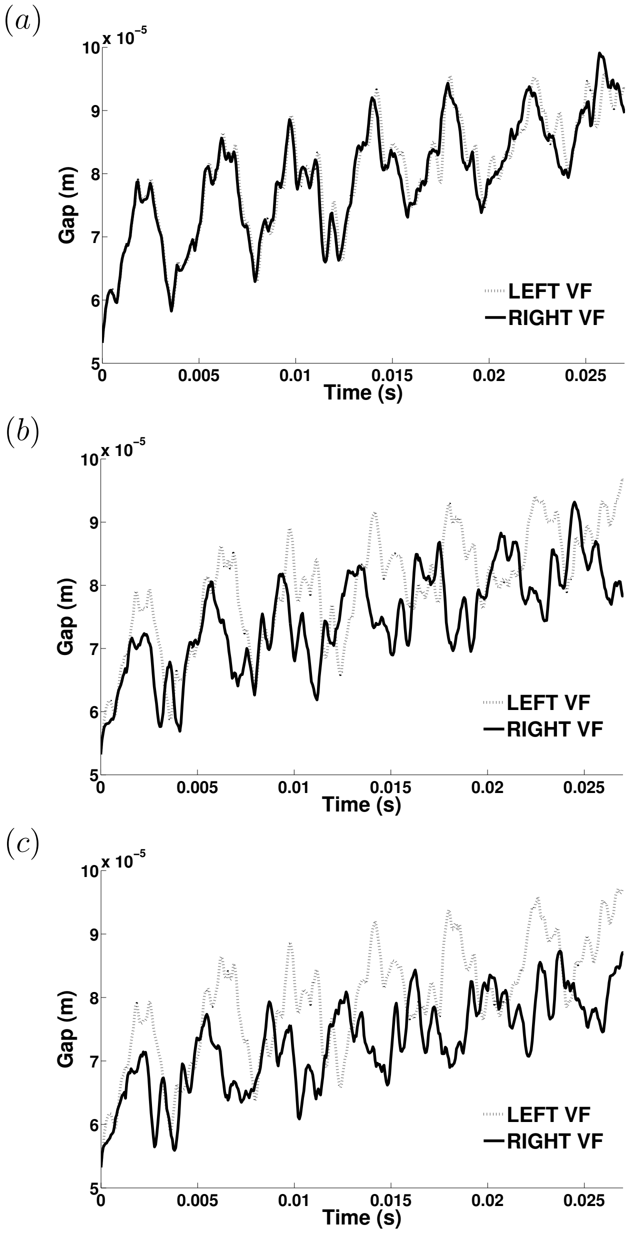

Figure 6.4: VF gap from centerline for the stiffness asymmetry series 1 for (a) Case 1 (b) Case 2 (c) Case 3.

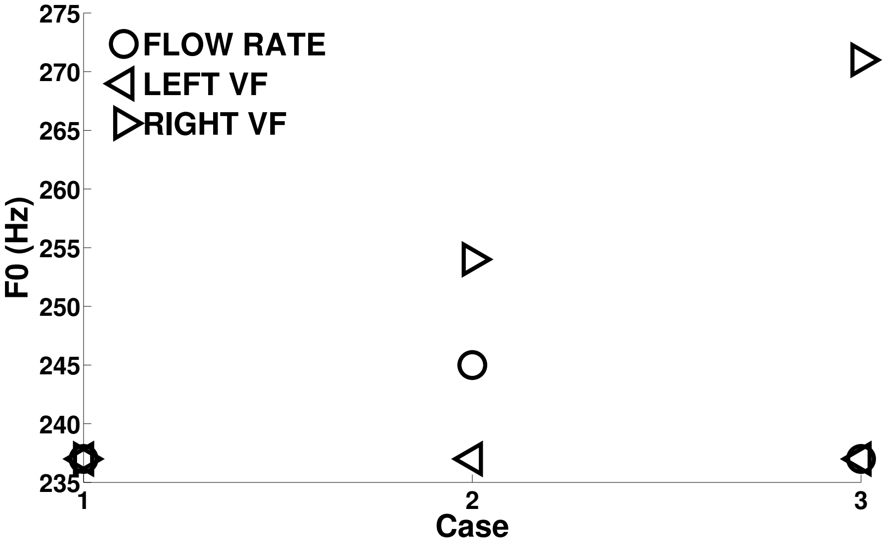

Figure 6.5: Fundamental frequencies for left and right VF gap variation from centerline and the flow rate variation at a location just past the VFs for the stiffness asymmetry series 1.

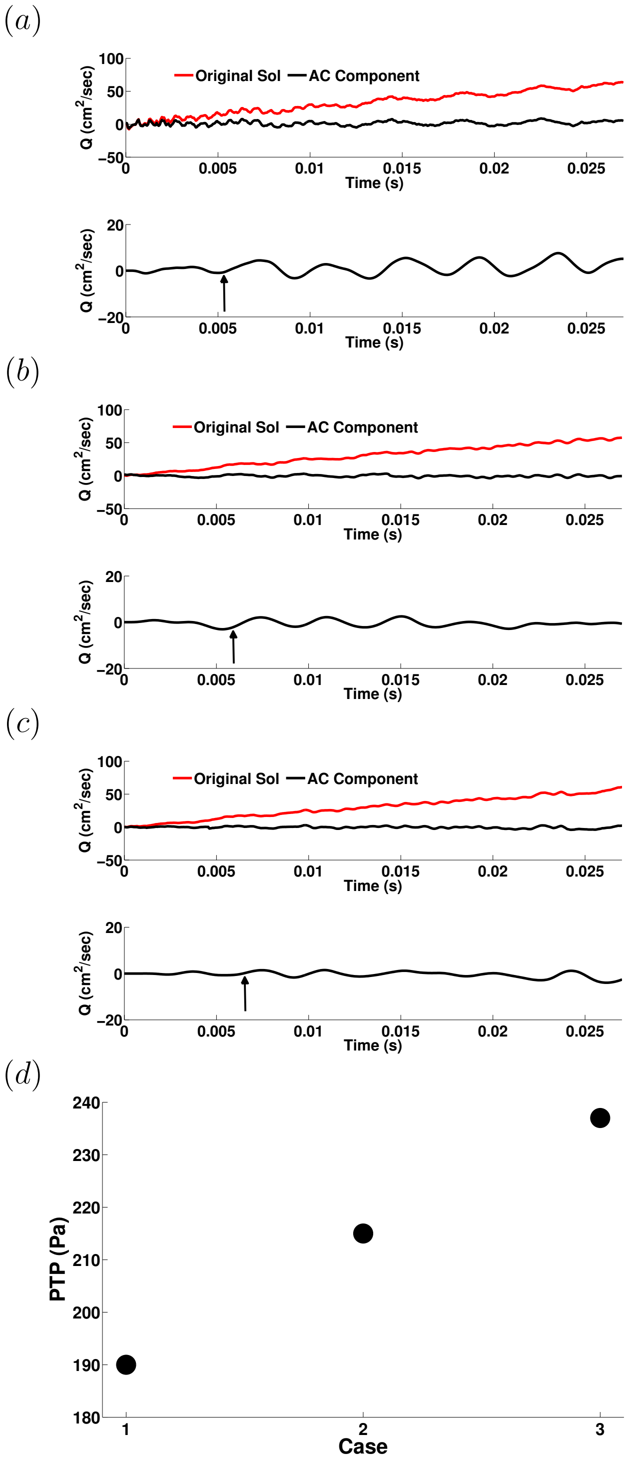

Figure 6.6: Original and AC component of flow rate (top) and the filtered AC component plot (bottom) for the stiffness asymmetry series 1 (arrow indicating phonation onset time) for (a) Case 1 (b) Case 2 (c) Case 3; (d) PTP values for the three cases of series 1.

6.3 VF stiffness asymmetry: Series 2

In this study the role of asymmetry is reversed. The left VF is now held at a higher stiffness of 75 kPa, while the right VF undergoes a decrease of stiffness from 75 kPa to 25 kPa. As in Sec. 6.2, the gap from centerline for the three cases here is plotted in Figure 6.7 to see the effect of this imposed asymmetry on the VF dynamics. Again when the two VFs have identical stiffnesses (Case 1), the resulting motion of the VFs tend to be near symmetric with slight asymmetry build up due to flow asymmetry past the VFs. As the right VF stiffness is further decreased to 50 kPa keeping the left VF unchanged, a much stronger asymmetry is observed. The right VF with a lower value of stiffness tends to vibrate slower than the left VF. Opposite to the behavior in series 1, the amplitude of vibration is increased for the less stiffer VF. This trend is strengthened as the right VF is set to an even lower stiffness of 25 kPa. The fundamental frequencies of vibration of both the VFs and the flow rate at a location just downstream of the VF exit is shown in Figure 6.8. Again for case 1, the flow rate is in sync with the motion of the two VFs, while for case 3 with maximum asymmetry, the flow rate follows the motion of the less stiffer VF. For case 2, the flow rate tends to show oscillatory behavior which lies in between the fundamental frequencies of the two VFs. This is again in accordance with the observation for series 1, wherein the effect of lesser stiffness asymmetry between the two VFs is not a sufficient driving factor to make the flow follow one of the VF motion. These observations have also been reported in Zhang et al. [114].

Next in the analysis is the effect of the VF stiffness asymmetry on the PTP. Figure 6.9 shows the original flow rate and its extracted AC component which is then filtered using a second order low pass Butterworth filter as was also reported in Sec. 6.2. The phonation onset time shifts to the left from case 1 to case 3. For case 1, with both VFs at a higher stiffness level, the phonation onset time is clearly shifted further due to the fact that it takes even more of an effort to initiate phonation for this case. This observation is again verified in the study done by Zhang et al. [114]. However, as one of the VFs is made less stiffer, the phonatory effort is reduced. Further the values of PTP for the three cases are plotted in Figure 6.9 which shows significant decrease in the values of PTP with rising asymmetry.

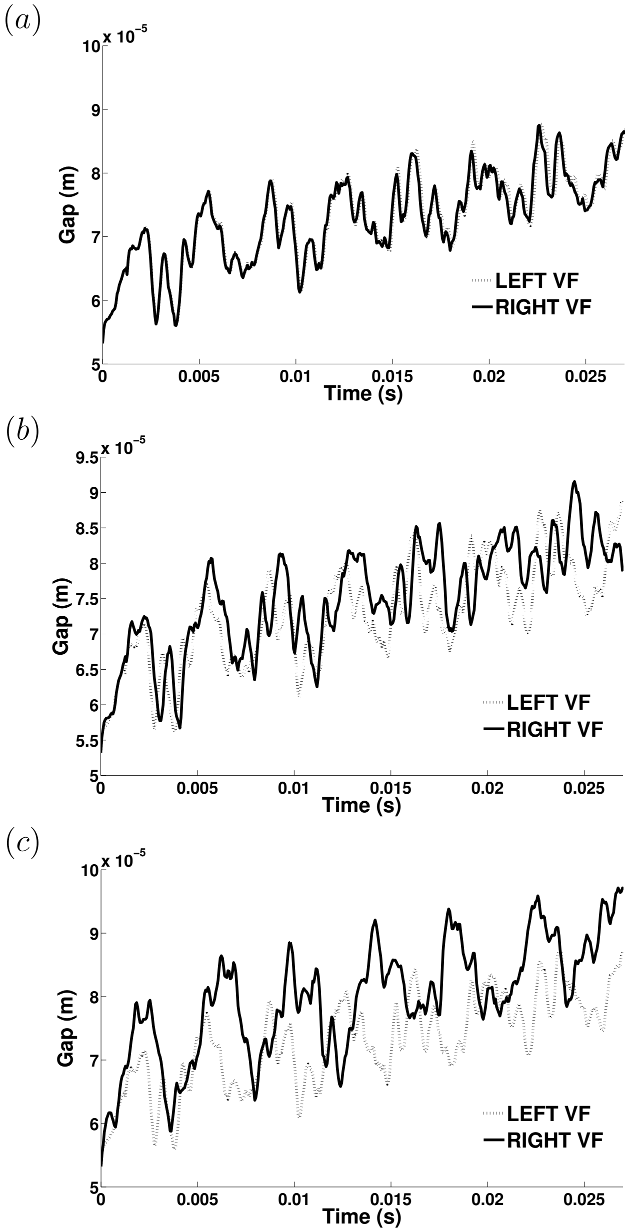

Figure 6.7: VF gap from centerline for the stiffness asymmetry series 2 for (a) Case 1 (b) Case 2 (c) Case 3.

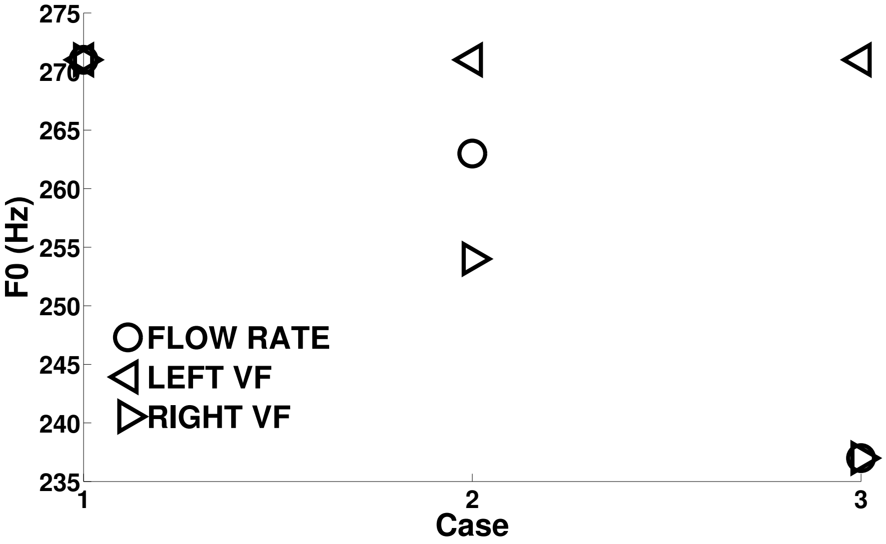

Figure 6.8: Fundamental frequencies for left and right VF gap variation from centerline and the flow rate variation at a location just past the VFs for the stiffness asymmetry series 2.

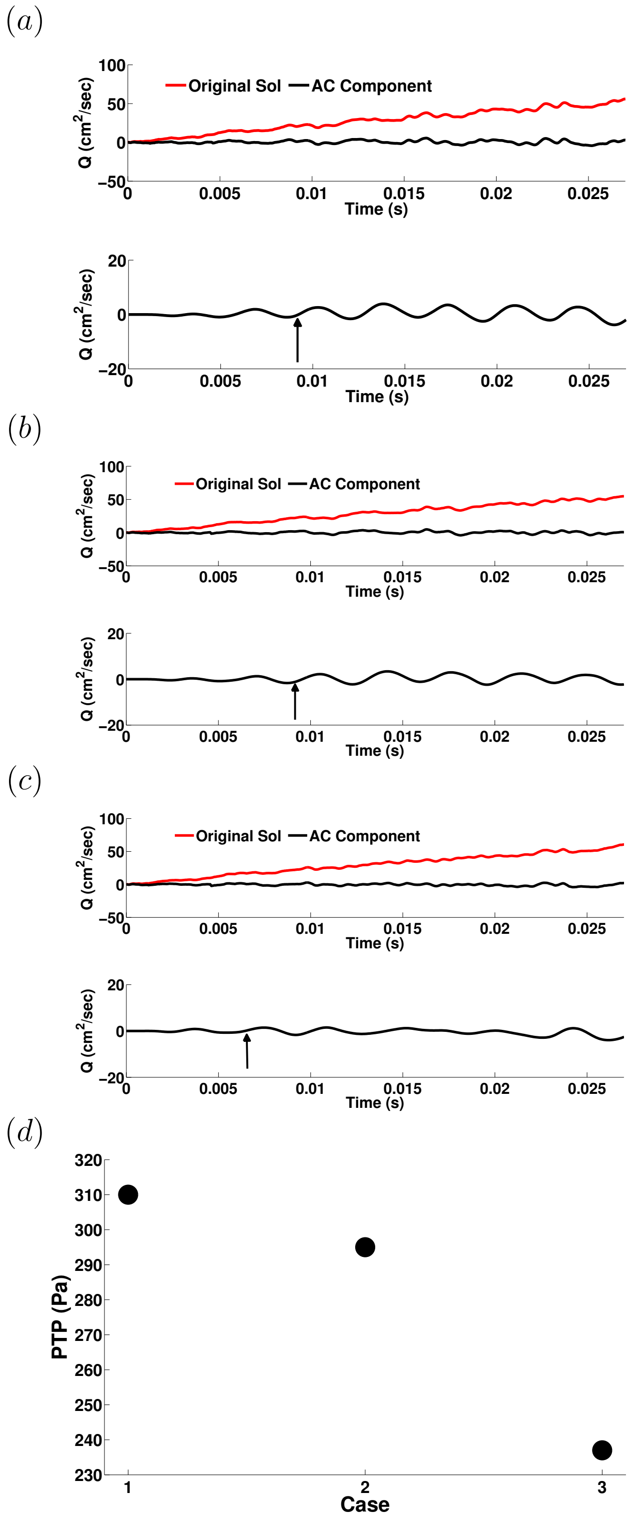

Figure 6.9: Original and AC component of flow rate (top) and the filtered AC component plot (bottom) for the stiffness asymmetry series 1 (arrow indicating phonation onset time) for (a) Case 1 (b) Case 2 (c) Case 3; (d) PTP values for the three cases of series 2.

6.4 UVFP and medialization laryngoplasty

For the VF pathology study, a comparative analysis is conducted by first looking at the case of UVFP and then a remedial case of medialization larygoplasty. Figure 6.10 shows the sketch of the VF structural domain used for these two cases. In order to imitate UVFP, the affected VF is pulled to intermediate position and has stiffness reduced to 80% of its healthy counterpart [107]. For the medialization study, the same VF was adducted close to the centerline to meet the healthy counterpart using an implant which had a stiffness value of 5 MPa [169]. This was done to closely simulate clinical diagnostic procedure for treating patients with UVFP.

For the current analysis, a different approach is utilized to obtain PTP called the method of continuous wavelet transform. The 1D continuos wavelet analysis package of MATLAB is used for this purpose [171]. This method enables one to correlate the waveform or flow rate signal with an analyzing analytic wavelet to generate a frequency versus time plot. This again is used to identify the phonation onset time by detecting onset of periodic structures.

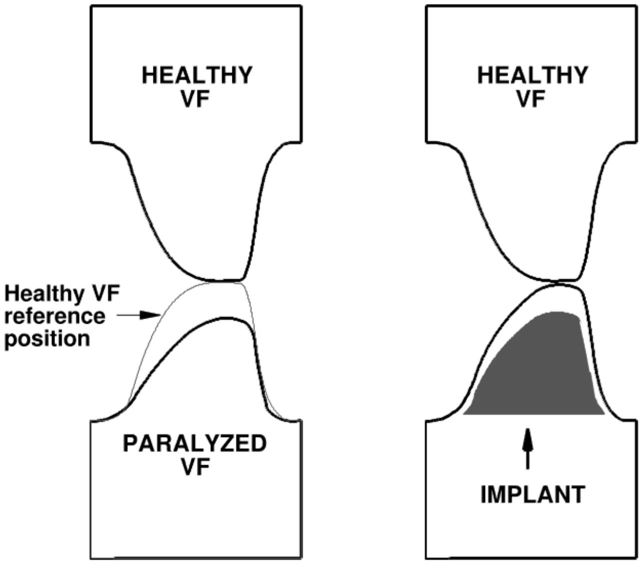

Figure 6.10: Vocal fold model for UVFP and medialization laryngoplasty showing implant placement.

The current analysis is aimed at understanding how patients suffering from UVFP demonstrate increased phonation difficulty and then how it can be eased via medialzation laryngoplasty. Before diving into these scenarios, a case of both VFs being healthy was studied to establish a benchmark. The simulation procedure has been outlined in Sec. 6.1. In this section, phonation onset time has been obtained from continuous wavelet transform of the AC component of the flow rate signal measured just past the VF exit. The benefit of using this method is that it allows to break the complex information and patterns into elementary form. In this case, it helps in looking at the entire waveform without the need to filter it. Moreover, the information for both PTP and the dominant frequencies in the flow is captured at once and will be discussed next.

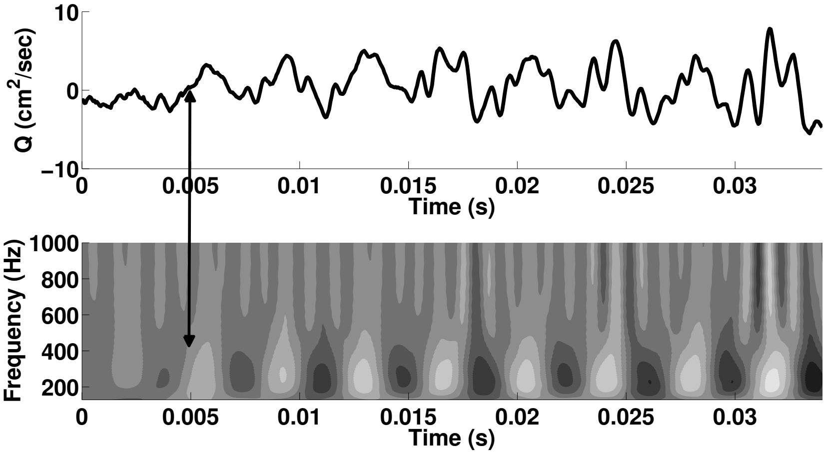

Figure 6.11: AC component of the flow rate (top) and cwt plot (bottom) for both healthy VFs case (double arrow indicating phonation onset time).

For the case with both VFs healthy, a plot of the AC component of the flow rate waveform and its continuous wavelet transform is depicted in Figure 6.11. The frequency versus time plot obtained from continuous wavelet transform, shows periodic patterns appearing around 0.0051 sec which is noted as the phonation onset time. These patterns then show a sustained existence. The PTP corresponding to this phonation onset time is approximately 180 Pa. Several clinical studies conducted using air-puff tests have indicated that for subjects with healthy VFs the normal PTP would lie between 180 to 400 Pa [124–126]. This plot also provides us information about the dominant frequency present in the waveform, which is concentrated around the 240 Hz mark. This has also been observed in a study done with similar VF material properties [72].

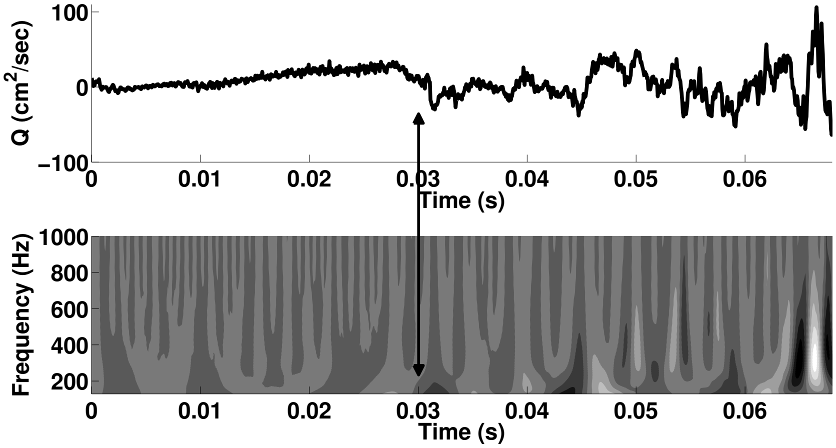

Figure 6.12: AC component of the flow rate (top) and cwt plot (bottom) for UVFP case (double arrow indicating phonation onset time).

The case of a patient suffering from UVFP is discussed now. Figure 6.12 shows the continuous wavelet transform of the flow rate waveform for this case. There are marked differences between this case and the benchmark case of the healthy VFs. First and foremost the phonation onset time is clearly shifted way to the right indicating a higher PTP. For this case, the value of PTP is approximately 1080 Pa. Similar values were reported in other clinical studies conducted with patients suffering from UVFP [112,124]. Particularly, PTP for UVFP were reported to be greater than 800 Pa [112], and was termed as severe deficit. Such high values of PTP were indicative of the extreme difficulty faced by the patient to phonate. Moreover, patients were reported to have a breathier voice which is as a result of flow leaking past the VFs, since the affected VF is unable to adduct to the centerline and meet its healthy counterpart. In Figure 6.12, this is highlighted by the absence of a clear dominant frequency in the continuous wavelet transform plot and also through the non-uniform nature of the flow rate waveform itself. Thus the simulation is able to capture all the essential aspects of UVFP and is consistent with values reported by clinical studies.

This analysis is concluded by doing a simulation in which the affected VF is pushed to the centerline via an implant (medialization laryngoplasty) with the aim to be able to recover phonation. Figure 6.13 shows the continuous wavelet transform of the flow rate waveform for this case. At once it is noted that the flow rate waveform begins to show much more uniform behavior as opposed to the UVFP case where flow leakage was dominant. Periodic patterns similar to the healthy VFs case reappear as is seen in the continuous wavelet transform of the flow rate waveform. The phonation onset time noted here is 0.008 sec, which corresponds to a PTP of 280 Pa. This lies in the normal range of healthy phonation [124–126]. The dominant frequency present in the waveform, which is concentrated around the 250 Hz mark shows recovered phonation pitch characteristics. Thus not only the uniform flow rate characteristics but also the ease in phonatory effort was realized via this modification to the affected VFs, which is in accordance with clinical treatment of UVFP. An inherent limitation of this analysis lies in the fact that it would be more comprehensive to include VF damping effect due to its viscoelastic nature and such an analysis can form a part of future work.

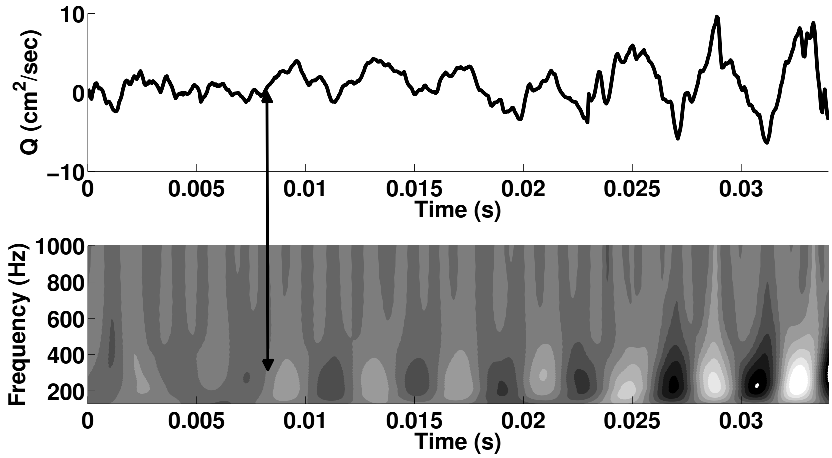

Figure 6.13: AC component of the flow rate (top) and cwt plot (bottom) for medialization laryngoplasty case (double arrow indicating phonation onset time).

Chapter 7

Full Body Simulation in 3D

Till this point, the discussion was based on two-dimensional simulations of human phonation. This chapter looks at the three-dimensional counterpart of the full body simulation done in two parts. The computational advantage of conducting simulation in two parts has already been highlighted in Chapter. 4.

7.1 Physical model

The fluid domain is broken down into two parts. The first part of the domain only consists of the vocal tract as shown in Figure 7.1. The 3D domain shown here has been obtained from the 2D domain by extruding the 2D domain which is motivated by a close simulation study done by Zheng et al. [75]. It is to be noted that the VFs here have been rotated to align with the sagittal plane. The grid resolution for this domain is maintained equivalent to that of the 2D case (refer to Table. 4.1) with 61 points in the anterior-posterior direction.

Part two of the fluid domain consists of the region of the full body extending from the exit of the mouth to ambient as shown in Figure 7.2. This domain is made up of a total of 11 blocks to incorporate the complex geometrical variation of the head and body. The grid resolution is kept equivalent to the two-dimensional case. The domain encompasses sufficient space for acoustic waves to propagate. The simulation is then carried out as follows. The solution from the vocal tract domain at its exit (corresponding to the mouth exit) is fed to the second domain wherein the acoustic waves can propagate into the ambient.

On the structural side, the two VFs in 3D are again obtained by extruding the 2D geometry by an equal amount as that of the vocal tract domain. The far ends of the VFs in the anterior-posterior directions are held fixed.

Figure 7.3 shows the 3D vocal fold domain and a cross-section of it showing the various layers. The material properties of the VFs are chosen to be the same as in a previous study [75]. The VFs are modeled as a transversely isotropic material. Table. 7.1 shows the material properties of the three layers of the VFs as adopted from the above study. Here E_p is the transverse Young's modulus, ν_p while is the in-plane transversal Poisson's ratio. In the longitudinal direction, E_{pz} represents the longitudinal Young's modulus, G_{pz} is the longitudinal shear modulus and ν_{pz} is the longitudinal Poisson's ratio. As in the study done by Zheng et al. [75], the longitudinal Young's modulus is set to equal to 10000 times the transverse Young's modulus to enforce the in-plane motion constraint [174]. A kinematic constraint is applied to prevent the VFs from colliding. It is to be noted that for a 3D case, the glottal flow has an additional degree of freedom and will not remain as confined as in the 2D case, and might still lead to VF collision. We had observed in Chapter. 4 that for the 2D case, the VFs do not collide during oscillation due to lubrication effect which results in an increase in pressure in the glottis when the VFs come very close to each other (or when (minimum VF gap)/(characteristic length scale 'L') $\ll 1$), that eventually pulls them apart. It has been pointed out in a recent review article [159] that an important feature of normal phonation for producing high frequency harmonics is the complete glottal closure. The same has been observed in an experimental study where VF collision was observed [173]. However, for computational simulation purposes a certain degree of approximation is required.

The VFs are modeled using an infinitesimal strain assumption applied in a linear elastic constitutive model framework as also provided in Luo et al. [71]. It was shown in Chapter 4, that there was very small deviation when using a linear elastic model as compared to a non-linear model for the 2D case. As such, we use the same linear elastic model for the 3D simulation presented here.

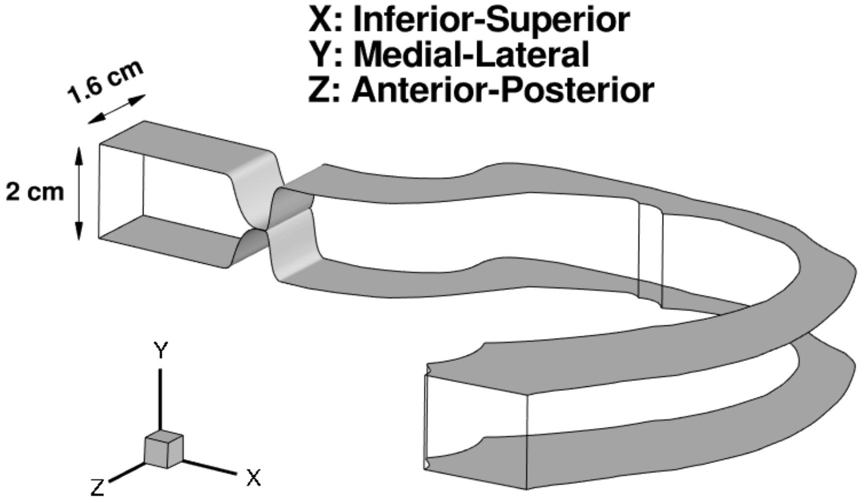

Figure 7.1: Part 1 fluid domain.

Table 7.1: Material properties of 3D VFs.

Layer	E_p (kPa)	ν_p	E_{pz} (kPa)	ν_{pz}	G_{pz} (kPa)
Cover	2	0.9	20000	0.0	10
Ligament	3.3	0.9	33000	0.0	40
Body	4	0.9	40000	0.0	20

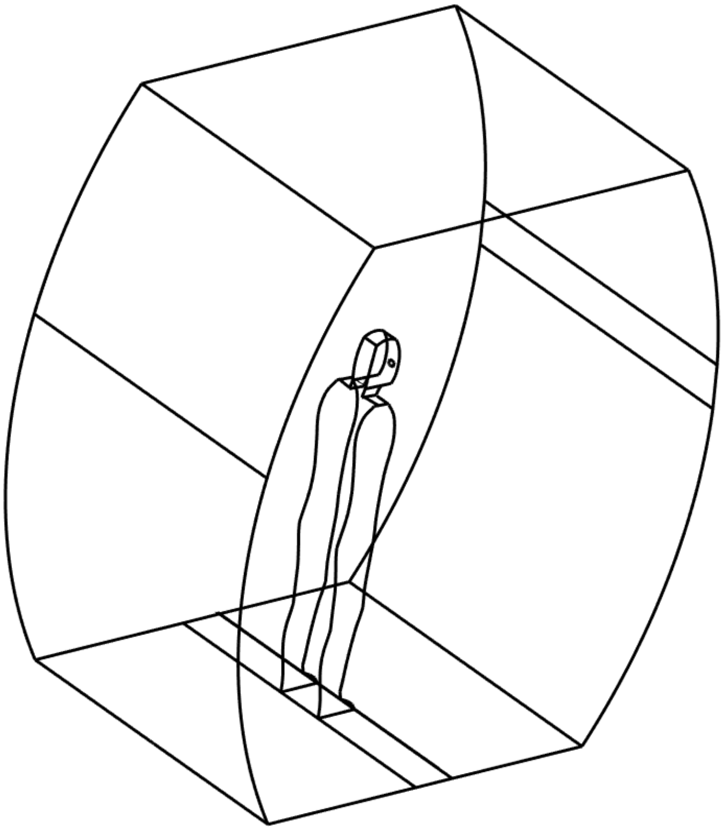

Figure 7.2: Part 2 fluid domain.

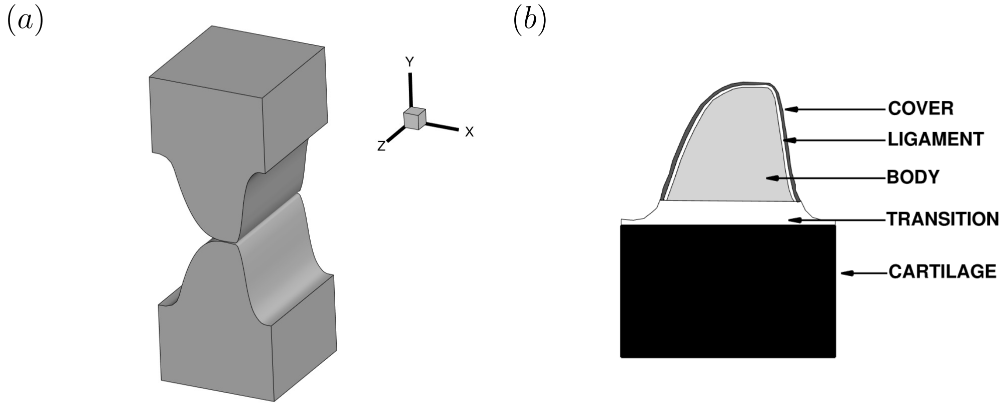

Figure 7.3: (a) 3D VF model and (b) Cross section showing the multi-layered VF.

7.2 Results

7.2.1 Glottal jet characteristics

Glottal jet in three-dimensional simulation presents an opportunity to look at aspects which are inherently missing in two-dimensions, such as jet instability leading to turbulent flow, asymmetric jet deflections along the anterior-posterior direction, etc. Figure 7.4 shows the iso-surfaces of vorticity plotted for one time period of VF oscillation. Several interesting observations follow suit. At the initial stages of the opening phase of the VFs, the jet past the glottis seem to deflect more than during other time instants. Three-dimensionality of the jet is also evident from the asymmetric deflection along the anterior-posterior direction. The length of the jet increases with time during the opening phase. As further time progresses, the jet seem to align with the stream wise direction and a flappy nature starts to appear during the deceleration phase of the jet. This instant marks the beginning of jet getting unstable and eventually detaching itself from the bulk flow. These jet characteristics have also been reported in previous three-dimensional studies [75, 107].

To provide a comparison of the current 3D glottal jet to that of the previous 2D simulation case, we plot the vorticity contours for the 3D simulation in the center-plane and compare it to the 2D simulation. In Figure 7.5 and Figure 7.6 we provide this comparison for one oscillation cycle of the VFs. To be consistent, we consider the same cycle for both the cases which here being the fifth cycle. At once it is noted that the during the initial phases of the VF opening up, the jets remain aligned to the stream wise direction for both the cases. However, as time progresses the jet deflection is seen to be more dominant for the 2D case, while the 3D case show negligible jet deflection in the center-plane. The jet deflection is related to the separation on the glottal surface, which in the 3D case is seen to occur predominantly at the glottal exit. This leads to smaller deflections for this case. The flappy nature of the jet in 3D is clearly noted here which embarks the start of instability of the jet. This wavy or flappy nature of the jet is seen to be absent for the 2D case. Instead the jet seem to detach forming smaller eddies as the jet deflection increases leading to its interaction with the nearby recirculation regions.

Next we analyze the transition to turbulence location of the supraglottal flow. It is to be pointed out that the peak jet Reynolds number defined as $Re = UW_{max}/\nu$, where U the peak flux averaged velocity, W_{max} the maximum glottal gap width and ν the kinematic viscosity of air is about 1020. This is typical Reynolds number for an adult human [75]. In a similar study [75], a much lower value of Reynolds number (= 210) was used to reduce the resolution requirements leading to a lower computational cost. In Figure 7.7, we plot the iso-surfaces of Q-criterion ($= 0.5[||\Omega||^2 - ||S||^2]$) at four different instants of time. Here Ω is the vorticity while S is the rate-of-strain tensor. A positive Q value represents vortex core where the rotation predominates over strain. The cut location in the lower wall of the vocal tract represents the approximate location of transition observed by Zheng et al [75]. It can be clearly noted that the higher but physiologically closer value of Reynolds number used in the current study leads to the transition phenomenon occurring much closer to the glottis, which was also stated in Zheng et al [75].

7.2.2 Glottal flow

Glottal waveform is an essential quantity which provides necessary information about the acoustic characteristics of the resulting flow in the far-field [75, 107, 159]. Several quantities can be obtained from the glottal waveform and compared to data from literature. Figure 7.8(a) shows a typical glottal waveform [75]. The first quantities of interest include mean and maximum flow rate given by Q_{mean} and Q_{max} respectively. Typical values of Q_{mean} measured in experiments ranges from 110 ml/s to 220 ml/s [158] while the peak flow rate is observed to lie between 200 ml/s to 580 ml/s [160]. From the current simulation results as shown in Figure 7.8(b), the mean flow rate comes out to be 130 ml/s and the peak flow rate averaged over all the cycles is 255 ml/s. These values lie within the range reported in experiments and compare very well to a similar three-dimensional simulation done by Zheng et al. [75].

The fundamental frequency obtained from the glottal waveform is 221 Hz and this value is very close to the value obtained by Zheng et al. [75], which is 243 Hz. These frequency values are relatively on the higher side, yet they lie within the normal phonation range of 60 to 260 Hz [158]. Zheng et al. [75] have attributed this to large longitudinal Young's modulus which complies

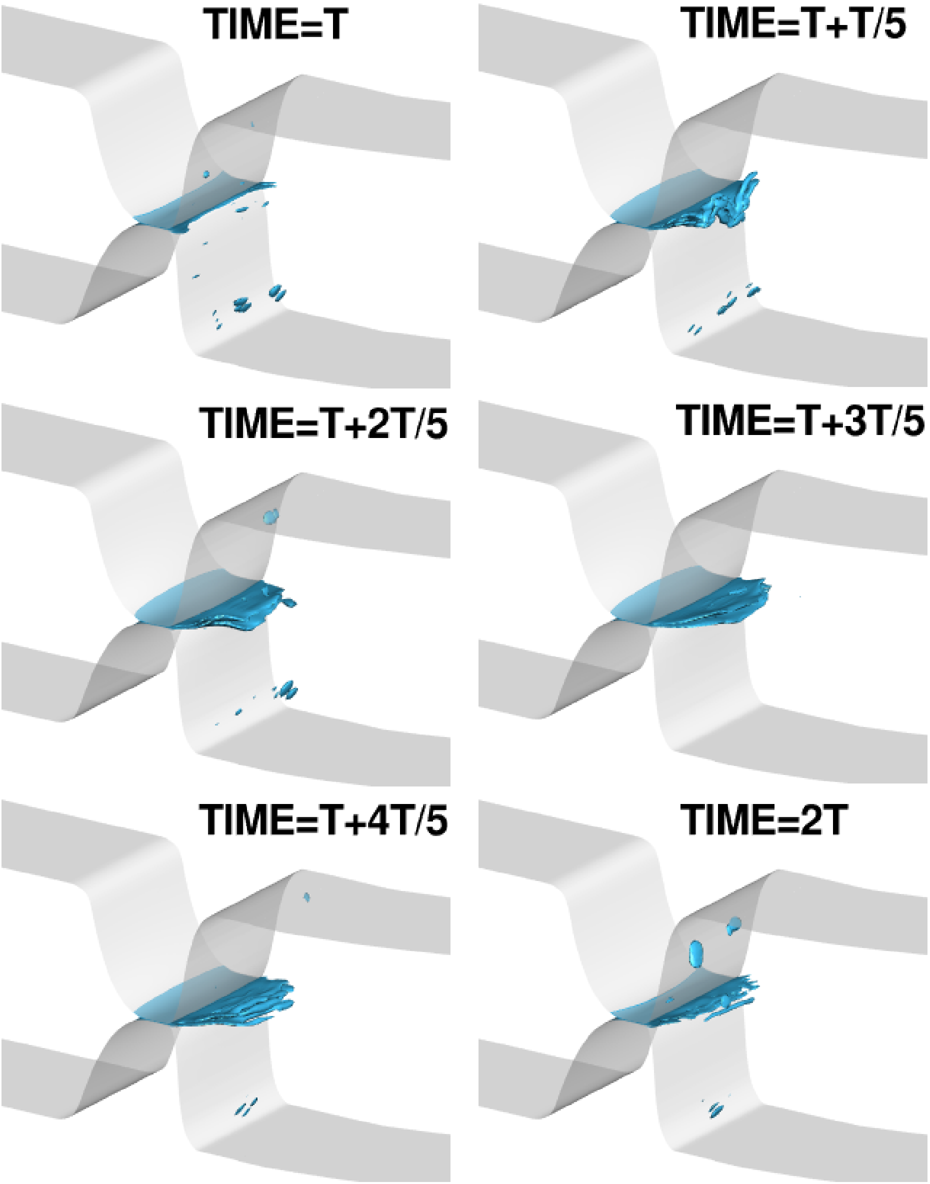

Figure 7.4: Iso-surfaces of the vorticity for one cycle of the VF oscillation.

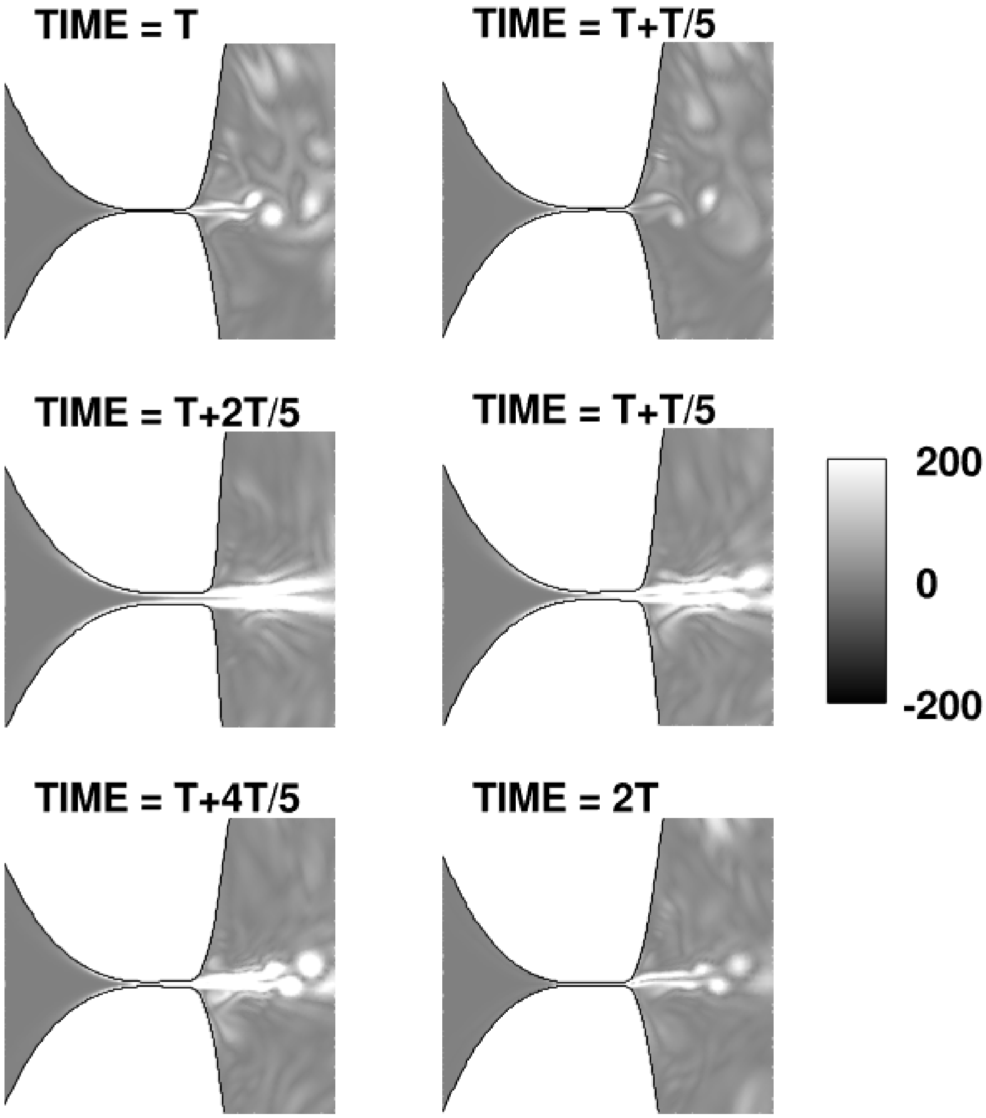

Figure 7.5: VF deformation and vorticity contours for one VF oscillation cycle for 3D in center-plane.

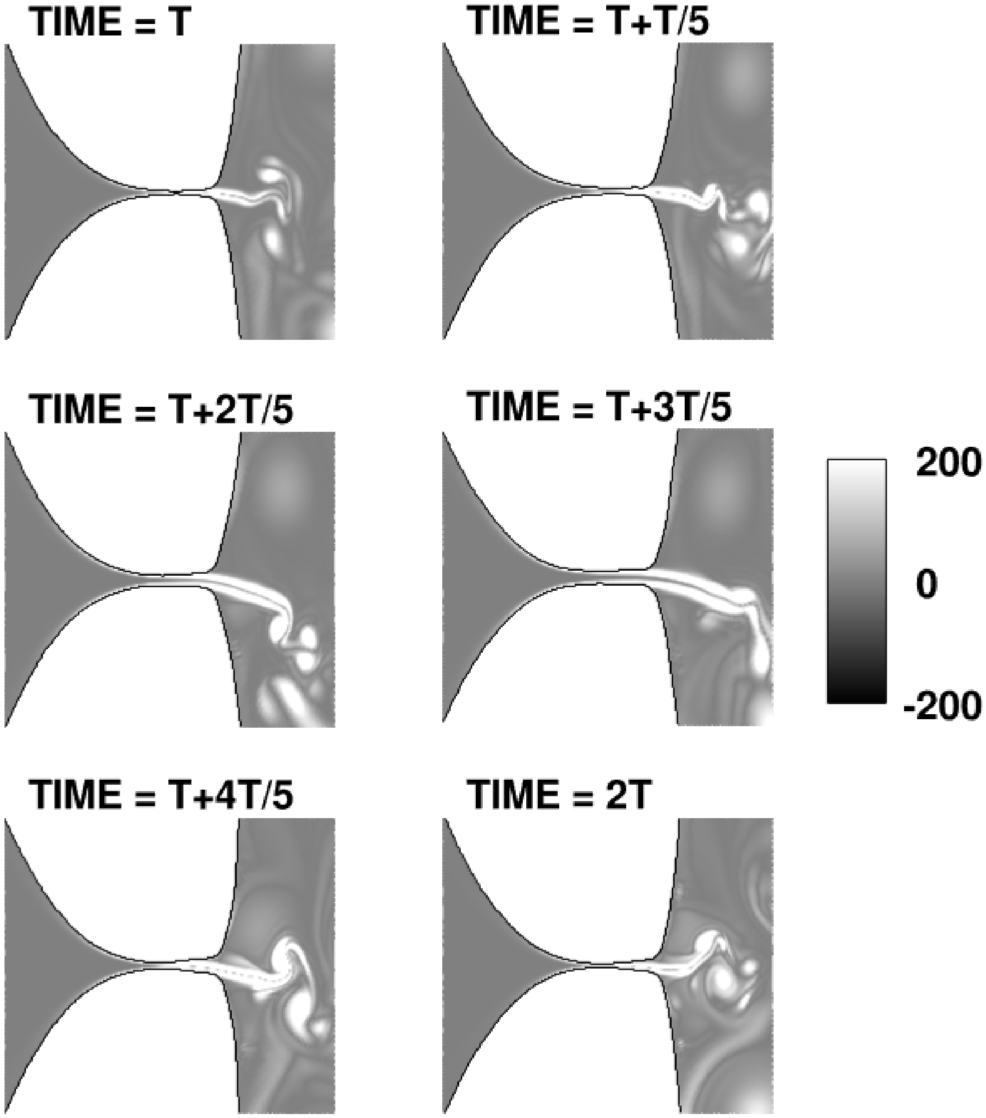

Figure 7.6: VF deformation and vorticity contours for one VF oscillation cycle for 2D case.

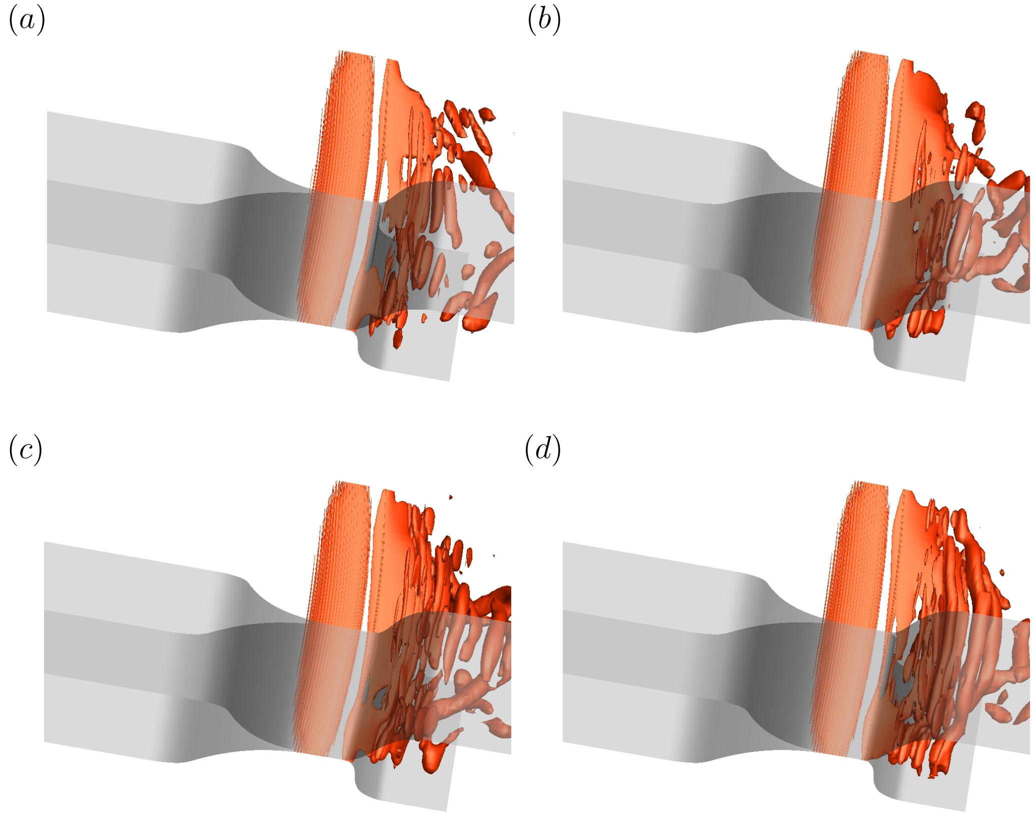

Figure 7.7: Iso-surfaces of Q-criterion (=1000 s^{-2}) at four time instants (a) t= 0.0178 s (b) t= 0.0219 s (c) t= 0.0260 s (d) t= 0.0301 s. The cut section on lower wall of vocal tract represents approximate transition location obtained from a similar study [75].

with the observations made by Rosa et al. [73] who noted an increase in phonation frequency from 160 Hz to 190 Hz when the longitudinal Young's modulus was increased from 20 kPa to 200 kPa.

As pointed out in several phonation studies [75, 159, 161] that the time-varying glottal waveform acts as a representation of sound source according to the source-filter theory and quantities like open quotient (τ_0) and skewness quotient (τ_s) play a major role in determining sound quality. As such we calculate these quantities from the current simulation and relate it to those reported in literature. From Figure 7.8(a) the vibration period is defined as T, T_p is time of increasing flow, T_n is time of decreasing flow, and T_0 is the duration of flow. The open quotient (τ_0) is defined as the ratio of the flow duration to vibration period or $\tau_0 = T_0/T$. The skewness quotient is defined as the ratio of duration of increasing flow to duration of decreasing flow or $\tau_s = T_p/T_n$. Typical values of τ_0 ranges from 0.4 to 0.75 [5]. Values of τ_0 greater than 0.75 represents breathy voice while values lower than 0.4 indicates pressed voice [5, 75]. From the current simulation we obtain a value of τ_0 to be equal to 0.64 which lies within normal phonation range and compares well to a value of 0.62 obtained from a similar simulation study [75]. The skewness quotient is an indication of the the amount of inertia of the air column and VF collapse which results in a delay in flow buildup. Typical values of τ_s range from 1.1 to 3.4 [10,71,75,162] and the value of 1.45 obtained from current simulation lies well within this range.

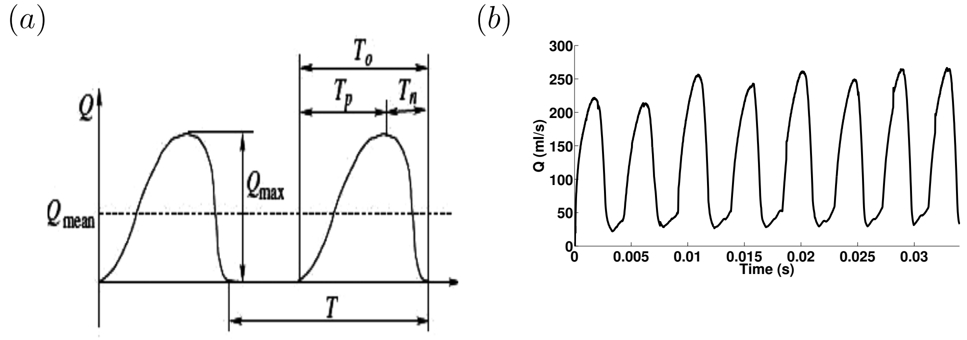

Figure 7.8: (a) Typical glottal flow rate waveform denoting the various flow quantities and (b) time variation of glottal flow rate for the current 3D simulation.

7.2.3 VF deformation

In this section we look at the qualitative as well as the quantitative behavior of the VF vibration and also compare it to the 2D simulation case. In order to do so we first go back to Figure 7.5 and Figure 7.6 where we can observe one period of oscillation of the VFs in the center-plane. We note that both the 3D as well as the 2D simulation case presents the converging-diverging shape of the VF vibration during the opening and closing phase of the cycle respectively. This is representative of the natural mucosal wave propagation during the motion of the VFs. One aspect which is different in the 3D case is the flattening of the VFs during the closing phase because of the applied kinematic constraint to prevent collision, which in the 2D case was not required as enough pressure builds up to pull them apart owing to lubrication effect.

Additionally, Figure 7.9 shows the superior view of the VF vibration for one oscillation cycle which depicts maximum opening at the center-plane during the VF opening phase with decreasing displacements as one goes away from it. As the VFs tend to reach closure this trend reverses. The applied kinematic constraint flattens the portion of the VFs which tend to overshoot it.

Figure 7.10 draws a comparison of the time variation of the left and right VF displacements from the centerline between the 3D case in center plane and the 2D simulation. As is evident from the plot, the 2D case did not require a kinematic constraint as the VFs would abduct from the minimum gap width due to lubrication effect, while for the 3D case, they tend to collapse necessitating a constraining mechanism depicted by the flat portion. The fundamental frequencies of vibration are 221 Hz and 246 Hz for the 3D and the 2D case respectively. Interestingly, For both the cases there is very slight asymmetry between the variations in the left and right VFs. The underlying asymmetry in the glottal jet and the resulting asymmetry is noted to have minimal effect on the VF vibration as has been reported in a review paper [159].

Figure 7.11 shows the time variation of glottal gap width at 5 different anterior-posterior locations. It is noted that there is no phase difference among the plots for the different locations and the VF gap width presents a symmetric variation along the longitudinal direction. This is also well

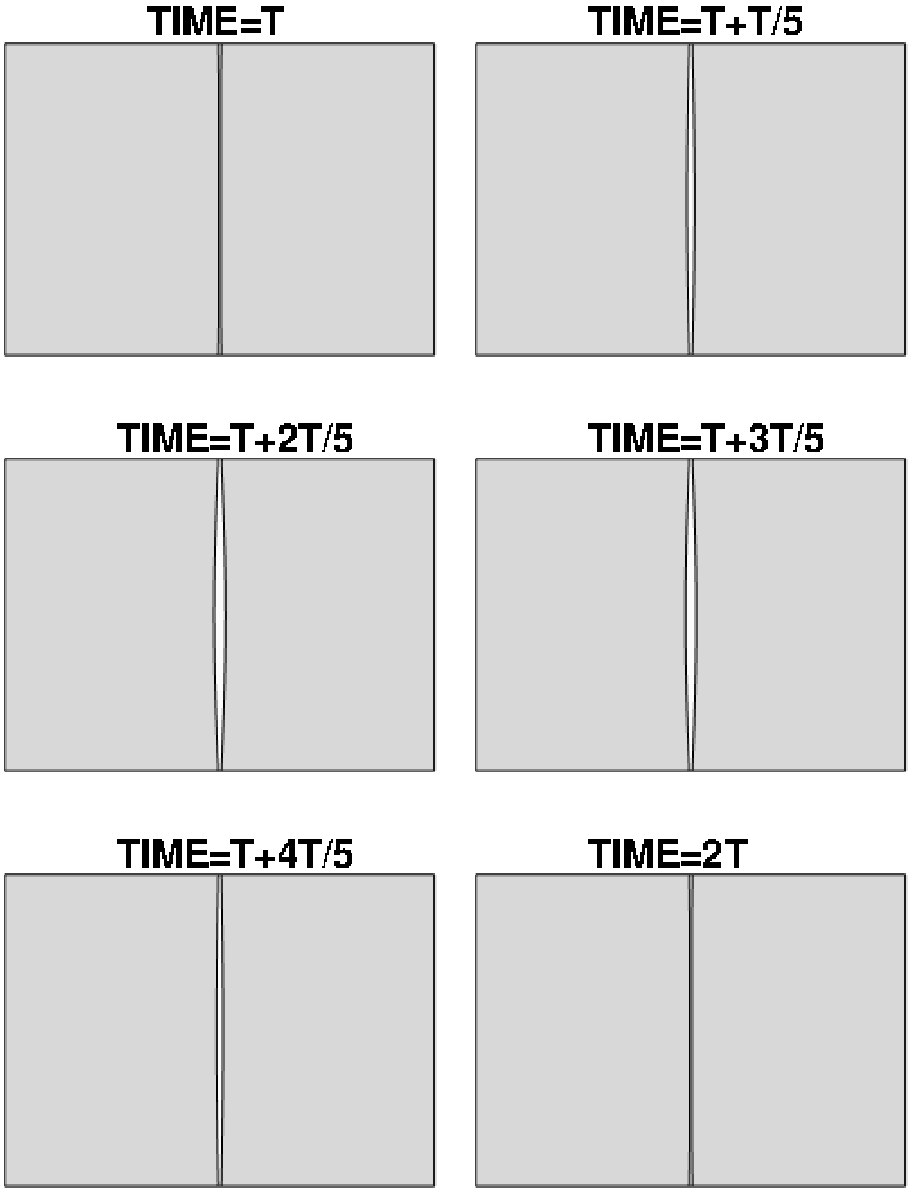

Figure 7.9: Superior view of VF vibration for one VF oscillation cycle.

captured in the superior view of the VF vibration in Figure 7.9. It is to be pointed out here that similar VF vibratory pattern is also observed in an experimental study [61] and a simulation study [75] with the same material properties and simulation setup as in the current case.

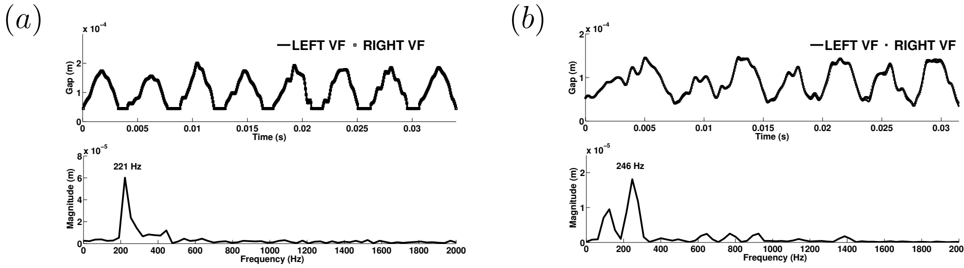

Figure 7.10: Time variation of left and right VF gap for (a) 3D case in center-plane and (b) 2D case.

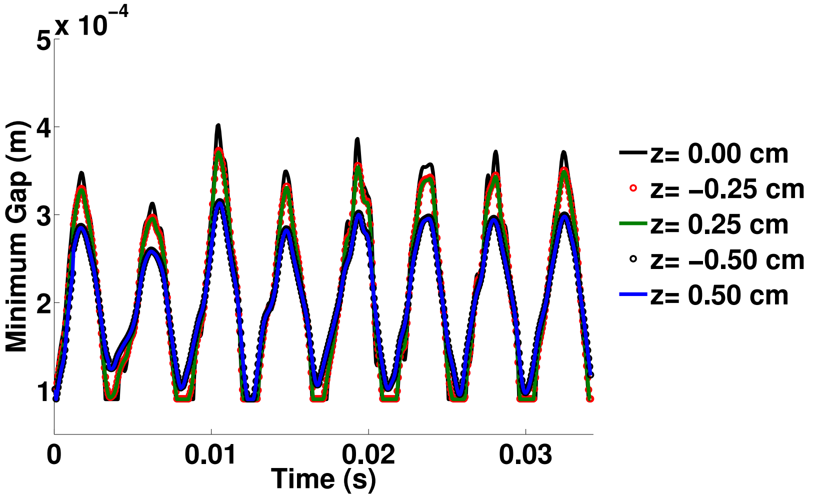

Figure 7.11: Glottal gap width variation with time at 5 different anterior-posterior directions.

7.2.4 Far-field acoustics

In this section we analyze the far-field acoustic characteristics of the current three-dimensional simulation. To reiterate, the far-field data is obtained from the second part of the simulation which uses the outflow data from the first part of the simulation as its inflow. One of the key difference between a two-dimensional and a three-dimensional simulation is the shape of the acoustic waves. While in 2D these are cylindrical waves, in 3D they are spherical. These characteristics are quite evident from the dilatation contours plotted in Figure 7.12 for the two-dimensional case and Figure 7.13 for the three-dimensional simulation. From this, one can obtain the information for the pressure fluctuation at different time instants as well as spatial locations. We look at the difference in pressure fluctuation with time for the two and three-dimensional simulations at a point 2 feet from the mouth of the speaker. Figure 7.14 shows this variation. The one thing that is of importance is the fundamental frequency of the acoustic waves in the far-field. For the three-dimensional case, this frequency aligns very well with the value obtained from near VF quantities, which is also in accordance with all the two-dimensional simulation cases performed so far. This points to the fact that the monopole source term dictated by the VF motion is the dominant term in the far-field acoustics.

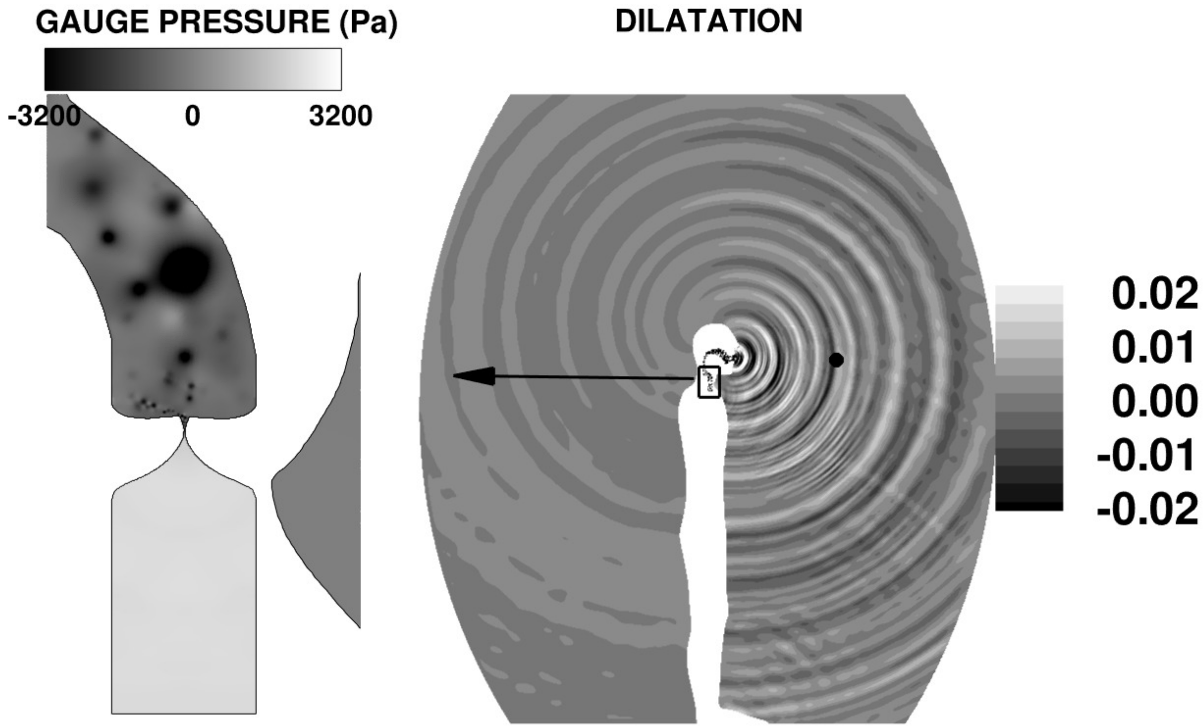

Figure 7.12: Far-field dilatation contours for a 2D adult simulation.

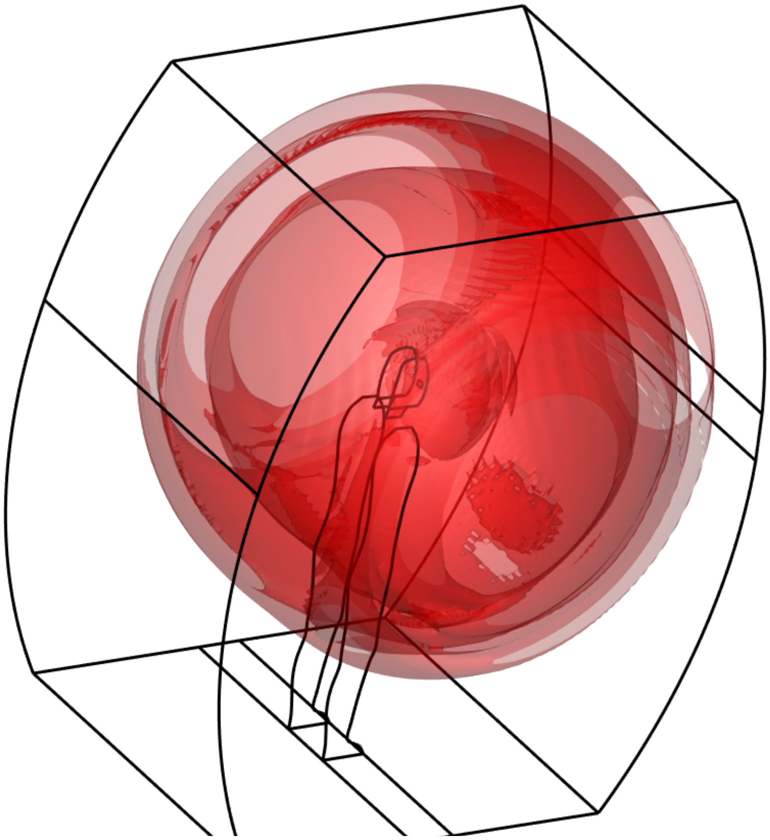

Figure 7.13: Far-field iso-surfaces of dilatation for the 3D adult simulation.

It is to be noted that the comparison between the two and three-dimensional cases is not a back-to-back one due to the variation in the material properties of the VF used for the two cases. Yet a qualitative comparison with respect to the far-field acoustic behavior is worth looking at. With this in mind we next look at far-field directivity of the acoustic wave by plotting the sound pressure levels on a circle centered at the speaker's mouth and with a radius of two feet. For the three-dimensional simulation we look at two such circles, one in the sagittal plane which aligns with the two-dimensional simulation and the other circle lies in the transverse plane which aligns with the horizontal plane. The planes are shown in Figure 7.15 for reference. Figure 7.16(a) shows the comparison between the sound pressure levels between the two dimensional simulation and the three-dimensional simulation case with sagittal plane data. The cut-section of the circle represents the points on the body and have thus been excluded. It is observed that for the two-dimensional simulation, the cylindrical wave emanating out of the speaker's mouth has to

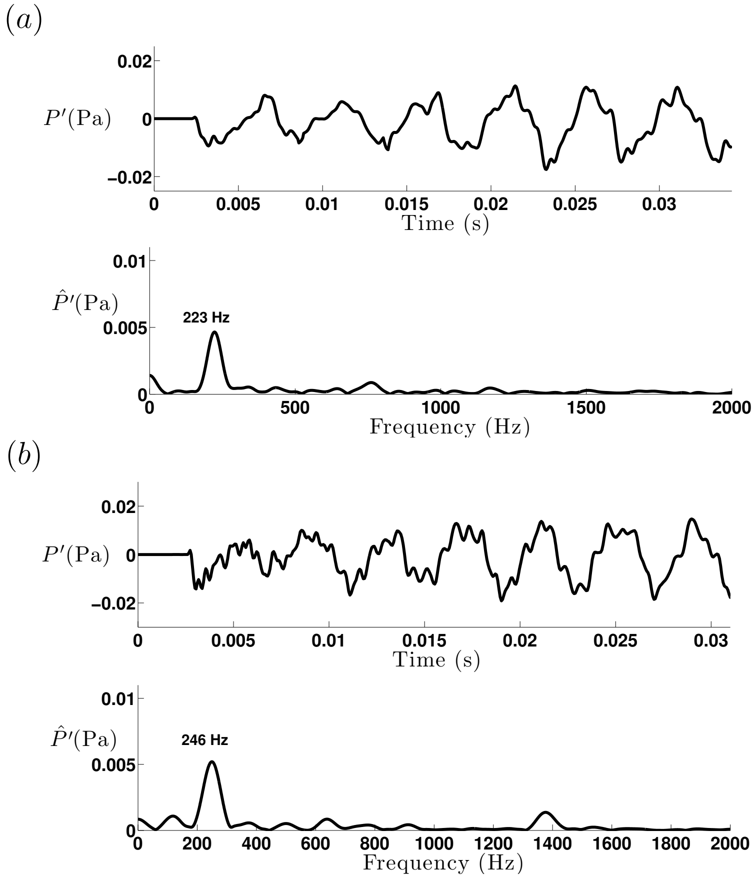

Figure 7.14: Time variation of pressure fluctuation at a point 2 feet from speaker's mouth for (a) 3D case and (b) 2D case.

overcome the head which acts as an obstacle. Thus the waves bend as they hit the head due to diffraction of sound waves. This leads to a reduced sound pressure level as one goes along the points on the circle belonging to the back of the body. Although this kind of variation is considered reasonable as far as the front portion of the body is concerned where the sound intensity is appropriately concentrated, the back is relatively much quieter, with a reduction of sound pressure level as high as 10 dB. By observation, we know that a person standing in front and at the back of us while we speak, does not perceive this big a variation. This makes the far-field acoustic variation in two-dimensions inaccurate and highlights the requirement to conduct equivalent three-dimensional simulation. This brings us to Figure 7.16(a), which shows the same variation for the three-dimensional simulation on a circle in the sagittal plane. At once we notice that the variation looks more natural with the back of the body not showing significant reduction in sound pressure levels as in the two-dimensional case. The small reduction of around 4.0 dB at the far end of the back of the body corresponding to $\theta = 255$ deg, can be attributed to a small level of diffraction presented by the head and body to the propagating spherical waves. It is to be noted that in three-dimensions the acoustic waves have an extra dimension to propagate as compared to waves in two-dimensions. Thus the resulting obstruction to the spherical waves in three-dimensions is relatively much smaller than in the two-dimensional case, leading to a more natural near symmetrical sound pressure level variation in the front and back of the body for the three-dimensional case.

Next we look at the same variation but on a circle in the transverse plane which is plotted in Figure 7.16(b). The circle in this situation does not intersect with any part of the body and as such is plotted in full. The variation is again pretty symmetric in the front and back with a maximum reduction of 3.2 dB in sound pressure level. The symmetry is also seen in the transverse direction and is again in accordance with natural expectations. Thus we note that the three-dimensional case was indeed able to capture the acoustic wave propagation much more accurately than the two-dimensional counterpart. This points to the relevance and importance of conducting three-dimensional simulation.

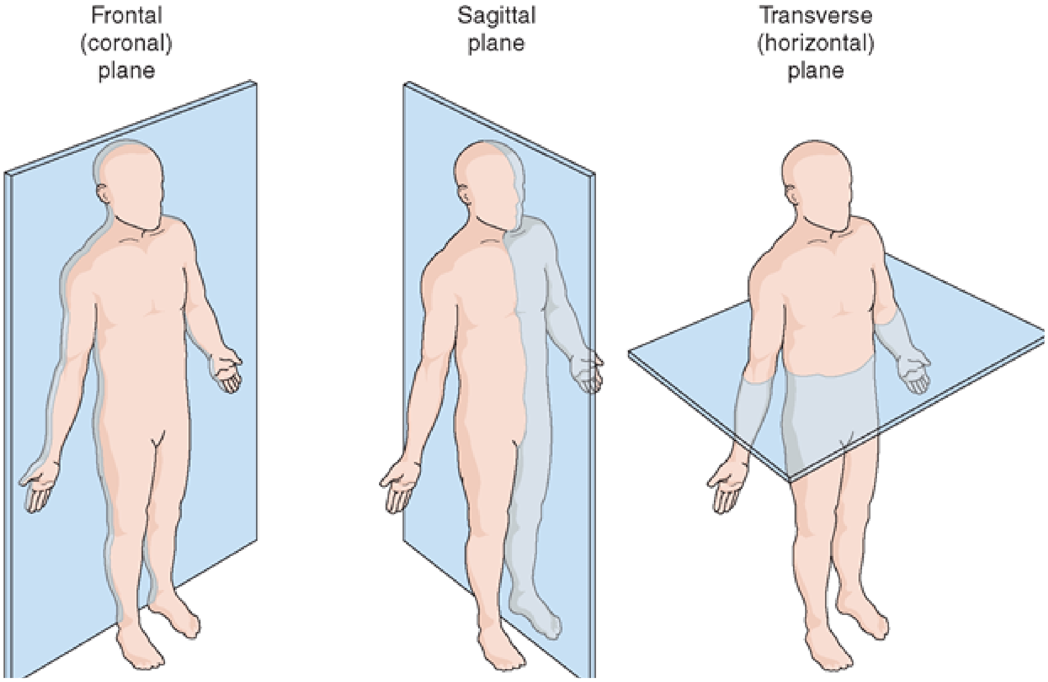

Figure 7.15: Physiological planes of the body.

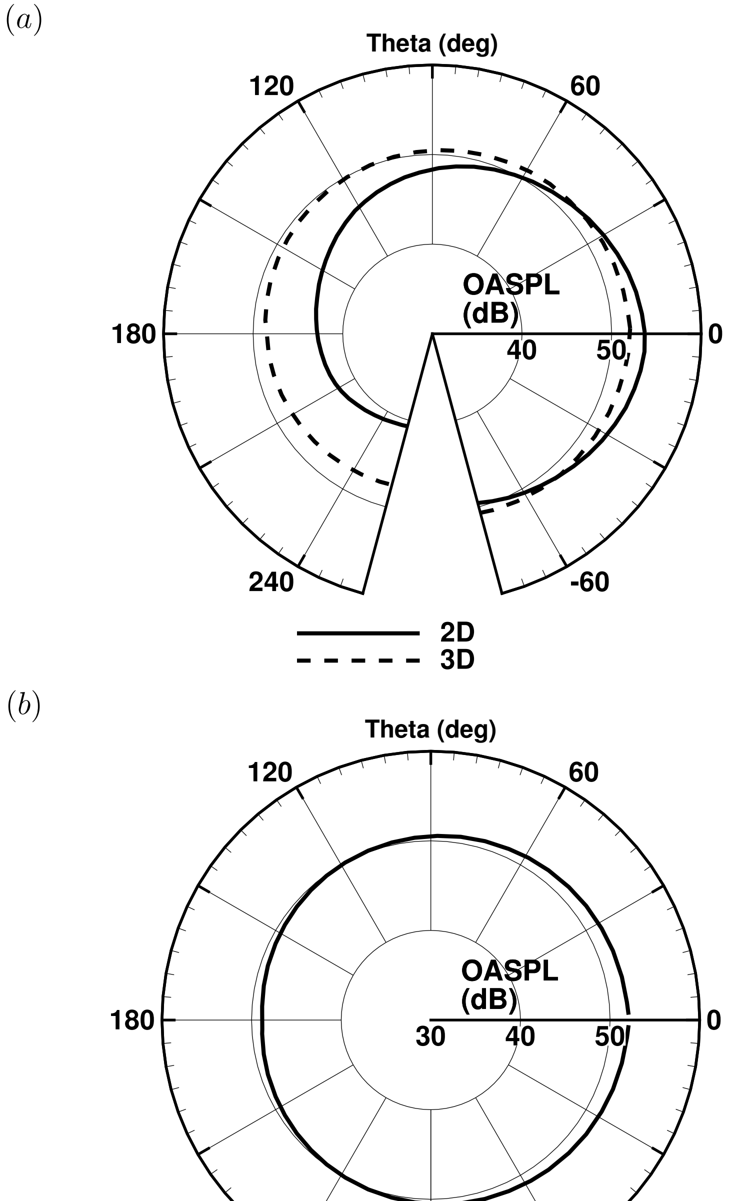

Figure 7.16: OASPL on a circle centered at mouth with a radius of 2 feet for (a) 2D vs 3D comparison in sagittal plane and (b) 3D case in transverse plane.

Chapter 8

Conclusions and Future Work

8.1 Conclusions

Phonation simulations in two dimensions involving the fluid-structure interaction between the vocal folds and the glottal flow have been performed. We set aside a number of simplifying assumptions generally made in phonation related studies, including a simplified rectangular vocal tract, single-layer structures of vocal folds, incompressible flow, vocal fold motion being imposed, and the use of a constant inflow pressure boundary condition. A new type of dynamic boundary condition based on a quasi-1D approach has been developed for the inflow to replace a constant pressure boundary condition. We verified that the vocal fold oscillation frequency as well as the periodic behavior of the resulting flow quantities is a strong function of the mean inflow pressure.

Following these improvements full-body phonation simulations were performed. Several cases have been examined with the above implementations. Here are the key takeaways.

A full body simulation of an adult and two year old child for two different Poisson's ratio ($\nu = 0.27,\ 0.47$) were performed. The presence of mucosal wave with a convergent-divergent VF opening and closing phase for the near incompressible Poisson's ratio indicates the inherent incompressible nature of the VFs as opposed to the lower value of the Poisson's ratio which resulted in a dominant lateral motion only of the VFs. The VF oscillation amplitude and frequency trend for the two Poisson's ratio complied with a parametric study [93] done for different Poisson's ratio values ranging from 0.4 to 0.5. The time-averaged velocity and streamlines plot for the adult simulation case showed the inherent asymmetry in the supraglottal flow which is consistent with literature. The effect of the vocal tract shape past the glottis was also observed by a formation of strong recirculation region near the lower wall where the shape of the vocal tract changed earlier. For the adult simulation, important quantities were obtained from plot of glottal waveform which were within phonation limits and followed the trend of Poisson's ratio change reported in another similar study [93]. Importance of considering both VFs for phonation simulations was noted by looking at glottal flow separation variation with time. The far-field acoustic characteristics followed the VF dynamics pointing to the VF mass displacement being the dominant acoustic driving parameter. An analogy was drawn between the maximum flow declination rate (MFDR) obtained from the glottal flow waveform and the acoustic intensity and the trends match clinical data. Also it is shown that the VFs do not collide during the entire time duration of the simulation as high glottal pressure develops during the VF closure due to a lubrication effect, thus not requiring any VF contact modeling. The same might not hold for a 3-D simulation where an additional degree of freedom for fluid flow might still lead to VF collision.

A VF stiffness sensitivity study was conducted for the two Poisson's ratio and the trends were analogous with the adult and child simulations. Moreover, increasing the stiffness resulted in an increased fundamental frequency and amplitude of pressure fluctuations for the far-field acoustics while decreased stiffness of the cover and ligament layers reversed the trend. Again, the dependence of vocal intensity on MFDR was shown and a clear trend was established for this study which is consistent with literature.

A study conducted to compare the phonation characteristics when the VFs are modeled using a non-linear hyper elastic model versus a linear elastic one resulted in very small differences in the VF oscillation as well as the far-field acoustic behavior. The strong similarity of the two solutions points to the fact that the small dynamic non-linearity of the VFs is not a major factor in affecting the far-field acoustics.

A study of full body simulation done in one part and two parts is presented. The results from the two scenarios did not show significant differences with the simulation in two parts having a computational advantage over the simulation done in one part. Thus, the method of running a simulation in two parts can replace the other with significant computational saving.

A comparative study between elastic only and viscoelastic based tissue model was conducted, where it was noted that the tissue viscosity had significant effect on VF oscillation amplitude and symmetry of motion resulting in reduced acoustic intensity in the far-field.

Next, two-dimensional continuum based fully coupled fluid-structure interaction simulations for VF body layer stiffness asymmetry, UVFP and medialization laryngoplasty have been studied. Phonation threshold pressure and other relevant VF and flow dynamics have been quantified and compared to available data in literature. Two different approaches to calculation of PTP have been reported. The major conclusions from the analysis is as follows.

The VF stiffness asymmetry is studied via two different series. In series 1, the left VF was kept at a lower stiffness while the right VF stiffness was varied in stiffness from low to high. In series 2, the left VF was kept at a high stiffness while the right VF varied in stiffness from high to low. For series 1, it was noted that the VFs showed increasing asymmetry with increasing differences in stiffness. The same was also observed for series 2 of the simulations. For both series 1 and 2, the fundamental frequency associated with the flow rate followed the motion of the softer VF when the difference in VF stiffness was maximum. The subglottal pressure required to initiate and sustain phonation for series 1 increases as the asymmetry is increased and is more dependent on the VF with higher stiffness. On the other hand, for series 2, the PTP values decreased with rising asymmetry. These observations have been verified against similar studies done in literature using a synthetic VF model.

The UVFP case was studied to understand the effect of one paralyzed VF on phonation characteristics. The PTP value for this case was obtained to be 1200 Pa which is in the severe phonation deficit regime as also reported through clinical studies. The flow behavior being non-uniform and an absence of a clear dominant frequency suggests flow leakage past the VFs which is characteristics of breathier voice also noticed in patients suffering from UVFP.

An attempt was made to simulate medialization laryngoplasty via inserting an implant in the paralyzed VF to adduct it towards the centerline, a method well recognized as a surgical procedure to diagnose UVFP. The flow rate began to show uniformity and clear oscillatory behavior was noticed as opposed to the UVFP case. The PTP value for this case dropped to 280 Pa which is within normal phonation limits.

A full body simulation in three-dimension was conducted using the motivation from two-dimensional simulation in two parts. The VF oscillation frequency and several quantities related to glottal flow were in good agreement to a similar study done in literature and were well within limits from both experimental and simulation data. The glottal jet exhibited wavy/flappy nature characteristic of transition to turbulence and was seen to exhibit reduced deflection when compared to the two-dimensional case. In the far-field, comparison was drawn between the two and three-dimensional simulation with respect to the sound pressure level on a circle in the sagittal plane centered at speaker's mouth. The three-dimensional case was able to capture near symmetric variation of sound in the front and back of the body, not seen for the two-dimension case which had a relatively quieter back. A directivity plot on a circle in the transverse plane for the three-dimensional case, produced similar symmetry with minimal reduction in sound pressure level as one goes from the front to back of the body. Thus the far-field acoustic variation in the three-dimensional case was able to conform to the natural propagation of sound and thus points to its significance in phonation simulations.

8.2 Future work

The complex nature of the problem presents several challenges that can form a part of the future study. The current work, has utilized the vocal tract geometry for one phoneme. Simulations can be extended to various phonemes or voice elements. Moreover, the vocal tract has been assumed to be rigid. Thus, vocal tract impedance and resonance characteristics could be applied to the current state of simulations to obtain further phonation details which are currently missing.

Three-dimensional simulations need to be conducted for all of the phonation related problems, so as to prevent significant loss of information due to lack of near-field three-dimensionality, turbulence and far-field spherical wave characteristics of sound. This is still a challenge due to the high computational cost involved, but with improved computational resources, it seems possible in the near future.

Inclusion of false vocal folds as well as articulatory elements like teeth, tongue etc can provide important information missing otherwise. This study can be extended in that direction as well.

Finally, a more detailed simulation study can be conducted for other complex pathological conditions related to the VFs and comparisons can be drawn with clinical data with the intention of bridging the gap between computational science and biomechanics.

Chapter 9

References

[1] M. S. Howe and R. S. McGowan. Aeroacoustics of [s]. *Proc. R. Soc. London A*, 461:1005–1028, 2005.

[2] National Institutes of Health. What is Voice? What is Speech? What is Language? *Published on the World Wide Web at http://www.nidcd.nih.gov/health/voice/whatisvsl.htm*, 2010.

[3] M. Hirano. Phonosurgery. Basic and clinical investigations. *Jibi to Rinsho*, 21:239–440, 1975.

[4] M. Hirano, S. Kurita and T. Nakashima. The structure of the vocal folds. In K. N. Stevens and M. Hirano (Eds.) *Vocal fold physiology*, Tokyo: Univ of Tokyo Press, 33–41, 1981.

[5] I. R. Titze. Principles of Voice Production. National Center for Voice and Speech, Iowa City, IA, 2nd edition, 2000.

[6] R. W. Chan and I. R. Titze. Dependence of phonation threshold pressure on vocal tract acoustics and vocal fold tissue mechanics *J. Acoust. Soc. Am.*,119(4):2351–2362, 2006.

[7] I. R. Titze. The physics of small amplitude oscillation of the vocal folds *J. Acoust. Soc. Am.*, 83(4):1536–1552, 1988.

[8] R. McGowan. Phonation from a continuum mechanics point of view. In J. Gauffin and B. Hammarberg (Eds.) *Vocal fold physiology: Acoustic, perceptual, and physiological aspects of voice mechanisms*, 65–72, 1991.

[9] J. L. Flanagan and L. L. Landgraf. Self-oscillating source for vocal tract synthesizers. *IEEE Trans. Audio Electroacoust.*, 16:57–64, 1968

[10] K. Ishizaka and J. L. Flanagan. Synthesis of voiced sounds from a two-mass model of the vocal cords. *Bell Syst. Tech. J.*, 51:1233-1268,1972

[11] F. Avanzini, P. Alku and M. Karjalainen. One-delayed-mass model for efficient synthesis of glottal flow. *Proc. Seventh Eur. Conf. Speech Commun. Technol*, Aalborg, Denmark, 2001.

[12] B. D. Erath, M. Zañartu, S. D. Peterson and M. W. Plesniak. Nonlinear vocal fold dynamics resulting from asymmetric fluid loading on a two-mass model of speech. *Chaos*, 21:033113,2011

[13] J. Horacek and J. G. Svec. Aeroelastic model of vocal-fold-shaped vibrating element for studying the phonation threshold. *J. Fluids Struct*, 16:931–55,2002

[14] J. Horacek and J. G. Svec. Instability boundaries of a vocal fold modeled as a flexibly supported rigid body vibrating in a channel conveying fluid. *5th Int. Symp. Fluid Struct. Interact. Aeroelast. Flow-Induc. Vib. Noise, New York:ASME*, 1043–1054,2002

[15] M. Kob. *Physical modeling of the singing voice.* PhD thesis, Univ. Technol. Aachen, 2002.

[16] J. C. Lucero. Oscillation hysteresis in a two-mass model of the vocal folds. *J. Sound Vib.*, 282:1247–1254,2005.

[17] I. Steinecke and H. Herzel. Bifurcations in an asymmetric vocal-fold model. *J. Acoust. Soc. Am.*, 97:1874–1884,1995.

[18] B. H. Story and I. R. Titze. Voice simulation with a body-cover model of the vocal folds. *J. Acoust. Soc. Am.*, 97:1249–1260,1995.

[19] Y. Zhang and J. J. Jiang. Chaotic vibrations of a vocal fold model with a unilateral polyp. *J. Acoust. Soc. Am.*, 115:1266–1269,2004.

[20] I. R. Titze. Regulating glottal airflow in phonation: application of the maximum power transfer theorem to a low dimensional phonation model. *J. Acoust. Soc. Am.*, 111:367–376,2002.

[21] A. Yang, J. Lohscheller, D. A. Berry, S. Becker and U. Eysholdt. Biomechanical modeling of the threedimensional aspects of human vocal fold dynamics. *J. Acoust. Soc. Am.*, 127:1014–1031,2010.

[22] J. F. Kaiser. Some observations on vocal tract operation from a fluid flow point of view. In I. R.Titze and R. Scherer (Eds.) *Vocal fold physiology: Biomechanics, acoustics and phonatory control*, 349–357, 1983.

[23] E. Holmberg, R. Hillman, and J. Perkell. Glottal airflow and transglottal air pressure measurements for male and female speakers in soft, normal and loud voice. *J. Acoust. Soc. Am.*, 84:511–529,1988.

[24] M. H. Krane and T. Wei. Theoretical assessment of unsteady aerodynamic effects in phonation. *J. Acoust. Soc. Am.*, 120(3):1578–1588,2006.

[25] N. Ruty, X. Pelorson, A. V. Hirtum, I. Lopez-Arteaga, A. Hirschberg. An in vitro setup to test the relevance and accuracy of low-order vocal fold models. *J. Acoust. Soc. Am.*, 121:479–490,2007.

[26] H. Teffahi. A two-mass model of the vocal cords: determination of control parameters. *Proc. Int. Conf. Multimedia Comput. Syst. ICMCS, New York:IEEE,*, 87–90, 2009.

[27] T. Wurzbacher, R. Schwarz, M. Döllinger, U. Hoppe, U. Eysholdt and J. Lohscheller. Model-based classification of nonstationary vocal fold vibrations. *J. Acoust. Soc. Am.*, 120:1012–1027,2006.

[28] M. Zañartu, L. Mongeau and G. R.Wodicka. Influence of acoustic loading on an effective single-mass model of the vocal folds. *J. Acoust. Soc. Am.*, 121:1119–1129,2007.

[29] X. Pelorson, A. Hirschberg, R. R.van Hassel, A. P. J. Wijnands and Y. Auregan. Theoretical and experimental study of quasi-steady flow separation within the glottis during phonation: application to a modified two-mass model. *J. Acoust. Soc. Am.*, 96:3416–3431,1994.

[30] B. D.Erath, S. D. Peterson, M. Zañartu, G. R.Wodicka and M. W.Plesniak. A theoretical model of the pressure field arising from asymmetric intraglottal flows applied to a two-mass model of the vocal folds. *J. Acoust. Soc. Am.*, 130:389–403,2011.

[31] C. Tao, J. J.Jiang and Y. Zhang. Simulation of vocal fold impact pressures with a self-oscillating finite-element model. *J. Acoust. Soc. Am.*, 119:3987–3994,2006.

[32] Q. Xue, R. Mittal, X. Zheng and S. Bielamowicz. A computational study of the effect of vocal-fold asymmetry on phonation. *J. Acoust. Soc. Am.*, 128:818–827,2010.

[33] N. Binh and J. Gauffin. Aerodynamic measurements in an enlarged static laryngeal model. *Tech. Rep. STLQPSR 2-3*, R. Inst. Technol., Stockholm.

[34] R. C. Scherer and C. G. Guo. Effect of vocal fold radii on pressure distributions in the glottis. *J. Acoust. Soc. Am.*, 88:S150,1990.

[35] R. C. Scherer and I. R. Titze. Pressure-flow relationships in a model of the laryngeal airway with a diverging glottis. In D. M.Bless, J. H.Abbs (Eds.) *Vocal Fold Physiology: Contemporary Research and Clinical Issues*, 179–193, 1983.

[36] R. C. Scherer, I. R. Titze and J. F. Curtis. Pressure-flow relationships in two models of the larynx having rectangular glottal shapes. *J. Acoust. Soc. Am.*, 73:668–676,1983.

[37] R. C. Scherer, D. Shinwari, K. J. DeWitt, C. Zhang, B. R. Kucinschi and A. A. Afjeh. Intraglottal pressure profiles for a symmetric and oblique glottis with a divergence angle of 10 degrees. *J. Acoust. Soc. Am.*, 109:1616–1630,2001.

[38] J. Farley and S. L. Thomson. Acquisition of detalied laryngeal flow measurements in geometrically realistic models. *J. Acoust. Soc. Am.*, 130:EL82–86,2011.

[39] R. C. Scherer, S. Torkaman, B. R. Kucinschi and A. A. Afjeh. Intraglottal pressures in a three-dimensional model with non-rectangular glottal shape. *J. Acoust. Soc. Am.*, 128:828–838,2010.

[40] A. Hirschberg, X. Pelorson, G. C.J. Hofrmans, R. R. vanHassel and A. P. J. Wijnands. Starting transient of the flow through an in-vitro model of the vocal folds. In P. J.Davis, N. H.Fletcher (Eds.) *Vocal Fold Physiology: Controlling Complexity and Chaos*, 31–46, 1996.

[41] X. Pelorson, A. Hirschberg, A. P. J. Wijnands and H. M. A. Bailliet. Description of the flow through in-vitro models of the glottis during phonation. *Act. Acust.*, 81(3):191–202, 1995.

[42] X. Pelorson, C. Vescovi, E. Castelli, A. Hirschberg, A. P. J. Wijnands and H. M. A. Bailliet. Description of the flow through in-vitro models of the glottis during phonation: application to voiced sound synthesis. *Act. Acust.*, 82:358–361, 1996.

[43] B. D. Erath and M. W. Plesniak. An investigation of bimodal jet trajectory in flow through scaled models of the human vocal folds. *Exp. Fluids.*, 40:683–696, 2006.

[44] B. D. Erath and M. W. Plesniak. An investigation of jet trajectory in flow through scaled vocal fold models with asymmetrical glottal passages. *Exp. Fluids.*, 41:735–748, 2006.

[45] B. D. Erath and M. W. Plesniak. The occurrence of the Coanda effect in pulsatile flow through static models of the human vocal folds. *J. Acoust. Soc. Am.*, 129:EL64–70, 2006.

[46] F. Alipour and R. C. Scherer. Pulsatile airflow during phonation: an excised larynx model. *J. Acoust. Soc. Am.*, 97:1241–1248, 1995.

[47] F. Alipour, V. C. Patel and R. C. Scherer. An experimental study of pulsatile flow in canine larynges. *J. Fluids Eng.*, 117:577–581, 1995.

[48] F. Alipour, V. C. Patel and R. C. Scherer. Measurement of pulsatile flow in excised larynges with hot-wire anemometry. in F. M.White Ed.*Individual Papers in Fluids Engineering*, FED-Vol. 202,1–5, 1995.

[49] S. M. Khosla, S. Murugappan, E. J. Gutmark and R. C. Scherer. Vortical flow field during phonation in an excised canine larynx model. *Ann. Otol. Rhinol. Laryngol.*, 116:217–228, 2007.

[50] S. M. Khosla, S. Murugappan, R. Lakhamaraju and E. J. Gutmark. Using particle imaging velocimetry to measure anterior-posterior velocity gradients in the excised canine larynx model. *Ann. Otol. Rhinol. Laryngol.*, 117:134–144, 2008.

[51] S. M. Khosla, S. Murugappan, R. Paniello, J. Ying and E. J. Gutmark. Role of vortices in voice production: normal versus asymmetric tension. *Laryngoscope*, 119:216–221, 2009.

[52] S. Murugappan, S. M. Khosla, K. Casper, L. Oren and E. J. Gutmark. Flow fields and acoustics in a unilateral scarred vocal fold model. *Ann. Otol. Rhinol. Laryngol.*, 118:44–50, 2009.

[53] S. L. Thomson, L. Mongeau and S. H. Frankel. Aerodynamic transfer of energy to the vocal folds. *J. Acoust. Soc. Am.*, 118:1689–1700, 2005.

[54] J. S. Drechsel and S. L. Thomson. Influence of supraglottal structures on the glottal jet exiting a two-layer synthetic, self-oscillating vocal fold model. *J. Acoust. Soc. Am.*, 123:4434–4445, 2008.

[55] J. Neubauer, Z. Zhang, R. Miraghie and D. Berry. Coherent structures of the near field flow in a self-oscillating physical model of the vocal folds. *J. Acoust. Soc. Am.*, 121:1102-1118, 2007.

[56] Z. Zhang. Characteristics of phonation onset in a two-layer vocal fold model. *J. Acoust. Soc. Am.*, 125:1091-1102, 2009.

[57] Z. Zhang, J. Neubauer and D. Berry. The influence of subglottal acoustics on laboratory models of phonation. *J. Acoust. Soc. Am.*, 120:1558-1569, 2006.

[58] Z. Zhang, J. Neubauer and D. Berry. Influence of vocal fold stiffness and acoustic loading on flow-induced vibration of a single-layer vocal fold model. *J. Sound Vib.*, 322:299-313, 2009.

[59] B. A. Pickup and S. L. Thomson. IInfluence of asymmetric stiffness on the structural and aerodynamic response of synthetic vocal fold models. *J. Biomech.*, 42:2219-2225, 2009.

[60] Z. Zhang, J. Neubauer and D. Berry. Aerodynamically and acoustically driven modes of vibration in a physical model of the vocal folds. *J. Acoust. Soc. Am.*, 120:2841-2849, 2006.

[61] S. Becker, S. Kniesburges, S. Müller, A. Delgado and G. Link. Flow-structure-acoustic interaction in a human voice model. *J. Acoust. Soc. Am.*, 125:1351–1361, 2009.

[62] Q. Xue, R. Mittal, X. Zheng and S. Bielamowicz. Sensitivity of vocal fold vibratory modes to their three-layer structure: implications for computational modeling of phonation. *J. Acoust. Soc. Am.*, 130:965–976, 2011.

[63] C. Zhang, W. Zhao, S. H. Frankel and L. Mongeau. Computational aeroacoustics of phonation, part II: effects of flow parameters and ventricular folds. *J. Acoust. Soc. Am.*, 112:2147–2154, 2002.

[64] W. Zhao, C. Zhang, S. H. Frankel and L. Mongeau. Computational aeroacoustics of phonation, part I: Computational methods and sound generation mechanisms. *J. Acoust. Soc. Am.*, 112:2134–2146, 2002.

[65] W. Zhao, S. H. Frankel and L. Mongeau. Numerical simulations of sound from confined pulsating axisymmetric jets. *AIAA J.*, 39:1868–1874, 2001.

[66] D. J. Bodony, H. Luo and R. Mittal. Prediction of sound from human vocal folds. *Bull. Am. Phys. Soc.*, 52(12), 2007.

[67] F. Alipour, D. A. Berry and I. R. Titze. A finite-element model of vocal-fold vibration. *J. Acoust. Soc. Am.*, 108(6):3003–3012, 2000.

[68] F. Alipour and R. C. Scherer. Flow separation in a computational oscillating vocal fold model. *J. Acoust. Soc. Am.*, 116(3):1710–1719, 2004.

[69] M. Larsson and B. Müller. Numerical simulation of confined pulsating jets in human phonation. *Computers and Fluids*, 38:1375–1383, 2009.

[70] J. Suh and S. H. Frankel. Numerical simulation of turbulence transition and sound radiation for flow through a rigid glottal model. *J. Acoust. Soc. Am.*, 121(6):3728–3739, 2007.

[71] H. Luo, R. Mittal, X. Zheng, S. Bielamowicz, R. J. Walsh and J. K. Hahn. An immersed-boundary method for flow-structure interaction in biological systems with application to phonation. *J. Comput. Phys.*, 227:9303–9332, 2008.

[72] H. Luo, R. Mittal and S. Bielamowicz. Analysis of flow-structure interaction in the larynx during phonation using an immersed-boundary method. *J. Acoust. Soc. Am.*, 126(2):816–824, 2009.

[73] M. de Oliveira Rosa, J. Pereira, M. Grellet and A. Alwan. A contribution to simulating a threedimensional larynx model using the finite element method. *J. Acoust. Soc. Am.*, 114(5):2893–2905, 2003.

[74] X. Zheng, Q. Xue, R. Mittal and S. Bielamowicz. A coupled sharp-interface immersed boundary-finite-element method for flow-structure interaction with application to human phonation. *J. Biomech. Eng.*, 132:111003, 2010.

[75] X. Zheng, R. Mittal, Q. Xue and S. Bielamowicz. Direct-numerical simulation of the glottal jet and vocal-fold dynamics in a three-dimensional laryngeal model. *J. Acoust. Soc. Am.*, 130:404–415, 2011.

[76] M. J. Lighthill. On sound generated aerodynamically I. General theory. *Proc. R. Soc. London A*, 211:564–587, 1952.

[77] J. E. Ffowcs Williams and D. L. Hawkings. Sound generation by turbulence and surfaces in arbitrary motion. *Proc. R. Soc. London A*, 264(151):321–342, 1969.

[78] S. Deguchi and Y. Kawahara. Simulation of human phonation with vocal nodules. *American J. of Comp. Maths.*, 1:189–201, 2011.

[79] P. Švancara, J. Horáček and V. Hrůza. FE modelling of the fluid-structure-acoustic interaction for the vocal folds self-oscillation. *In Vibration Problems ICOVP 2011, ed. by J. Náprstek et al. (Springer, Berlin, 2011)*:801–807, 2011.

[80] S. Deguchi, Y. Matsuzaki and T. Ikeda. Numerical analysis of effects of transglottal pressure change on fundamental frequency of phonation. *Annals of Otology, Rhinol. Laryngol.*, 116(2):128–134, 2007.

[81] T. Ikeda, Y. Matsuzaki and T. Aomatsu. A numerical analysis of phonation using a two-dimensional flexible channel model of the vocal folds. *J. Biomech. Eng.*, 123:571–579, 2001.

[82] M. Kaltenbacher, S. Zörner, A. Hüppe and P. Sidlof. 3d numerical simulations of human phonation. *Proc. of the 11th world congress on computational mechanics - WCCM XI*, 2014.

[83] J. Yang, X. Wang, M. Krane and L. T. Zhang. Fully-coupled aeroelastic simulation with fluid compressibility-For application to vocal fold vibration. *Comput. Methods Appl. Mech. Engrg.*, 315:584–606, 2017.

[84] R. Mittal, X. Zheng, R. Bhardwaj, J. H. Seo, Q. Xue and S. Bielamowicz. Toward A Simulation-Based Tool for the Treatment of Vocal Fold Paralysis. *Frontiers in Physiology*, 2-19:1–15, 2011.

[85] L. C. Cantor Cutiva, I. Vogel and A. Burdorf. Voice disorders in teachers and their associations with work-related factors: A systematic review. *J. Communication Disorders*,46:143–155, 2013.

[86] P. N. Carding, S. Roulstone and K. Northstone. The prevalence of childhood dysphonia: A cross-sectional study. *J. Voice*, 20:623–629, 2006.

[87] S. M. Cohen, J. Kim, N. Roy, C. Asche and M. Courey. Prevalence and causes of dysphonia in a large treatment-seeking population. *The Laryngoscope*, 122:343–348, 2012.

[88] D. A. Berry and I. R. Titze. Normal modes in a continuum model of vocal fold tissues. *J. Acoust. Soc. Am.*, 100:3345–3354, 1996.

[89] I. R. Titze and B. H. Story. Rules for controlling low-dimensional vocal fold models with muscle activation. *J. Acoust. Soc. Am.*, 112:1064–1076, 2002.

[90] S. L. Smith and S. L. Thomson. Effect of inferior surface angle on the self-oscillation of a computational vocal fold model. *J. Acoust. Soc. Am.*, 131: 4062–4075, 2012.

[91] C. Tao and J. J. Jiang. Anterior-posterior biphonation in a finite element model of vocal fold vibration. *J. Acoust. Soc. Am.*, 120:1570–1577, 2006.

[92] C. Tao and J. J. Jiang. Mechanical stress during phonation in a self-oscillating finite-element vocal fold model. *J Biomech.*, 40:2191–2198, 2007.

[93] T. E. Shurtz and S. L. Thomson. Influence of numerical model decisions on the flow-induced vibration of a computational vocal fold model. *Comput. Struct.*, 122:44–54, 2013.

[94] M. Brockmann-Bauser, D. Beyer and J. E. Bohlender. Reliable acoustic measurements in children between 5;0 and 9;11 years: Gender, age, height and weight effects on fundamental frequency, jitter and shimmer in phonations without and with controlled voice SPL. *Int. J. Pediatr. Otorhinolaryngol.*, 79:2035–2042, 2015.

[95] W. Cohen, D. M. Wynne, H. Kubba and E. McCartney. Development of a minimum protocol for assessment in the paediatric voice clinic. Part 1: Evaluating vocal function. *Logoped. Phoniatr. Vocol.*, 37(1):33–38, 2012.

[96] M. Trani, A. Ghidini, G. Bergamini and L. Presutti. Voice therapy in pediatric functional dysphonia: A prospective study. *Int. J. Pediatr. Otorhinolaryngol.*, 71:379–384, 2007.

[97] B. H. Story and K. Bunton. Formant measurement in children's speech based on spectral filtering. *Speech Commun.*, 76:93–111, 2015.

[98] Q. Xue, X. Zhang, R. Mittal and S. Bielamowicz. Computational study of effects of tension imbalance on phonation in a three-dimensional tubular larynx model. *J. Voice*, 28(4):411–419, 2014.

[99] F. B. Tian, H. Dai, H. Luo, J. F. Doyle and B. Rousseau. Fluid-structure interaction involving large deformations: 3D simulations and applications to biological systems. *J. Comp. Phys.*, 258:451–469, 2013.

[100] R. W. Chan and I. R. Titze. Viscoelastic shear properties of human vocal fold mucosa measurement methodology and empirical results. *J. Acoust. Soc. Am.*, 106(4):2008–2021, 1999.

[101] R. W. Chan and I. R. Titze. Viscoelastic shear properties of human vocal fold mucosa: Theoretical characterization based on constitutive modeling. *J. Acoust. Soc. Am.*, 107(1):565–580, 2000.

[102] R. W. Chan. Measurements of vocal fold tissue viscoelasticity: Approaching the male phonatory frequency range. *J. Acoust. Soc. Am.*, 115(6):3161–3170, 2004.

[103] S. A. Klemuk and I. R. Titze. Viscoelastic properties of three vocal-fold injectable biomaterials at low audio frequencies. *Laryngoscope*, 114:1597–1603, 2004.

[104] I. R. Titze, S. A. Klemuk and S. Gray. Methodology for rheological testing of engineered biomaterials at low audio frequencies. *J. Acoust. Soc. Am.*, 115:392–401, 2004.

[105] R. W. Chan. Estimation of viscoelastic shear properties of vocal fold tissues based on time-temperature superposition. *J. Acoust. Soc. Am.*, 110(3):1548–1561, 2001.

[106] R. W. Chan and M. L. Rodriguez. A simple-shear rheometer for linear viscoelastic characterization of vocal fold tissues at phonatory frequencies. *J. Acoust. Soc. Am.*,124(2):1207–1219, 2008.

[107] Q. Xue, R. Mittal, X. Zheng and S. A. Bielamowicz. Computational modeling of phonatory dynamics in a tubular three-dimensional model of the human larynx. *J. Acoust. Soc. Am.*, 132(3): 1602–1613, 2012.

[108] D. A. Berry, H. Reininger, F. Alipour, D. M. Bless and N. Ford. Influence of vocal fold scarring on phonation: Predictions from a finite element model. *Annals of Otology, Rhinol. Laryngol.*, 114:847–852, 2005.

[109] D. G. Hanson and J. J. Jiang. Diagnosis and management of chronic laryngitis associated with reflux. *The American Journal of Medicine.*, 108(4A): 112S–119S, 2000.

[110] S. L. Thibeault, S. D. Gray, D. M. Bless, R. W. Chan and C. N. Ford. Histologic and rheologic characterization of vocal fold scarring. *J. Voice.*, 16(1): 96–104, 2002.

[111] T. Havas, D. Lowinger and J. Priestley. Unilateral vocal fold paralysis: causes, options and outcomes. *The Australian and New Zealand journal of surgery.*, 69(7): 509–513, 1999.

[112] T. Kim, K. Goodhart, J. E. Aviv, R. L. Sacco, D. Beverly, S. Kaplan and L. G. Close. FEESST: A new bedside endoscopic test of the motor and sensory components of swallowing. *Annals of Otology, Rhinol. Laryngol.*, 107: 378–387, 1998.

[113] D. A. Berry, Z. Zhang and J. Neubauer. Mechanisms of irregular vibration in a physical model of the vocal folds. *J. Acoust. Soc. Am.*, 120(3): 36–42, 2006.

[114] Z. Zhang, J. Kreiman and B. R. Gerratt. Acoustic and perceptual effects of changes in body layer stiffness in symmetric and asymmetric vocal fold models. *J. Acoust. Soc. Am.*, 133(1): 453–462, 2012.

[115] Z. Zhang and T. H. Luu. Asymmetric vibration in a two-layer vocal fold model with left-right stiffness asymmetry: Experiment and simulation. *J. Acoust. Soc. Am.*, 132(3):1626–1636, 2012.

[116] M. Hirano. Morphological structure of the vocal cord as a vibrator and its variations. *Folia Phoniatr (Basel).*, 26(2): 89–94, 1974.

[117] S. Fex and D. Elmqvist. Endemic recurrent laryngeal nerve paresis. *Acta oto-laryngologica.*, 75: 368–369, 1973.

[118] S. Lowell and B. H. Story. Simulated effects of cricothyroid and thyroarytenoid muscle activation on adult-male vocal fold vibration. *J. Acoust. Soc. Am.*, 120: 386–397, 2006.

[119] N. Isshiki, M. Tanabe, K. Ishizaka and D. Broad. Clinical significance of asymmetrical vocal cord tension. *Annals of Otology, Rhinol. Laryngol.*, 86: 58–66, 1977.

[120] J. A. Sercarz, G. S. Berke, M. Ye, B. R. Gerratt and M. Natividad. Videostroboscopy of human vocal fold paralysis. *Annals of Otology, Rhinol. Laryngol.*, 101: 567–577, 1992.

[121] D. M. Moore, G. S. Berke, D. G. Hanson and P. H. Ward. Videostroboscopy of the canine larynx: The effects of asymmetric laryngeal tension. *Laryngoscope.*, 97: 543–553, 1987.

[122] M. E. Smith, G. S. Berke, B. R. Gerratt, J. Kreiman. Laryngeal paralyses: Theoretical considerations and effects on laryngeal vibration. *J. Speech Language and Hearing Research.*, 35: 545–554, 1992.

[123] G. S. Berke and B. R. Gerratt. Laryngeal biomechanics: An overview of mucosal wave mechanics. *J. Voice.*, 7: 123–128, 1993.

[124] J. E. Aviv, T. Kim, J. E. Thomson, S. Sunshine, S. Kaplan and L. G. Close. Fiberoptic endoscopic evaluation of swallowing with sensory testing (FEESST) in healthy controls. *Dysphagia*, 13(2): 87–92, 1998.

[125] J. E. Aviv, J. H. Martin, M. S. Keen, M. Debell and A. Blitzer. Air pulse quantification of supraglottic and pharyngeal sensation: a new technique. *Annals of Otology, Rhinol. Laryngol.*, 102(10): 777–780, 1993.

[126] P. Bhabu, C. Poletto, E. Mann, S. Bielamowicz and C. L. Ludlow. Thyroarytenoid muscle responses to air pressure stimulation of the laryngeal mucosa in humans. *Annals of Otology, Rhinol. Laryngol.*, 112(10): 834–840, 2003.

[127] M. Vinokur. Conservation equations of gasdynamics in curvilinear coordinate systems. *J. Comp. Phys.*, 14:105–125, 1974.

[128] B. Strand. Summation by parts for finite difference approximations for d/dx. *J. Comp. Phys.*, 110:47–67, 1994.

[129] K. Mattsson, M. Svärd, and J. Nordström. Stable and accurate artificial dissipation. *J. Sci. Comput.*, 21(1):57–79, 2004.

[130] M. H. Carpenter, D. Gottlieb, and S. Abarbenel. Time-stable boundary conditions for finite difference schemes involving hyperbolic systems: Methodology and application for high-order compact schemes. *J. Comp. Phys.*, 111:220–236, 1994.

[131] M. Svärd, M. H. Carpenter, and J. Nordström. A stable high-order finite difference scheme for the compressible navier-stokes equations, far-field boundary conditions. *J. Comp. Phys.*, 225:1020–1038, 2007.

[132] M. Svärd and J. Nordström. A stable high-order finite difference scheme for the compressible Navier-Stokes equations: No-slip wall boundary conditions. *J. Comp. Phys.*, 227:4805–4824, 2008.

[133] J. Nordström, J. Gong, E. Van der Weide, and M. Svärd. A stable and conservative high order multi-block method for the compressible navier-stokes equations. *J. Comp. Phys.*, 228:9020–9035, 2009.

[134] D. J. Bodony. Accuracy of the simultaneous-approximation-term boundary condition for time-dependent problems. *J. Sci. Comput.*, 43(1):118–133, 2010.

[135] T. H. Pulliam and D. S. Chaussee. A diagonal form of an an implicit approximate-factorization algorithm. *J. Comp. Phys.*, 43:357–372, 1981.

[136] D. J. Bodony. Analysis of sponge zones for computational fluid mechanics. *J. Comp. Phys.*, 212:681–702, 2006.

[137] S. K. Lele. Compact finite difference schemes with spectral-like resolution. *J. Comp. Phys.*, 103:16–42, 1992.

[138] M. Svärd and J. Nordström. On the order of accuracy for difference approximations of initial-boundary value problems. *J. Comp. Phys.*, 218:333–352, 2006.

[139] M. R. J. Charest, C. P. T. Groth and P. Q. Gauthier. High-order CENO finite-volume scheme for low-speed viscous flows on three-dimensional unstructured mesh. *In Seventh International Conference on Computational Fluid Dynamics (ICCFD7)*,1002, 2012.

[140] J. Kim, D. J. Bodony, and J. B. Freund. LES investigation of a mach 1.3 jet with and without plasma actuators. AIAA Paper 2009-0290, Presented at the 47th Aerospace Sciences Meeting & Exhibit, January 2009.

[141] D. J. Bodony. Heating effects on the structure of noise sources of high-speed jets. AIAA Paper 2009-0291, Presented at the 47th Aerospace Sciences Meeting & Exhibit, Orlando, Florida, Jan. 5-8, 2009.

[142] M. Sucheendran, D. J. Bodony, and P. H. Geubelle. Structural-acoustic interaction of a cavity-backed, clamped, elastic plate with sound in a duct. *Bull. Am. Phys. Soc.*, 54(19), 2009.

[143] G. Zagaris, D. J. Bodony, M. Brandyberry, M. T. Campbell, E. G. Shaffer, and J. B. Freund. A collision detection approach to chimera grid assembly for high fidelity simulations of turbofan noise. In *48th AIAA Aerospace Sciences Meeting*, number 2010–836. AIAA, AIAA, January 2010.

[144] J. Kim, M. Natarajan, D. J. Bodony, and J. B. Freund. A high-order, overset mesh algorithm for adjoint-based optimization for aeroacoustics control. AIAA Paper 2010-3818, Presented at the 16th AIAA/CEAS Aeroacoustics Conference, June 2010.

[145] D. J. Bodony, G. Zagaris, A. Reichert, and Q. Zhang. Aeroacoustic predictions in complex geometries. In R. J. Astley and G. Gabard, editors, *IUTAM Symposium on Computational Aero-Acoustics for Aircraft Noise Prediction*, volume 6, pages 234–243. Procedia Engineering, 2010.

[146] S. P. Spekreijse, B. B. Prananta, and J. C. Kok. A simple, robust and fast algorithm to compute deformations of multi-block structured grids. Report TP-2002-105, National Aerospace Laboratory NLR, February 2002.

[147] J. F. Thompson, F. C. Thames and C. W. Mastin. Automatic Numerical Generation of Body-fitted Curvilinear Coordinate System for Field Containing any Number of Arbitrary Two-Dimensional Bodies. *J. Comput. Phys.*, 15:299-319, 1974.

[148] C. Ostoich. *Aerothermal and aeroelastic response prediction of aerospace structures in high-speed flows using direct numerical simulation.* PhD thesis, Univ. Illinois at Urbana-Champaign, 2013.

[149] L. Vujošević and V. A. Lubarda. Finite-strain thermoelasticity based on multiplicative decomposition of deformation gradient. *Theoretical and applied mechanics*, (28-29), 2002.

[150] J. Bonet and R. D. Wood. *Nonlinear continuum mechanics for finite element analysis.* Cambridge university press, 1997.

[151] K. R. Srinivasan. *Thermomechanical meso-scale modeling of combustion of heterogeneous solid propellants.* PhD thesis, University of Illinois at Urbana-Champaign, 2008.

[152] I. Doghri. *Mechanics of deformable solids: linear, nonlinear, analytical, and computational aspects.* Springer Verlag, 2000.

[153] G. A. Holzapfel. On large strain viscoelasticity: continuum formulation and finite element applications to elastomeric structures. *Int. J. Num. Methods. Engineering*, 39:3903-3926, 1996.

[154] M. B. Giles. Stability analysis of numerical interface conditions in fluid-structure thermal analysis. *Int. J. Num. Methods. Fluids*, 25(8):421–436, 1997.

[155] R. Mittal, B. D. Erath and M. W. Plesniak. Fluid dynamics of human phonation and speech. *Annu. Rev. Fluid Mech.*, 45:437–467, 2013.

[156] J. H. Seo and R. Mittal. A high-order immersed boundary method for acoustic wave scattering and low-Mach number flow-induced sound in complex geometries. *J. Comput. Phys..*, 230:1000–1019, 2011.

[157] X. Zheng, R. Mittal and S. Bielamowicz. A computational study of asymmetric glottal jet deflection during phonation. *J. Acoust. Soc. Am.*, 129:2133–2143, 2011.

[158] W. R. Zemlin. Speech and hearing science: anatomy and physiology. *Prentice Hall. Vol. 3rd edition. Englewood Cliffs, NJ: Prentice Hall*, 1988.

[159] Z. Zhang. Mechanics of human voice production and control. *J. Acoust. Soc. Am.*, 140(4):2614–2635, 2016.

[160] S. Hertegard, J. Gauffin and I. Karlsson. Physiological correlates of the inversrsed filtered flow waveform. *J. Voice*, 6(3):224–234, 1992.

[161] G. Fant. Theory of Speech Production. *Mouton, The Hague*, 140(4):p. 328, 1960.

[162] M. D. Lamar, Y. Qi. and J. Xin. Modeling vocal fold motion with a hydrodynamic semicontinuum model. *J. Acoust. Soc. Am.*, 114(1):455–463, 2003.

[163] I. R. Titze. Theoretical analysis of maximum flow declination rate versus maximum area declination rate in phonation. *J. Speech, Language and Hearing Res.*, 49:439–447, 2006.

[164] C. M. Sapienza and E. T. Stathopoulos Comparison of maximum flow declination rate: Children versus adults. *J. Voice*, 8(3):240–247, 1994.

[165] M. Hirano, S. Kurita and T. Nakashima. Growth, development and aging of human vocal folds. In D. M. Bless and J. H. Abbs (Eds.) *Vocal fold physiology: contemporary research and clinical issues*, San Diego College Hill Press, 22–43, 1983.

[166] H. K. Vorperian, R. D. Kent, M. J. Lindstrom, C. M. Kalina, L. R. Gentry and B. S. Yandell. Development of vocal tract length during early childhood: A magnetic resonance imaging study. *J. Acoust. Soc. Am.*, 117(1):338–350, 2005.

[167] M. Larsson and B. Müller. Numerical simulation of fluid-structure interaction in human phonation: application. In G. Kreiss et al. (Eds.)*Numerical Mathematics and Advanced Applications*, Springer-Verlag Berlin Heidelberg, 571–578, 2010.

[168] A. Kosik. Numerical simulation of interaction of fluid flow and an elastic body. *WDS'11 Proc. Contributed Papers*, 1:61–66, 2011.

[169] D. Henry. Materials and coatings for medical devices: cardiovascular. *ASM International, Ohio, USA.*, 297–303, 2009.

[170] J. C. Lucero and L. L. Koenig. On the relation between the phonation threshold lung pressure and the oscillation frequency of the vocal folds. *J. Acoust. Soc. Am.*, 121(6):3280–3283, 2007.

[171] J. M. Lilly and S. C. Olhede. Higher-order properties of analytic wavelets. *IEEE Transactions on Signal Processing.*, 57(1): 146–160, 2009.

[172] G. Bianchi and R. Sorrentino. Electronic filter simulation and design. *McGraw-Hill Professional.*, 17–20, 2007.

[173] Y. Xuan and Z. Zhang. Influence of embedded fibers and an epithelium layer on glottal closure pattern in a physical vocal fold model. *J. Speech Lang. Hear. Res.*, 57:416–425, 2014.

[174] D. D. Cook, E. Nauman. and L. Mongeau. Reducing the number of vocal fold mechanical tissue properties: Evaluation of the incompressibility and planar displacement assumptions. *J. Acoust. Soc. Am.*, 124(6):3888–3896, 2008.

Appendix A

Additional Thermomechanical Formulation Details

A.1 Elasticity tensor, $\mathcal{A}$

The elasticity tensor, $\mathcal{A}$, is defined as $\mathcal{A} = \partial \boldsymbol{P}/\partial \boldsymbol{F}$. Given the result in appendix 3.2.1, the elasticity tensor relating changes in the first Piola-Kirchhoff elasticity tensor to changes in the deformation gradient can be found as

$$\begin{aligned} \mathcal{A}_{KiLj} &= \frac{\partial}{\partial F_{jL}} \left(F_{iP} S_{KP} \right) = \frac{\partial}{\partial F_{jL}} \left(2 F_{iP} \frac{\partial W}{\partial C_{KP}} \right) \\ &= 2\delta_{ij}\delta_{LP} \frac{\partial W}{\partial C_{KP}} + 2F_{iP} \frac{\partial^2 W}{\partial C_{KP} \partial C_{MN}} \frac{\partial C_{MN}}{\partial F_{jL}} \\ &= \delta_{ij} S_{KL} + 4 F_{iP} F_{jM} \frac{\partial^2 W}{\partial C_{KP} \partial C_{ML}} \\ &= \delta_{ij} S_{KL} + F_{iP} F_{jM} \mathcal{C}_{KPML}, \end{aligned} \tag{A.1}$$

where $\mathcal{C}_{KPML} = 4\frac{\partial^2 \hat{W}}{\partial C_{KP} \partial C_{ML}}$ is the elasticity tensor relating changes in the Green-Lagrange strain tensor, $\boldsymbol{E}$, to the second Piola-Kirchhoff stress tensor, $\boldsymbol{S}$. This result is valid for any isotropic material. For the St. Venant-Kirchhoff model, it is known that

$$\mathcal{C}_{KPML} = \lambda \delta_{KP} \delta_{ML} + \mu (\delta_{KM} \delta_{PL} + \delta_{KL} \delta_{PM}),$$

where λ and μ are the first and second Lamé parameters, respectively. For the modified Neo-Hookean model, following the derivation steps summarized in Doghri [152], the elasticity tensor is found to be

$$\mathcal{C}_{KPML} = \Gamma_1 C^{-1}_{KP} C^{-1}_{ML} + \Gamma_2 \left(C^{-1}_{KP} \delta_{ML} + \delta_{KP} C^{-1}_{ML} \right) + \frac{1}{2} \Gamma_8 \left(C^{-1}_{KM} C^{-1}_{PL} + C^{-1}_{KL} C^{-1}_{PM} \right),$$

where

$$\Gamma_1 = \frac{2}{9} G \,\mathrm{Tr}(\boldsymbol{C}) J^{-2/3} + K(2J^2 - J),$$

$$\Gamma_2 = -\frac{2}{3} G \, J^{-2/3},$$

and

$$\Gamma_8 = \frac{2}{3} G \, \mathrm{Tr}(\boldsymbol{C}) J^{-2/3} - 2K(J^2 - J).$$

A.2 External load jacobian, $\mathcal{B}$

The term $\mathcal{B}$ entering Eq. (3.14) is

$$\begin{aligned}
\mathcal{B} &= \frac{\partial}{\partial^e \boldsymbol{F}} \left(\boldsymbol{t} \, {}^e J \sqrt{\boldsymbol{N} \cdot \boldsymbol{C}^{-1} \boldsymbol{N}} \right) \\
&= \frac{\partial \boldsymbol{t}}{\partial^e \boldsymbol{F}} \left({}^e J \sqrt{\boldsymbol{N} \cdot \boldsymbol{C}^{-1} \boldsymbol{N}} \right) + \boldsymbol{t} \frac{\partial}{\partial^e \boldsymbol{F}} \left({}^e J \sqrt{\boldsymbol{N} \cdot \boldsymbol{C}^{-1} \boldsymbol{N}} \right) \\
&= \mathcal{B}_{\boldsymbol{t}} \left({}^e J \sqrt{\boldsymbol{N} \cdot \boldsymbol{C}^{-1} \boldsymbol{N}} \right) + \boldsymbol{t} \, \mathcal{B}_{da},
\end{aligned} \tag{A.2}$$

where $\mathcal{B}_{\boldsymbol{t}}$ and $\mathcal{B}_{da}$ are the Jacobians associated with the change in traction and surface, respectively, This term is derived as follows. The superscript e on the deformation gradient $\boldsymbol{F}$ and Jacobian, J, will be left off for brevity.

$$\begin{aligned}
\mathcal{B}_{da,gG} &= \frac{\partial}{\partial F_{gG}} \left(J \sqrt{\boldsymbol{N} \cdot \boldsymbol{C}^{-1} \boldsymbol{N}} \right) = \frac{\partial J}{\partial F_{gG}} \sqrt{\boldsymbol{N} \cdot \boldsymbol{C}^{-1} \boldsymbol{N}} + J \frac{\partial}{\partial F_{gG}} \left(\sqrt{\boldsymbol{N} \cdot \boldsymbol{C}^{-1} \boldsymbol{N}} \right) \\
&= J F_{gG}^{-1} \sqrt{\boldsymbol{N} \cdot \boldsymbol{C}^{-1} \boldsymbol{N}} + \frac{J}{2} \left(\boldsymbol{N} \cdot \boldsymbol{C}^{-1} \boldsymbol{N} \right)^{-1/2} \frac{\partial}{\partial F_{gG}} \left(\boldsymbol{N} \cdot \boldsymbol{C}^{-1} \boldsymbol{N} \right) \\
&= J \left[F_{gG}^{-1} \sqrt{\boldsymbol{N} \cdot \boldsymbol{C}^{-1} \boldsymbol{N}} + \frac{1}{2} \left(\boldsymbol{N} \cdot \boldsymbol{C}^{-1} \boldsymbol{N} \right)^{-1/2} N_I \frac{\partial C_{IJ}^{-1}}{\partial F_{gG}} N_J \right] \\
&= J \left[F_{gG}^{-1} \sqrt{\boldsymbol{N} \cdot \boldsymbol{C}^{-1} \boldsymbol{N}} + \frac{1}{2} \left(\boldsymbol{N} \cdot \boldsymbol{C}^{-1} \boldsymbol{N} \right)^{-1/2} N_I \frac{\partial}{\partial F_{gG}} \left(F_{Ik}^{-1} F_{Jk}^{-1} \right) N_J \right] \\
&= J \Big[F_{gG}^{-1} \sqrt{\boldsymbol{N} \cdot \boldsymbol{C}^{-1} \boldsymbol{N}} \\
&\qquad + \frac{1}{2} \left(\boldsymbol{N} \cdot \boldsymbol{C}^{-1} \boldsymbol{N} \right)^{-1/2} N_I \left(F_{Ik}^{-1} \frac{\partial F_{Jk}^{-1}}{\partial F_{gG}} + F_{Jk}^{-1} \frac{\partial F_{Ik}^{-1}}{\partial F_{gG}} \right) N_J \Big]
\end{aligned} \tag{A.3}$$

$$\begin{aligned}
&= J \Big[F_{gG}^{-1} \sqrt{\boldsymbol{N} \cdot \boldsymbol{C}^{-1} \boldsymbol{N}} \\
&\qquad + \frac{1}{2} \left(\boldsymbol{N} \cdot \boldsymbol{C}^{-1} \boldsymbol{N} \right)^{-1/2} N_I \left(F_{Ik}^{-1} F_{Jg}^{-1} F_{Gk}^{-1} + F_{Jk}^{-1} F_{Ig}^{-1} F_{Gk}^{-1} \right) N_J \Big]
\end{aligned}$$

$$\begin{aligned}
\mathcal{B}_{\boldsymbol{t},gG} &= \frac{\partial t_i}{\partial gG} = \sigma_{ij}\frac{\partial n_j}{\partial gG} = \sigma_{ij}\frac{\partial}{\partial gG}\left(\frac{F^{-1}_{Ii}N_I}{\sqrt{N_I F^{-1}_{Im}F^{-1}_{Km}N_K}}\right) \\
&= \sigma_{ij}\left[\frac{\partial F^{-1}_{Jj}N_J}{\partial F_{gG}}\left(\boldsymbol{N}\boldsymbol{C}^{-1}\boldsymbol{N}\right)^{-1/2} + F^{-1}_{Jj}N_J\frac{\partial}{\partial F_{gG}}\left(\boldsymbol{N}\boldsymbol{C}^{-1}\boldsymbol{N}\right)^{-1/2}\right] \\
&= \sigma_{ij}\Big[N_J F^{-1}_{Jg}F^{-1}_{Gj}\left(\boldsymbol{N}\boldsymbol{C}^{-1}\boldsymbol{N}\right)^{-1/2} - \\
&\qquad \frac{1}{2}F^{-1}_{Jj}N_J\left(\boldsymbol{N}\boldsymbol{C}^{-1}\boldsymbol{N}\right)^{-3/2}N_I\frac{\partial}{\partial F_{gG}}\left(F^{-1}_{Im}F^{-1}_{Km}\right)N_K\Big] \\
&= \sigma_{ij}\Big[N_J F^{-1}_{Jg}F^{-1}_{Gj}\left(\boldsymbol{N}\boldsymbol{C}^{-1}\boldsymbol{N}\right)^{-1/2} - \\
&\qquad \frac{1}{2}F^{-1}_{Jj}N_J\left(\boldsymbol{N}\boldsymbol{C}^{-1}\boldsymbol{N}\right)^{-3/2}N_I\left(\frac{\partial F^{-1}_{Im}}{\partial F_{gG}}F^{-1}_{Km} + F^{-1}_{Im}\frac{\partial F^{-1}_{Km}}{\partial F_{gG}}\right)N_K\Big] \\
&= \sigma_{ij}\Big[N_J F^{-1}_{Jg}F^{-1}_{Gj}\left(\boldsymbol{N}\boldsymbol{C}^{-1}\boldsymbol{N}\right)^{-1/2} - \\
&\qquad \frac{1}{2}F^{-1}_{Jj}N_J\left(\boldsymbol{N}\boldsymbol{C}^{-1}\boldsymbol{N}\right)^{-3/2}N_I\left(F^{-1}_{Ig}F^{-1}_{Gm}F^{-1}_{Km} + F^{-1}_{Im}F^{-1}_{Kg}F^{-1}_{Gm}\right)N_K\Big]
\end{aligned} \tag{A.4}$$

A.3 External load from fluid stress tensor, $\boldsymbol{\tau}$

The formulation is simplified if the traction on the boundary is expressed as the product of the Cauchy stress tensor and the current surface normal, $t_j = \tau_{ij}n_i$. The traction load is then calculated as

$$\int_{\partial B}\boldsymbol{\delta u}\cdot\boldsymbol{t}\;da = \int_{\partial B}\boldsymbol{\delta u}\cdot\left(\boldsymbol{\tau}\cdot\boldsymbol{n}\right)\;da = \int_{\partial B_0}\boldsymbol{\delta u}\cdot\left(\boldsymbol{\tau}\cdot\left(J\boldsymbol{F}^{-T}\cdot\boldsymbol{N}\right)\right)\;dA. \tag{A.5}$$

The advantage of this form is that the resulting linearization is simpler:

$$\begin{aligned}
D\int_{\partial B}\delta u_j t_j\;da[\boldsymbol{u}] =& D\int_{\partial B}\delta u\left(\tau_{ij}n_i\right)\;da[\boldsymbol{u}] \\
=& D\int_{\partial B_0}\delta u_j\left(\tau_{ij}\left(JF^{-1}_{Ii}N_I\right)\right)\;dA[\boldsymbol{u}] \\
=& \int_{\partial B_0}\delta u_j\left(\tau_{ij}N_I\;D\left(JF^{-1}_{Ii}\right)[\boldsymbol{u}]\right)\;dA \\
=& \int_{\partial B_0}\delta u_j\left(\tau_{ij}N_I\;\mathcal{B}_{IikK}\frac{\partial u_k}{\partial X_K}\right)\;dA,
\end{aligned} \tag{A.6}$$

where

$$\begin{aligned}\mathcal{B}_{IikK} =& \frac{\partial}{\partial F_{kK}}\left(JF_{Ii}^{-1}\right) = \left(\frac{\partial J}{\partial F_{kK}}F_{Ii}^{-1} + J\frac{\partial F_{Ii}^{-1}}{\partial F_{kK}}\right) \\ =& J\left(F_{Kk}^{-1}F_{Ii}^{-1} - F_{Ik}^{-1}F_{Ki}^{-1}\right).\end{aligned} \tag{A.7}$$

A.4 Spatial discretization of structural equations

Solution values $\boldsymbol{X}$ and $\boldsymbol{u}$ are stored at the n nodal locations per element. Values are interpolated using shape functions N of order n

$$X_d = \sum_{a=1}^{n} N_a \hat{X}_{ad}, \tag{A.8}$$

where d is the direction index, a is the element local node index, and $\hat{(\ )}$ denotes the nodal value of a given quantity. Isoparametric elements are used, so that

$$\int_e \phi(\boldsymbol{x})\ dV = \int_{-1}^{1} \phi'(\boldsymbol{\xi}) J\ d\boldsymbol{\xi}$$

where $J = det\,(\partial \boldsymbol{X}/\partial \boldsymbol{\xi})$. Numerical integration is done using Gauss quadrature, so that (in three dimensions, for example)

$$\int_{-1}^{1}\int_{-1}^{1}\int_{-1}^{1} \phi'(\boldsymbol{\xi})J(\boldsymbol{\xi})\ d\xi d\eta d\zeta \approx \sum_{i=1}^{ng}\sum_{j=1}^{ng}\sum_{k=1}^{ng} \phi'(\xi_{ijk})J(\xi_{ijk})W(\xi_i)W(\eta_j)W(\zeta_k).$$

Discretizing the first term of Eq. (3.15) for each element

$$\begin{aligned}\int_e \beta^2(\Theta)\hat{\boldsymbol{P}} : \boldsymbol{\delta F}\ dV \approx \delta\hat{u}_{ad} \sum_{ijk=1}^{ng} \beta^2(\boldsymbol{\xi}_{ijk}) P_{dK}(\boldsymbol{\xi}_{ijk}) \frac{\partial N_a(\boldsymbol{\xi}_{ijk})}{\partial \xi_l} \frac{\partial \xi_l}{\partial X_K} J(\boldsymbol{\xi}_{ijk}) \\ \times W(\xi_i)W(\eta_j)W(\zeta_k) = \delta\hat{u}_{ad} r_{ad}^{int},\end{aligned}$$

which, when assembled over the entire body, B_0, gives

$$\int_{B_0} \beta^2(\Theta)\hat{\boldsymbol{P}} : \boldsymbol{\delta F}\ dV \approx \boldsymbol{\delta\hat{u}}^T \boldsymbol{R}^{int}.$$

In the latter relation, $\boldsymbol{R}^{int}$ is the internal load vector. The remaining terms are discretized similarly:

The external load due to a body force over an element is given by

$$\int_e \rho_0 \boldsymbol{b} \cdot \boldsymbol{\delta u} \; dV \approx \delta \hat{u}_{ad} \sum_{ijk=1}^{ng} \rho_0(\boldsymbol{\xi}_{ijk}) b(\boldsymbol{\xi}_{ijk}) N_a(\boldsymbol{\xi}_{ijk}) J(\boldsymbol{\xi}_{ijk})$$

$$\times W(\xi_i) W(\eta_j) W(\zeta_k) = \delta \hat{u}_{ad} r_{ad}^{body}.$$

When added over B_0, this term yields

$$\int_{B_0} \rho_0 \boldsymbol{b} \cdot \boldsymbol{\delta u} \; dV \approx \boldsymbol{\delta \hat{u}}^T \boldsymbol{R}^{body},$$

where $\boldsymbol{R}^{body}$ is the external load vector due a body force.

The external load due to a traction force over an element takes the form

$$\int_{\partial e} \boldsymbol{t}_0 \cdot \boldsymbol{\delta u} \; dA \approx \delta \hat{u}_{ad} \sum_{ij=1}^{ng} t_{0a}(\boldsymbol{\xi}_{\boldsymbol{2D}ij}) N_a(\boldsymbol{\xi}_{\boldsymbol{2D}ij}) N_b(\boldsymbol{\xi}_{\boldsymbol{2D}ij}) J_{2D}(\boldsymbol{\xi}_{\boldsymbol{2D}ij})$$

$$\times W(\xi_i) W(\eta_j) = \delta \hat{u}_{ad} r_{ad}^{tract.}.$$

When assembled over the entire body, B_0, this term gives

$$\int_{\partial B_0} \boldsymbol{t}_0 \cdot \boldsymbol{\delta u} \; dA \approx \boldsymbol{\delta \hat{u}}^T \boldsymbol{R}^{tract.},$$

where $\boldsymbol{R}^{tract.}$ is the external load vector due a body force.

The acceleration term is discretized as follows:

$$\int_e \rho_0 \ddot{\boldsymbol{u}} \cdot \boldsymbol{\delta u} \; dV \approx \delta \hat{u}_{ad} \sum_{ijk=1}^{ng} \rho_0(\boldsymbol{\xi}_{ijk}) N_a(\boldsymbol{\xi}_{ijk}) N_b(\boldsymbol{\xi}_{ijk}) J(\boldsymbol{\xi}_{ijk})$$

$$\times W(\xi_i) W(\eta_j) W(\zeta_k) \ddot{u}_{bd} = \delta \hat{u}_{ad} m_{adbd} \hat{\ddot{u}}_{bd},$$

which, when added over B_0 gives

$$\int_{B_0} \rho_0 \ddot{\boldsymbol{u}} \cdot \boldsymbol{\delta u} \; dV \approx \boldsymbol{\delta \hat{u}}^T \boldsymbol{M} \hat{\ddot{\boldsymbol{u}}},$$

where $\boldsymbol{M}$ is the mass matrix.

Finally, the linearized internal work term yields

$$\int_e \beta^2(\Theta)\boldsymbol{\delta F} : \mathcal{A} : \nabla_{\boldsymbol{X}}\Delta\boldsymbol{u}\; dV$$
$$\approx \delta\hat{u}_{ad}\sum_{ijk=1}^{ng}\beta^2(\boldsymbol{\xi}_{ijk})\mathcal{A}_{KdLm}(\boldsymbol{\xi}_{ijk})\frac{\partial N_a(\boldsymbol{\xi}_{ijk})}{\partial\xi_l}\frac{\partial\xi_l}{\partial X_K}\frac{\partial N_b(\boldsymbol{\xi}_{ijk})}{\partial\xi_q}\frac{\partial\xi_q}{\partial X_L}$$
$$\times J(\boldsymbol{\xi}_{ijk})W(\xi_i)W(\eta_j)W(\zeta_k)\Delta\hat{u}_{bm} = \delta\hat{u}_{ad}k_{adbm}\Delta\hat{u}_{bm}.$$

The global form of that term is then

$$\int_{B_0}\beta^2(\Theta)\boldsymbol{\delta F} : \mathcal{A} : \nabla_{\boldsymbol{X}}\boldsymbol{u}dV \approx \boldsymbol{\delta u}^T\boldsymbol{K}\Delta\hat{\boldsymbol{u}},$$

where $\boldsymbol{K}$ is the tangent stiffness matrix. The discretized form of the principle of virtual work is thus

$$\boldsymbol{\delta u}^T\left(\boldsymbol{R}^{int} + \boldsymbol{M}\ddot{\boldsymbol{u}} - \boldsymbol{R}^{tract.} - \boldsymbol{R}^{body} + \boldsymbol{K}\Delta\boldsymbol{u}\right) = \boldsymbol{0}, \qquad \text{(A.9)}$$

where the $\hat{(\;)}$ on nodal values are assumed.

A.5 Area change

The relation between the areas in the reference (initial) and deformed (current) configurations is derived as follows. We can first start with the relation between two volume elements, dv and dV, in the current and initial configurations, respectively

$$dv = JdV, \qquad \text{(A.10)}$$

where the Jacobian, $J = det(\boldsymbol{F})$. Each volumes can be decomposed into the product of an area and a length element

$$dv = d\boldsymbol{l}\cdot d\boldsymbol{a},$$

and

$$dV = d\boldsymbol{L}\cdot d\boldsymbol{A},$$

where

$$d\boldsymbol{l} = \boldsymbol{F} d\boldsymbol{L}.$$

Plugging into Eq. (A.10) and multiplying both sides by $\boldsymbol{F}^{-1}$ gives the resulting relation between area vectors

$$d\boldsymbol{a} = J\boldsymbol{F}^{-T} d\boldsymbol{A}. \tag{A.11}$$

This is known as Nanson's relation. To relate the two scalar areas, we use the fact that $da = \sqrt{d\boldsymbol{a} \cdot d\boldsymbol{a}}$. When applied to Eq. (A.11), this results in

$$da = \sqrt{d\boldsymbol{a} \cdot d\boldsymbol{a}} = \sqrt{J\boldsymbol{F}^{-T} d\boldsymbol{A} \cdot J\boldsymbol{F}^{-T} d\boldsymbol{A}} = J\sqrt{[\boldsymbol{N}\boldsymbol{F}^{-1}]^T \boldsymbol{F}^{-T} \boldsymbol{N}} dA$$

$$= J\sqrt{\boldsymbol{N} \cdot \boldsymbol{F}^{-1} \boldsymbol{F}^{-T} \boldsymbol{N}} dA$$

This gives the final relation as

$$da = J\sqrt{\boldsymbol{N} \cdot \boldsymbol{C}^{-1} \boldsymbol{N}} dA.$$

Appendix B

Additional Validations

B.1 Additional Validation studies

In this section we provide some of the necessary validations to corroborate our results so far.

B.1.1 Quasi 1D vs Constant Inflow boundary conditions

We mentioned in Sec. 4.1, the theory behind the quasi 1D inflow boundary conditions that we implemented for all our simulations. Since, it is different from the traditional inflow condition used by most other studies, that of a constant pressure, we conducted a comparative study with both the boundary conditions, to measure and quantify the impact of considering one over another. As such from our adult simulation study with quasi 1d inflow condition, we took the mean of the inflow pressure over the first cycle (comes out to be 1.9 kPa), and applied this value at the inflow to run the constant pressure boundary condition case. We still calculate the other inflow parameters at each time iteration like density and velocities with the quasi 1d theory.

Now, with the inflow pressure fixed to a constant value, we obtained both the near vocal fold and far-field data, and compared them against the already available data from adult simulation. Figure B.1 compares the near vocal fold results for upstream gauge pressure, downstream flow rates and minimum vocal fold gaps from centerline. The top left plot of upstream gauge pressure shows that the pressure over the cycles, show a marked reduction for the constant pressure case. The maximum difference with respect to the maximum pressure value observed here is 8%, which is significant. We also notice similar differences for the minimum vocal fold gaps from the centerline which being nearly 7.5% for both the vocal folds. The downstream flow rate also

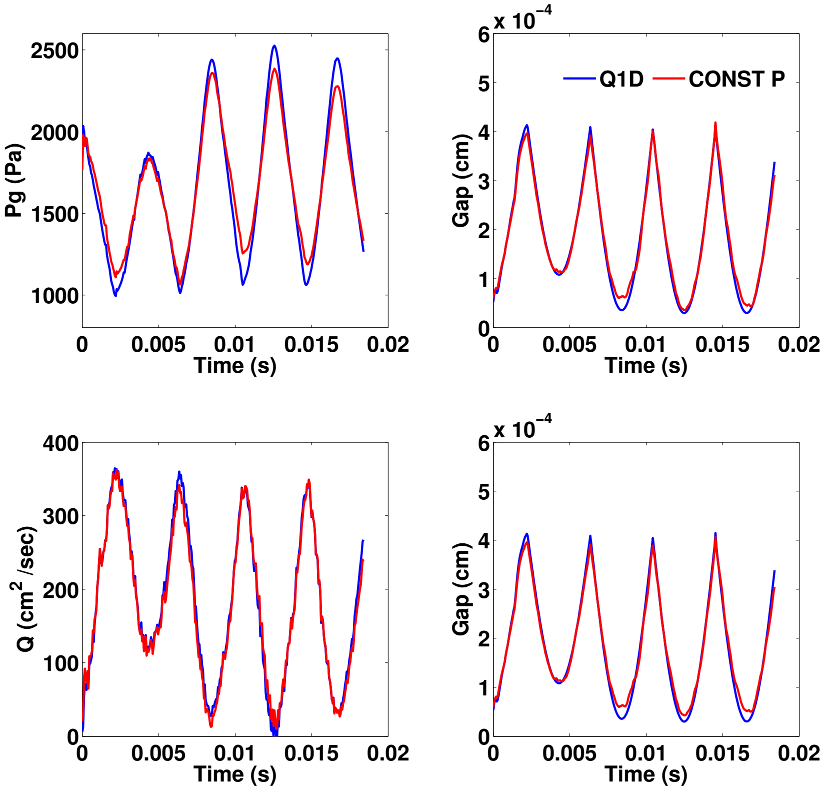

Figure B.1: Quasi 1D versus constant pressure inflow boundary condition study: Upstream gauge pressure (top left), flow rate at vocal fold exit (bottom left), left vocal fold minimum gap from centerline (top right) and right vocal fold minimum gap from centerline (bottom right).

showed a relative difference of 4.5%. As observed for the upstream pressure plot, the vocal fold oscillation amplitudes also show significant reductions for the constant pressure case.

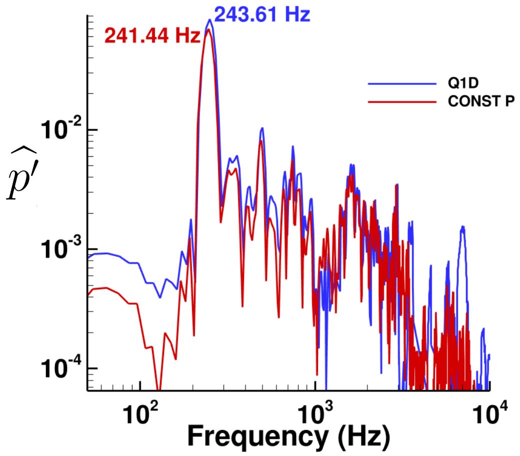

Figure B.2: Quasi 1D versus constant pressure inflow boundary condition study: FFT comparison for acoustic pressure data measured at a point in the far-field.

However, the most striking feature of this comparison is that both sets of inflow boundary conditions lead to insignificant variation in the frequency associated with the each of the above extracted quantities. This is further verified by looking at the frequency spectrum of the far-field radiated pressure at a point located directly in front of the speaker's mouth and at a distance of 2 feet. The frequency spectrums shown in Figure B.2 for the two cases, bear close resemblance both qualitatively and quantitatively. The peak corresponding to the fundamental frequency are also very close with a relative error of 0.9%. This confirms our observation in the near vocal fold data. This suggests that the quantities considered here have a strong dependence on the vocal fold oscillation frequency, which in turn is possibly proportional to the mean pressure variation at the inflow, since it was the mean of the pressure at inflow which we obtained from the quasi 1D data, that we imposed for the constant pressure driven simulation. This hypothesis needs validation, which can be accomplished by running the quasi 1D case with varying inflow velocities resulting in different mean inflow pressures. This can form a part of the future work for this thesis.

B.1.2 Lubrication Theory in Phonation

In order to explain the no-collision occurrence of the VFs, lubrication theory perspective is employed. When the VFs come very close to each other (or when (minimum VF gap)/(characteristic length scale ‘L’) $\ll 1$), high pressure develops in the glottis that eventually pulls them apart. With $L = 1\,\mathrm{cm}$, based on length and width of the vocal tract as the reference length, this factor comes out to be quite small (O[10^{-2}]). A quasi-steady form of the Reynolds equation (based on lubrication theory for a thin film) is adopted. This assumption is attributed to the fact that the VF motion and the mean glottal flow are relatively slow phenomena as compared to the speed of acoustic waves.

$$\frac{\partial}{\partial x}\left(\frac{h^3 \partial P}{\partial x}\right) = 6\mu U \frac{\partial h}{\partial x} \tag{B.1}$$

where h, U, P and μ are the VF gap, axial velocity, pressure and air viscosity respectively.

For each oscillation cycle $\frac{\partial p}{\partial x}$ was calculated using Eq. (B.1) and compared it to the value obtained from simulation results. Figure B.3 shows this variation of $\frac{\partial p}{\partial x}$ and minimum gap variation of the VFs plotted below it for Poisson’s ratio 0.27 and 0.47. Three cycles of VF oscillation with time have been presented here. It is noted that the minimum gap which corresponds to the instant when the VFs are near closure, the lubrication theory prediction is significantly close to simulation result. However at other stages of VF oscillation this prediction is not as accurate, which implies the role of lubrication during the closing phase of VFs is predominant. Thus, the lubrication effect does come into play during VF closure which would lead to a rise in pressure in the glottis which in turn pulls the VF apart.

B.1.3 Rectangular Vocal Tract

We investigate a simplified rectangular version of the vocal tract to set a baseline for further anatomically representative geometry. This case was considered to study the differences in the results from the present formulation to those in the literature. Figure B.4, shows the computational domain for the rectangular vocal tract configuration. The lungs on the left of the domain, provide the necessary pressure forcing to start the VF oscillations,

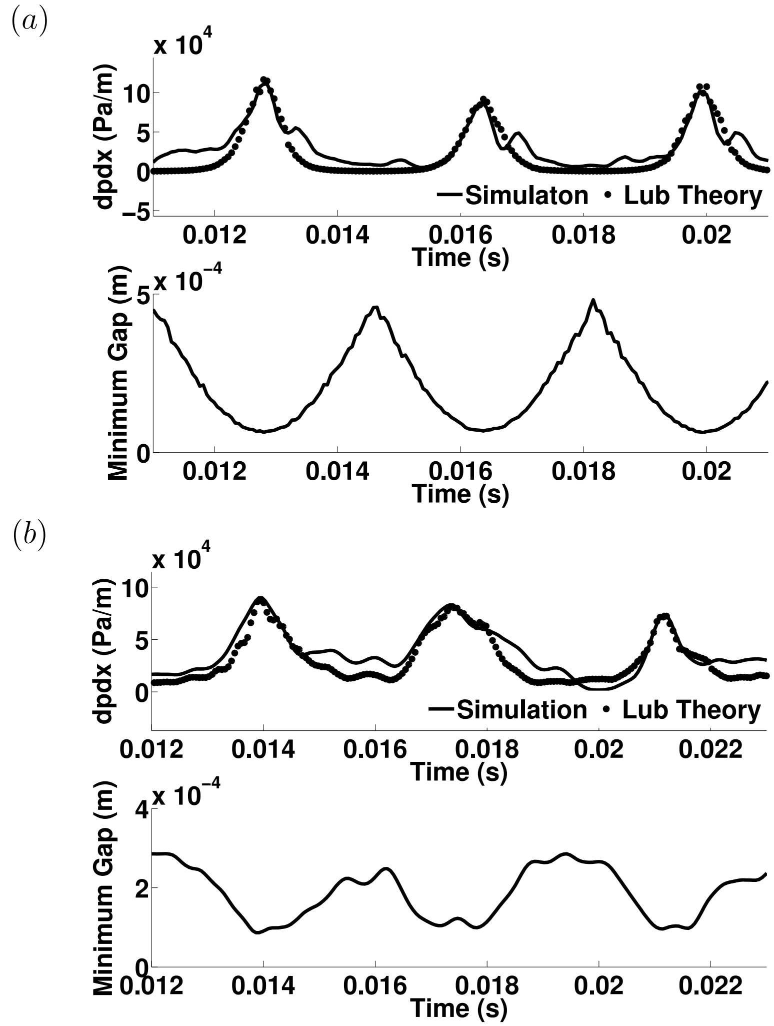

Figure B.3: Comparison of $\frac{\partial p}{\partial x}$ from lubrication theory and simulation for three vocal fold oscillation cycles (top) and minimum gap variation of the vocal folds (bottom) with (a) ν =0.27 and (b) ν =0.47.

while at the rear end the conditions are set to ambient depicting exit from the mouth. We employ the quasi-1D approach described in Sec. 4.1 to obtain the inflow pressure. The VFs and the glottal flow interact in a two way coupling. Details of the coupling mechanism have been described in Chapter 3. Initial condition is obtained and set from the quasi 1D formulation described in the previous section corresponding to area function at the start of the simulation.

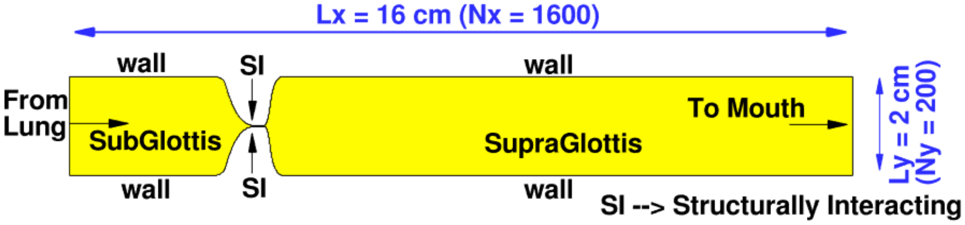

Figure B.4: Rectangular vocal tract domain showing the different boundary conditions and grid detail. VF interface is marked with 'SI' which stands for a structurally interacting surface.

For modeling the VFs, we use a three layer model composed of the cover, ligament and the body as shown in Figure 4.2. The VF layers terminate into a stiff cartilage after transitioning smoothly through a transition layer. The material properties of the VFs are given in Table 4.2. The values of the material parameters are chosen from [71] and are relatively stiffer than usual.

Figure B.5 shows the vorticity contours and the corresponding VF motions for different time instants. Here $Time = t^{*}c/L$, where t^{*} is the dimensional time, c is the sound speed and $L = 1\,\text{cm}$ (based on length and width of the vocal tract Figure B.4), is the reference length. The flow in the small gap is is basically viscous dominated and the resulting glottal flow exhibits unsteadiness as shown by the vorticity contours. Another observation from the figure, is the underlying asymmetry in the flow past the glottis. The eddies that largely remain parallel to the vocal tract initially, curl up from one VF to the other without any bias. This phenomenon has been observed in previous two-dimensional simulation studies [30–32, 40, 41, 43, 45, 71]. This asymmetry has been attributed to jet confinement, its pulsatility and the intrinsic instabilities of the glottal jet itself [157]. It is the interaction of these eddies with the supraglottal walls of the vocal tract and among themselves, which play a significant role on the measured radiated acoustic field, however, the major contribution still being the VF motion acting as a mass source. These can be well understood with the far field acoustic plots for the full body simulation cases to be discussed later, where we extended the domain to contain region outside the human body.

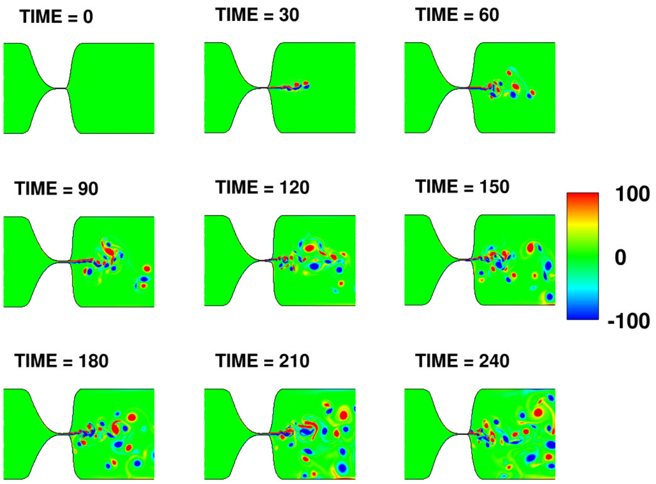

Figure B.5: VF dynamics and vorticity contours for the rectangular vocal tract simulation. Time is $t^{*}c/L$.

We now plot the variation of the centerline gauge pressure and axial velocity, at one time instant, along the entire vocal tract in Figure B.6. The pressure drops rapidly in the glottis, as a result of the blockage provided by the VFs. This is evident in the rapid rise and then fall of the centerline axial velocity, which peaks at the point of minimum glottal area. There is also significant variations in pressure just past the VFs ($x > 0cm$) , due to the unsteady flow in that region.

We also obtained the fast fourier transform of pressure fluctuations at $x = 4.5$ cm past the VF exit. Figure B.7 shows that there is a dominant frequency also called the fundamental frequency or F0. Also we see that our value of F0 = 254 Hz, is on the higher side of the phonatory limit (65 Hz < F0 < 260 Hz) [71]. This is due to the relatively higher values of VF stiffness that we use.

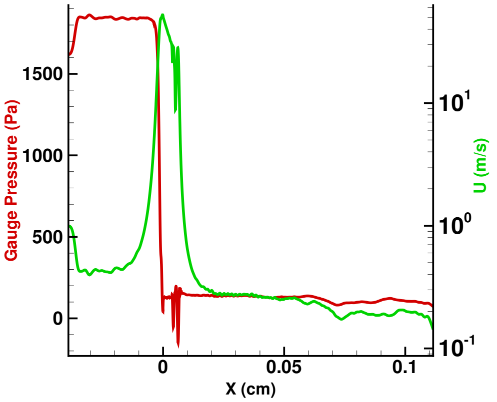

Figure B.6: Axial pressure and $x-$ velocity variation for the rectangular vocal tract case along the centerline.

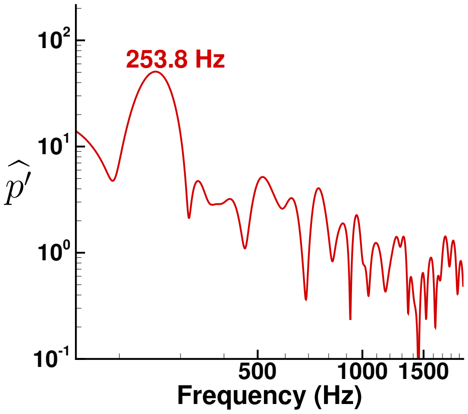

Figure B.7: FFT of the pressure fluctuation at $x = 4.5$ cm past VF exit.

B.1.4 Navier-Stokes vs Quasi 1D Euler governing equation

Phonation simulations studies have utilized the quasi 1D Euler system of equations to a great extent as governing equations to solve for the flow field in a rectangular vocal tract domain [25–28,162]. Here we look at a comparative study done using both quasi 1D Euler and our Navier-Stokes solver. For the sake of completeness we provide the quasi 1D Euler equations:

$$
\begin{aligned}
\frac{\partial \rho A}{\partial t} + \frac{\partial \rho u A}{\partial x} &= 0 \\
\frac{\partial \rho u A}{\partial t} + \frac{\partial (\rho u^2 + p) A}{\partial x} &= p\frac{\partial A}{\partial x} \\
\frac{\partial \rho E A}{\partial t} + \frac{\partial (\rho E + p) u A}{\partial x} &= -p\frac{\partial A}{\partial t}
\end{aligned} \tag{B.2}
$$

with,

$$
\rho E = \frac{p}{\gamma - 1} + 0.5\rho u^2 \tag{B.3}
$$

The simulation is then carried out in the following order:

- The rectangular vocal tract case is run with Navier-Stokes as the governing equations.
- From this the area function variation $A(x, t)$, with space and time is extracted along the vocal tract boundary.
- The area function obtained above is then provided as an input to the quasi 1D Euler equation solver and the flow is solved for equal number of time iterations as the Navier-Stokes data.

With the results obtained from both simulations we first do a simple error check to understand the difference between the two data sets. For this, we simply plug the solutions from both the quasi 1D Euler and Navier-Stokes simulations, into the quasi 1D Euler system of equation Eq. (B.3). Figure B.8 shows this comparison. One major take aways from this plot is that the quasi 1D Euler solution does lie along the $y = 0$ line, indicating the correctness of the quasi 1D Euler simulation results. Another point to note is the deviation which the Navier-Stokes solution exhibits from the $y = 0$, line. Now to read this plot correctly, we need to understand that any deviation for the Navier-Stokes solution in this plot, can also be interpreted as the error that the quasi 1D Euler equations, Eq. (B.3), would encounter due to its inherent simplifications based on inviscid, one dimensional assumptions. We notice deviations all along the domain, with major impact concentrated around x =0, which for our case is where the domain encounters the maximum area variation due to the presence of the vocal folds with highly dominated viscous flow, and part of the domain represented by the wake with non-uniform flow due to vortex shedding and vortex interactions. Thus quasi 1D Euler system of equations, Eq. (B.3), will exhibit large errors due to the absence of a multi-dimension, viscous model to capture the aforementioned effects. Moreover, the small differences observed elsewhere in the domain, are again due to the incapability of the quasi 1D Euler system to capture the boundary layer effects due to its inviscid nature.

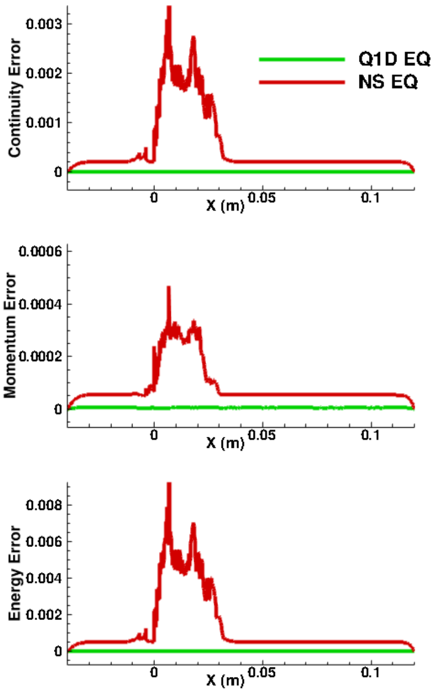

Figure B.8: Continuity (top), Momentum (center) and Energy (bottom) equation errors obtained by plugging quasi 1D Euler and Navier-Stokes simulation data into the Quasi 1D Euler equations.

In order to validate the above theory, we plotted some quantities from the two simulations and compared them. Figure B.9, shows the gauge pressure variations at a point upstream i.e. just before the vocal folds, point $x = 4.5$cm and the difference between the values for the above two locations. We notice that while in the upstream quasi 1D Euler system under-predicts the pressure as compared to Navier-Stokes system, it mostly over-predicts the same downstream. Moreover, the differences are quite significant. Both the upstream and the downstream maximum errors with respect to the corresponding maximum value for the quantity is greater than 40%, which is significantly large. Similar errors are seen to occur in the pressure difference plotted at the bottom of the figure.

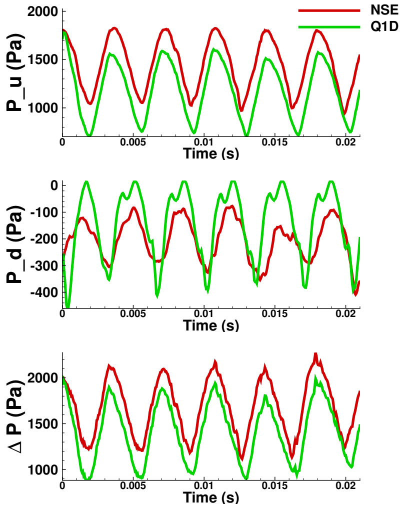

Figure B.9: Comparison of pressures at a point just before the vocal folds (top), at $x = 4.5cm$ (center) and the difference of these two pressures (bottom) from the Navier-Stokes and quasi 1D Euler simulations.

In order to look at sound characteristics we calculated the frequency spectrum for the two cases, by considering pressure fluctuations at $x = 4.5$ cm and obtaining its fast-fourier transform. Figure B.10 shows this variation, wherein we note an approximate error of 9 Hz in predicting the fundamental frequency by the quasi 1D Euler system. Also the sound pressure levels were found out to be 136 dB and 132 dB from the quasi 1D Euler and Navier-Stokes simulations respectively, at the above mentioned point. Again, this is a significant difference.

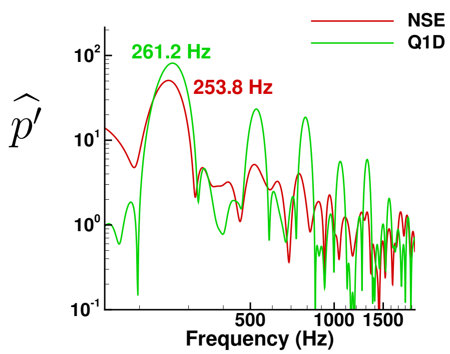

Figure B.10: Comparison of FFT of pressure fluctuations from the Navier-Stokes and Quasi-1D simulations measure at $x = 4.5cm$

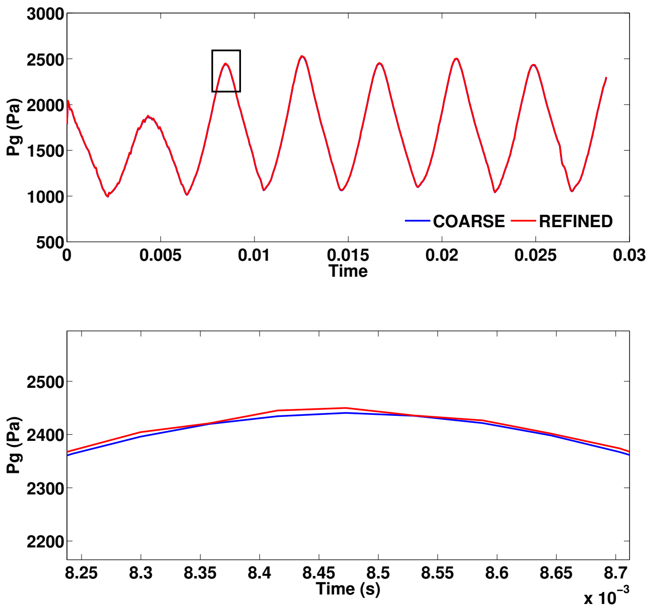

Figure B.11: Grid refinement study: Upstream gauge pressure (top) and its zoomed plot (bottom) near the location indicated by the rectangular black box.

B.1.5 Grid Refinement study

Due to lack of analytical or similar solutions available to validate our simulation results, apart from already observing resulting parameters like vocal fold oscillation frequencies, flow field variation in the vocal tract, and far-field radiated sound quantities, being within expected ranges as compared to other studies in the literature, we needed to have a grid refinement study conducted, to verify grid independence. As such we repeated the adult simulation for a grid with approximately 1.5 times the resolution in each direction for all the blocks in the domain. We present here the results from this study.

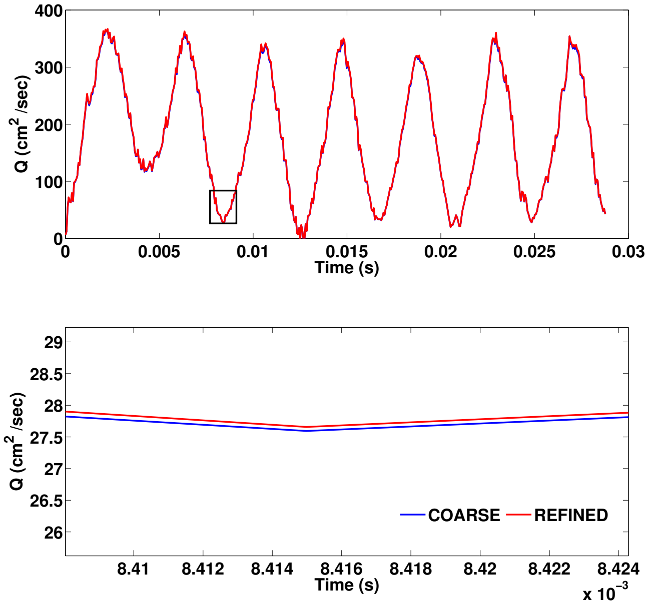

Figure B.12: Grid refinement study: Flow rate at vocal fold exit (top) and its zoomed plot (bottom) near the location indicated by the rectangular black box.

We considered three different quantities for this. First, Figure B.11 shows a comparison of the upstream gauge pressure (measured at a location just before the start of vocal folds). We see that the the two grids, provide almost perfect match, when some differences can be noticed upon zooming. The zoomed region indicated by the square block on the top plot, is shown below it. The maximum difference/error with respect to the maximum value of this quantity was found to be 0.5%. Next we do the same with flow rate measured downstream, Figure B.12 and minimum left vocal fold gap from centerline, Figure B.13. We again observe significantly small differences upon zooming near a certain location. The errors obtained were 0.4% and 0.7% for the flow rate and minimum left vocal fold gap respectively. Since, we observe, insignificant differences between the two grid results, proves our current grid is well resolved to extract grid independent results.

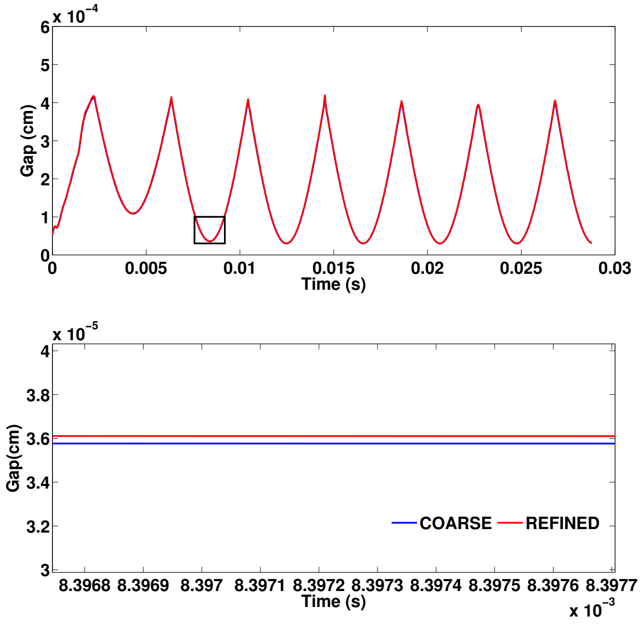

Figure B.13: Grid refinement study: Left vocal fold minimum gap from centerline (top) and its zoomed plot (bottom) near the location indicated by the rectangular black box.

Appendix C

Additional Results and Discussion

C.1 Geometric Elimination of Reflecting Wave Component

From the figure Figure C.1 we know that the overall velocity at any point can be decomposed into x and y components, i.e. u' and v'. Now if we consider only the waves coming out of the speaker's mouth, then let us say that at a certain point in the domain as shown in the figure, the velocity is given by $V1'$ for this wave. Similarly, for the reflecting wave, the associated velocity is $V2'$. Now both these wave velocities are unknowns. We need to determine them using the knowns namely $u', v', \theta_1, \theta_2$, where θ_1 and θ_2 are the angles that $V1'$ and $V2'$ extend to y axis, and can be obtained by the information of the coordinates of center of the two waves and the coordinates of the point of interest. The center of the emitted waves is taken at the midpoint of the exit of the mouth of speaker, while for the reflecting waves it is calculated based on any 3 given points on the reflecting wave at a given time instant. So with these four knowns, we write the following equations:

$$u' = -V_1' \sin(\theta_1) + V_2' \sin(\theta_2) \tag{C.1}$$

and,

$$v' = V_1' \cos(\theta_1) + V_2' \cos(\theta_2) \tag{C.2}$$

Using these equations we can eliminate V_2' and just have V_1' component of the total velocity. Thus we eliminate any contribution from the reflecting waves. We then resolve V_1' into its x and y components to get the vector $\boldsymbol{V_1'}$

With the value of $\boldsymbol{V_1'}$ obtained for all points in the domain, we can plug it into the linearized energy equation

$$\frac{dp'}{dt} = -\gamma P_{inf} \nabla . \boldsymbol{V_1'} \tag{C.3}$$

and solve for p'. This p' will only have contributions from the original wave.

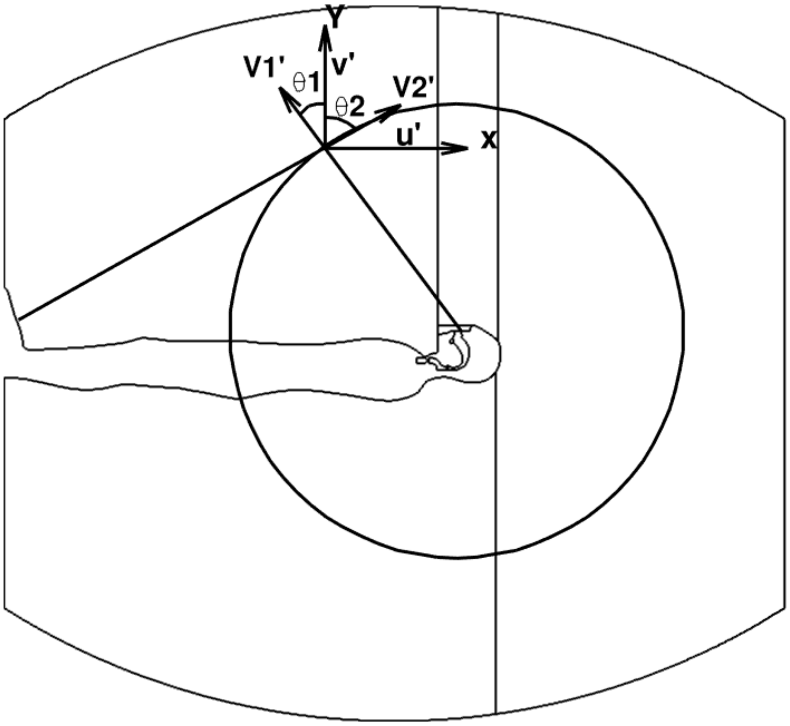

Figure C.1: Image describing the various geometric parameters required to eliminate components of V_2'.